Development of a reduced-order model of a non-uniform distortion screen and re-staggered inlet guide vane

Tesi di Laurea Magistrale in
Mechanical Engineering - Ingegneria Meccanica

Author: **Alessandro Nardone**

Student ID: 252500
Advisor: Prof. Paolo Gaetani
Co-advisor: Prof. Fabrizio Fontaneto
Academic Year: 2025-2026

Abstract

The demand for lower aircraft emissions is driving the development of advanced propulsion technologies such as Short-Nacelle High-Bypass (SNHB) turbofans, Boundary Layer Ingestion (BLI) engines and open rotor architectures. Unlike conventional engines, where inlet distortion arises only in off-design or transient regimes, these configurations operate continuously under highly distorted inflow, posing critical challenges for engine stability. The low-pressure compressor (booster) is particularly sensitive to inlet distortion, which can compromise engine operability and motivates effective mitigation strategies. A promising approach is the optimized scheduling of the inlet guide vanes (IGV), non-uniformly re-staggered across the annulus to restore the rotor incidence.

This problem was investigated experimentally, prior to this work, at the von Karman Institute for Fluid Dynamics (VKI), through a campaign on the R4 high-speed compressor test rig. A low pressure compressor 1.5-stage was tested on the test rig, where a realistic total pressure distortion was reproduced by a distortion screen upstream of the IGV row. This campaign, which constitutes the starting point of the present study, showed a significant performance degradation under distorted inflow, induced by high rotor incidence, which increases profile and secondary losses.

The final objective of this work is to propose an effective design strategy for a non-uniform stagger of the IGV that promotes the recovery of the compressor performance under distorted inlet conditions, based on a comprehensive understanding of the flow redistribution through the distortion screen. A low-order model is developed to predict the redistribution across one or multiple non-uniform screens in series, accounting for their coupled effects as a function of the axial distance; the approach is then extended to a non-uniformly re-staggered IGV row and validated against dedicated two-dimensional and 2.5D CFD simulations of the combined configuration. The results demonstrate the capability of the model to capture the interaction between inlet distortion and IGV scheduling, providing a tool to design distortion screens that achieve a desired pattern, predict rotor operating conditions, and provide optimized IGV re-staggering strategies.

Abstract in lingua italiana

La richiesta di ridurre le emissioni degli aeromobili sta guidando lo sviluppo di tecnologie propulsive avanzate, quali i turbofan Short-Nacelle High-Bypass (SNHB), i motori Boundary Layer Ingestion (BLI) e le architetture open rotor. A differenza dei motori convenzionali, in cui la distorsione all'ingresso compare solo in operazioni off-design o nei transitori, queste configurazioni operano continuativamente in flusso fortemente distorto, con sfide critiche per la stabilità del motore. Il compressore di bassa pressione (booster) è particolarmente sensibile alla distorsione all'ingresso, che può comprometterne l'operabilità e motiva efficaci strategie di mitigazione. Un approccio promettente è la regolazione ottimizzata delle inlet guide vanes (IGV), ricalettate in modo non uniforme lungo la circonferenza per ripristinare l'incidenza sul rotore. Tale problema è stato studiato sperimentalmente presso il von Karman Institute for Fluid Dynamics (VKI), testando un compressore di bassa pressione a 1.5 stadi sul banco prova ad alta velocità R4, con una distorsione di pressione totale realistica riprodotta da uno schermo a monte della schiera di IGV. Questa campagna, punto di partenza del presente studio, ha evidenziato una significativa degradazione delle prestazioni in flusso distorto, indotta dall'elevata incidenza sul rotore, che incrementa le perdite di profilo e secondarie.

L'obiettivo della tesi è proporre un'efficace strategia di calettamento non uniforme delle IGV per il recupero delle prestazioni in ingresso distorto, basata su una comprensione approfondita della redistribuzione del flusso attraverso lo schermo. Per raggiungere tali obiettivi è stato sviluppato un modello di ordine ridotto per predirre la redistribuzione attraverso uno o più schermi non uniformi in serie, tenendo conto dei loro effetti accoppiati in funzione della distanza assiale; l'approccio è poi esteso a una schiera di IGV ricalettata in modo non uniforme e validato con simulazioni CFD bidimensionali e 2.5D. I risultati dimostrano la capacità del modello di cogliere l'interazione tra distorsione all'ingresso e regolazione delle IGV, fornendo uno strumento per progettare schermi di distorsione che realizzino un pattern desiderato, predire le condizioni operative del rotore e proporre strategie ottimizzate di ricalettatura delle IGV.

Contents

1 | Introduction

1.1. Context and motivation

The aviation sector is currently facing increasing pressure to reduce its environmental impact, as it represents one of the fastest growing sources of greenhouse gas emissions. Ambitious long term targets have been established by the European Union to ensure the sustainability of air transport. In particular, according to the Flightpath 2050 vision for aviation [10], future aircraft technologies are expected to achieve up to a 75% reduction in CO_2 emissions per passenger kilometre and a 90% reduction in NO_x emissions by 2050, compared to year 2000 levels. Achieving these goals requires a profound transformation of current aircraft design and propulsion systems.

To meet these targets, a wide range of technological solutions is currently under development. These include advanced propulsion architectures and aircraft configurations, aimed at improving overall efficiency. Among the most promising concepts are open rotor engines, boundary layer ingestion (BLI) configurations and Short Nacelle High Bypass turbofans (SNHB).

A key challenge of these new design architectures is that they inherently cause the engine to operate with high levels of inlet flow non uniformity, also called 'distortion'. Contrary to conventional engines, where inlet flow distortion occurred only under specific operating conditions, such as high angle of attack flight and short duration manoeuvres, future aircraft engines are expected to operate continuously under such conditions, due to the distortion being intrinsic to the design. This shift has stimulated a growing interest in both experimental and computational research focused on understanding and mitigating the detrimental effects of inlet flow distortion.

Existing studies have mostly examined distortion effects on isolated fan or compressor stages exposed to canonical, symmetric distortion patterns. Prior to this work, the von Karman Institute for Fluid Dynamics (VKI) has conducted a dedicated experimental campaign on the VKI R4 high speed compressor test rig, used to test a 1.5 stage configuration composed of an Inlet Guide Vane (IGV) row, a rotor and a stator. The campaign has analysed the effects of a realistic and complex total pressure distortion pattern, representative of next generation propulsion architectures, on the performance and operability of a modern highly loaded low pressure axial compressor (booster). The distortion was reproduced by means of a total pressure distortion screen placed upstream of the IGV row.

The results of this campaign demonstrated that such distortion conditions severely compromise compressor performance, motivating the research and development of effective mitigation strategies. One promising approach consists in the non-uniform re-staggering of the Inlet Guide Vanes, where the vane angle is locally adjusted along the circumferential coordinate according to the distortion intensity experienced within each individual blade passage, with the goal of restoring the rotor incidence to its design value across the full annulus.

1.2. Overall objective of the thesis

The circumferential re-staggering of the IGV row introduces a second source of circumferential non-uniformity: the non-uniform stagger produces varying levels of blockage that redistribute the flow upstream, and this redistribution interacts with the distortion already imposed by the screen. Because the existing literature does not address configurations in which a distortion screen operates in close proximity to a non-uniformly staggered blade row, a modelling gap emerges: no predictive model currently captures the coupled interaction between the upstream redistribution driven by a non-uniform distortion screen and the additional redistribution introduced by a circumferentially varying IGV stagger angle. In the absence of such a model, the design of effective re-staggering patterns remains dependent on full-annulus Computational Fluid Dynamics (CFD) simulations, which are too computationally expensive to be practical within an iterative engineering design loop.

Building directly on the experimental campaign, the objective of the thesis is to develop a low-order numerical model capable of predicting the flow redistribution occurring across a system composed of a non-uniform distortion screen followed by a non-uniformly re-staggered row of Inlet Guide Vanes. The goal of the model is capturing the aerodynamic coupling between these two components, and in particular its dependence on the axial distance separating them. Achieving this first requires a physical understanding of the underlying redistribution mechanisms: how the screen geometry drives tangential mass-flow migration, and how the potential field of the IGV row propagates upstream and interacts with the distortion screen. On this physical basis, the low-order model is constructed and its results are validated against CFD simulations.

1.3. Detailed objectives of the thesis

The detailed objectives are the following:

1. Characterise the physics of circumferential flow redistribution through a non-uniform total pressure distortion screen, identifying the governing parameters and the resulting distributions of static pressure and Mach number as a function of the screen porosity $\beta(\theta)$ and wire diameter $d_w(\theta)$.
2. Characterise the aerodynamic coupling between the distortion screen and a non-uniformly re-staggered IGV row as a function of the axial distance separating the two components.
3. Develop a low-order model for the prediction of the circumferential flow field upstream and downstream of a non-uniform distortion screen and a re-staggered IGV row, as a direct consequence of the physical understanding established in the preceding objectives.
4. Propose a preliminary IGV re-staggering strategy based on the model predictions.

To achieve Objective 3, it was decided to first develop a low-order model for two distortion screens in series, treating the IGV row as an aerodynamic resistance analogous to a distortion screen from the flow redistribution standpoint. The IGV was then implemented in place of the second screen.

The model serves two practical purposes. First, it provides a design tool for non-uniform distortion screens, enabling a more accurate screen design procedure that accounts for the upstream flow redistribution and its effect on the effective total pressure loss distribution. Second, it supports the analysis and design of IGV re-staggering patterns by predicting the rotor inlet incidence distribution, as a direct function of the chosen stagger angle distribution $\gamma(\theta)$.

Thesis Outline

The thesis is structured in six chapters, whose content is summarised below.

Chapter 1 Introduces the broader context of sustainable aviation and the engineering challenges posed by novel propulsion architectures. It defines the context and motivation for the present work, and defines the specific objectives that the thesis aims to address.

Chapter 2 provides the theoretical background required for the motivation of the thesis. It describes the distortion mechanisms associated with Boundary Layer Ingestion (BLI) and Short Nacelle High Bypass (SNHB) turbofan architectures, explains how circumferential total pressure distortion affects compressor performance and stability margins.

Chapter 3 describes the experimental and computational tools used. The VKI R4 closed-loop test rig and the DREAM 1.5-stage compressor test section are presented, along with the design and installation of the total pressure distortion screen. The two-dimensional and 2.5D CFD methodologies adopted in ANSYS Fluent to validate the analytical models are also described, focusing on domain definition, screen modelling, mesh strategy, and grid convergence.

Chapter 4 develops a low-order stream-tube model for circumferential flow redistribution through a single non-uniform distortion screen. The physical hypotheses, spatial discretisation into circumferential stream-tubes, and the four-station axial structure are introduced. The total pressure loss correlation is presented, decoupling the contributions of screen porosity, wire-diameter Reynolds number, and inlet Mach number compressibility; and calibrated against seven experimental operating conditions. The iterative solution algorithm is described in detail and the model results are presented.

Chapter 5 extends the single screen framework to the configuration of two distortion screens placed in series. Two formulations are proposed: the *Coupled* model, and the *Decoupled* model, which are different in the way the static pressure assumption is implemented. A systematic validation against CFD simulations covering seven inter-screen axial distances reveals the validity range of each model. A *Hybrid* model is then introduced, which interpolates between the two models, as a function of the axial distance between the two screens

Chapter 6 – Screen–IGV Model replaces the second screen in the dual-screen framework with an Inlet Guide Vane (IGV) row, treating the blade row as a circumferentially non-uniform aerodynamic resistance analogous to a wire-mesh screen. The complete model is validated against a 2.5D CFD simulation of the VKI facility operating with the distortion screen at its nominal position and a uniformly staggered IGV.

2 | State of the art

2.1. Inlet distortion in modern propulsion architectures

The development of next-generation aircraft propulsion systems is strongly driven by the need to reduce fuel consumption, emissions, and noise. In this context, several innovative engine architectures are currently being investigated, including Boundary Layer Ingestion (BLI) propulsors, short-nacelle high-bypass turbofans (SNHB), and open-rotor configurations. Despite their different layouts, these concepts share a common aerodynamic challenge: the propulsion system operates under highly non-uniform inlet flow conditions.

Unlike conventional turbofan engines, where inlet distortion is mainly associated with off-design conditions such as crosswind or high angle of attack operations, these future architectures are characterized by distortion as an intrinsic operating condition. The incoming flow may contain strong total pressure deficits, swirl distortions, and radial non-uniformities generated by the interaction between the engine and the airframe.

This aspect is particularly relevant for the present work, since the objective of the experimental campaign at the Von Karman Institute (VKI) is to reproduce representative distortion patterns through dedicated distortion screens and to study the associated flow redistribution mechanisms. Understanding the physics of inlet distortion is therefore a necessary preliminary step before developing distortion mitigation strategies based on non-uniform IGV re-staggering.

Boundary layer ingestion (BLI)

In conventional podded configurations, the engine ingests nearly uniform free-stream air, while the low-momentum wake generated by the aircraft fuselage is dissipated downstream, contributing to aerodynamic losses. Boundary Layer Ingestion (BLI) aims to recover part of this lost kinetic energy by ingesting the low-momentum boundary layer

Figure 2.1: Model of the D8 transport aircraft [23].

flow into the propulsion system. This is achieved by placing the engine at the end of the fuselage. Figure 2.1 shows a model of one possible configuration of a BLI engine.

The aerodynamic benefit of BLI can be interpreted through actuator disk theory. In a simplified model, the propulsion system re-energizes the aircraft wake, reducing the velocity deficit downstream of the aircraft. Since the ingested flow already possesses a lower momentum compared to the free stream, the required kinetic energy addition to generate thrust is reduced compared to a conventional configuration. This leads to an increase in propulsive efficiency.

A direct consequence of Boundary Layer Ingestion (BLI) architectures is the ingestion of a highly non-uniform inlet flow, characterized by both radial and circumferential distortions. The ingested boundary layer introduces a low momentum region that can occupy a significant fraction of the fan annulus, often extending over a large circumferential sector and a substantial portion of the span. This results in a total pressure distortion due to the viscous losses in the boundary layer and non-uniform flow angles, both radial and circumferential components, as shown in Figure 2.2.

As the distorted inlet flow approaches the engine, the incoming distortion is actively modified by the fan through a complex, three dimensional coupling between pressure fields and flow redistribution. The presence of low momentum regions within the inlet flow leads to a non-uniform work input across the annulus. Sectors characterized by reduced axial velocity experience higher aerodynamic loading, which results in a locally lower static pressure upstream of the rotor. This pressure imbalance drives a redistribution of mass flow both circumferentially and radially, with fluid migrating toward the low momentum regions. This can be seen in Figure 2.2b, where there are counter swirling (B) and co swirling (C) regions. This behaviour is schematized in Figure 2.2c and causes an attenuation of the axial velocity distortion through the machine.

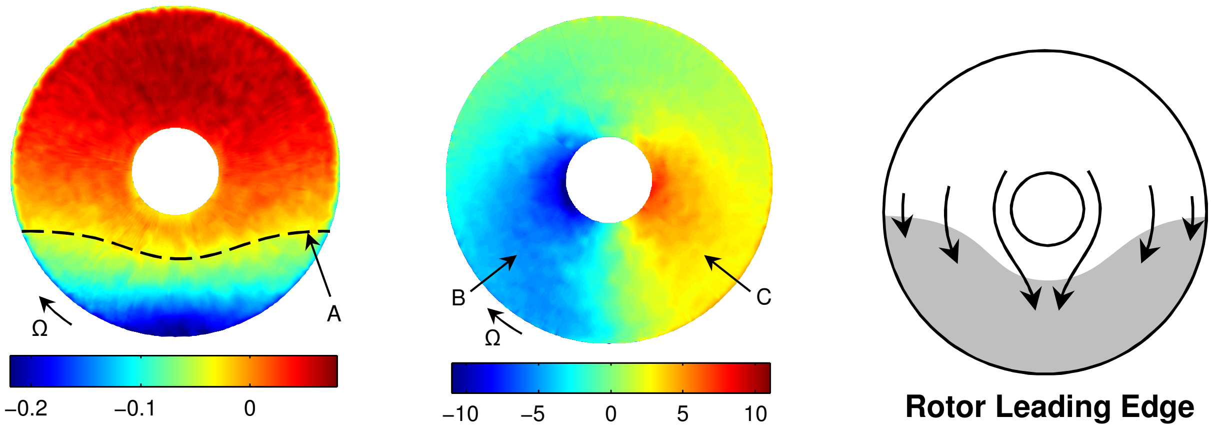

(a) Total pressure: $\frac{p_t - \bar{p_{t,3}}}{0.5\rho U_{mid}^2}$ (b) Absolute swirl angle: α (c) Flow redistribution

Figure 2.2: Distortion induced by BLI architecture at the engine inlet [13]

The ingestion of a distorted inflow has a pronounced impact on the aerodynamic behaviour of the fan stage, since it imposes a spatially varying inlet condition that forces different blade passages to operate under significantly different aerodynamic regimes. As the rotor blades traverse regions of varying inlet velocity and total pressure, they experience continuous changes in incidence angle and local loading. The flow has negative incidence on the rotor in the regions of co swirl and vice versa as clearly in Figure 2.3a at 25% blade span. The most important result from Figure 2.3a is that the rotor does not operate at its design conditions anywhere in the annulus.

Compared to the design value, the loading varies circumferentially by up to 20% as can be seen in Figure 2.3c. This is not a problem by itself, the problem is the associated variation in loss and hence the reduction in rotor efficiency [13].

Short nacelle high bypass turbofans (SNHB)

Next generation turbofan engine designs seek higher bypass ratios (BPR) and lower fan pressure ratios (FPR) for improved fuel burn and reduced emissions and noise. However, lower FPR require larger fan diameters, which increases the engine's contribution to overall aircraft drag and weight. To realize the fuel burn benefits of low FPR propulsors, shorter inlet and exhaust ducts are required to minimize these nacelle penalties. While shortening the inlet reduces external drag, it limits its diffusion capability, which can intensify inlet flow distortion.

A primary challenge unique to short inlets is the continuous decrease of effective flow area throughout the intake. In ultrashort configurations with extended spinners, the flow

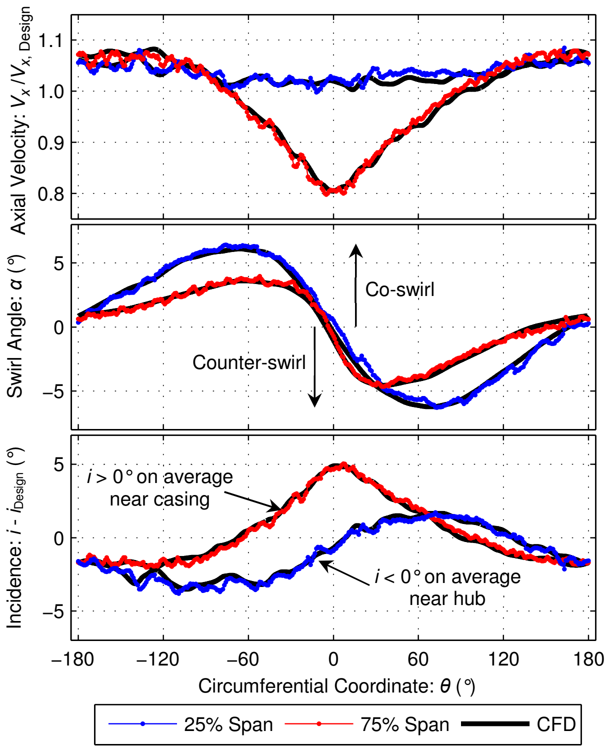

(a)

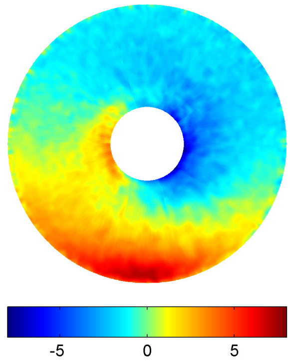

(b) Incidence: $i - i_{design}$

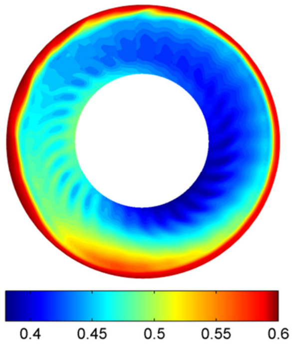

(c) Work input: $(h_{04} - h_{03})/U_{mid}^2$

Figure 2.3: (a) Measured and computed axial velocity, swirl and incidence variations at rotor inlet. (b)(c) Rotor incidence and work input [13]

area monotonically decreases up to the fan face. This lack of diffusion forces the flow to accelerate along the internal inlet surface, generating a localized region of high axial Mach numbers over the outer span near the shroud. This problem is intrinsic to the engine architecture and is present in all operating conditions.

In addition to cruise penalties, off design conditions such as high angle of attack (AOA) climbs are even more problematic in terms of efficiency reduction. The loss mechanisms in this operating condition can be schematized in three main effects [24]: rotor choking loss, Rotor–separation interaction loss (RSI) and variation in work input from radial flows.

The integration of short nacelle turbofans imposes a strict trade off between exterior aerodynamic drag and fan aerodynamic efficiency. Shortening the L/D ratio to values of around 0.25 [25] can effectively reduce nacelle drag and maintain propulsive efficiency, going beyond that generally causes the fan efficiency penalties to outweigh the benefits.

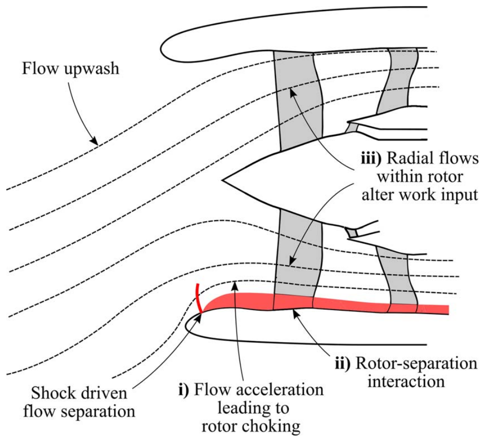

Figure 2.4: Schematic of key flow mechanism at high AOA [24]

2.2. Compressor behaviour under inlet distortion

Inlet flow distortions can generally be of three types: total temperature, total pressure and swirl distortion. Most of the research is focused on total pressure distortions, since they are the more pronounced ones in most applications, such as BLI engines and high angle of attack flight. Swirl distortions are also very common, such as in swirl ingestion from the fuselage or vortex ingestion, they often come coupled with total pressure distortions in most scenarios.

Although the shape of the inlet flow distortion can be complex and three dimensional, it is a useful simplification to divide them in radial and circumferential distortions, and approach them separately. Purely radial distortion can be treated with the methods developed for axisymmetric inlet flow, while circumferential distortions are the ones with a higher impact on performance and stability [20]. The distortions of most interest for compressor stability are those that occupy a large fraction of the annulus, the appropriate length scale for this behaviour is the radius of the machine [20].

In these conditions, the influence of viscous forces on the distorted velocity can be neglected, and the total pressure distribution at the compressor inlet will be the same as the one far upstream. The distortion is considered, for simplicity, as a simple square wave with equal circumferential extent of high and low pressure regions.

2.2.1. Upstream flow redistribution

Considering a pure total pressure distortion and uniform far upstream static pressure [20], the total pressure distortion is totally linked to a distortion of axial velocity (V_{ax}). Due to the axial velocity distortion, the compressor operates locally at different operating points. By considering the $\psi_{SS} = \Delta P_{SS}/\rho U^2$ versus flow coefficient $\phi = V_{ax}/U$ map, like the one in Figure 2.5b, the distorted region (lower V_{ax}) will work at a lower ϕ value, and thus at a higher ψ_{SS} value, due to the shape of the compressor curve.

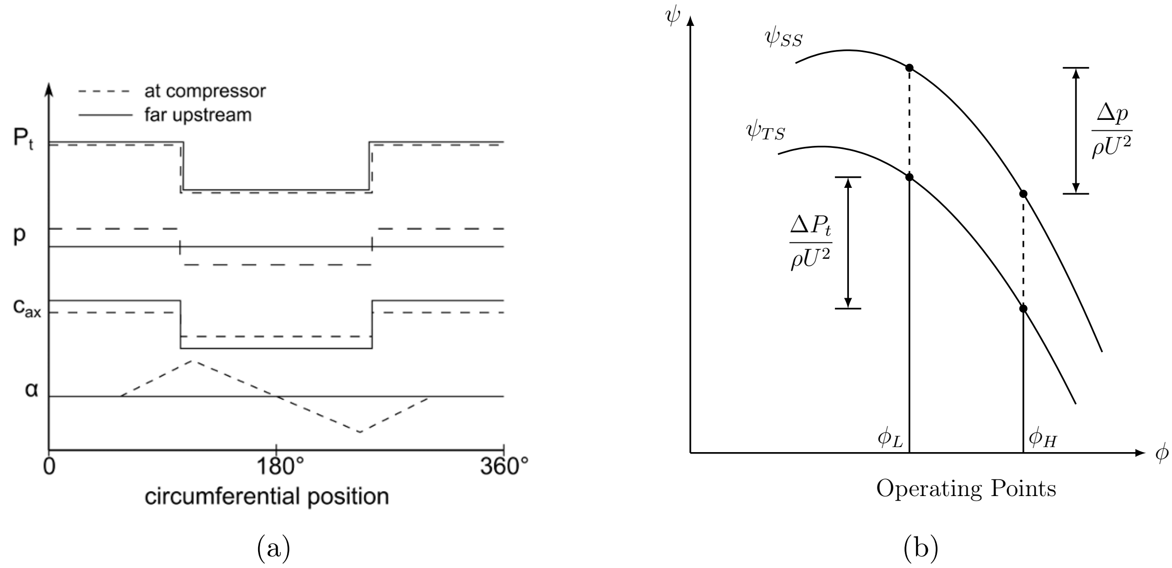

Figure 2.5: (a) Distribution of total pressure, static pressure, axial velocity and flow angle in two axial locations: far upstream and compressor inlet. [17] (b) ψ_{TS}, ψ_{SS} vs ϕ compressor map, showing the distorted sector operating point (ϕ_L) and the clean one (ϕ_H).

The outlet static pressure is assumed uniform, this assumption is valid under the conditions described by Gritzer [20]. The uniform outlet static pressure and different ψ_{SS} values imply that the static pressure in front of the distorted sector will have a lower value than the one in front of the clean one. Since the total pressure value does not change from far upstream to right in front of the compressor, this pressure gradient at the compressor inlet causes both an attenuation of the axial velocity distortion and the creation of tangential flows (swirl distortion).

The theoretical trend is shown in Figure 2.5a, where it is shown how the static pressure distortion caused by the compressor causes the flow to redistribute, creating a flow angle α distortion.

2.2.2. Impact on compressor performance

To better understand the influence of inlet flow distortion on the compressor stability limit, a simplified analytical model can be adopted to capture the underlying physical mechanisms. Among the available approaches, the simplest representation of compressor operation under distorted inlet conditions is the *parallel compressor model* (PCM), which, under suitable assumptions, provides valuable insight into the onset of instability and the associated performance degradation. The compressor is modelled as two compressors in parallel, operating on different conditions: one of relatively high inlet velocity and one of relatively low inlet velocity, as it would be behind a distortion screen. The model relies on three fundamental hypothesis [19]:

1. Each compressor operates on the undistorted characteristic
2. Circumferential cross flow is neglected
3. Uniform exit static pressure

The mass flow through each compressor depends both on the entity of the distortion, in terms of total pressure difference, and on the extent of the distorted region. Figure 2.6a shows a generic compressor map, on which the clean operating point is reported together with the two parallel compressors operating points, corresponding to the sectors of high (H) and low (L) inlet pressure. The overall distorted compressor operating point (M), computed as the area average of the compressors in parallel is shifted from the clean operating curve. The mean pressure rise is below the one in clean conditions at the same corrected mass flow.

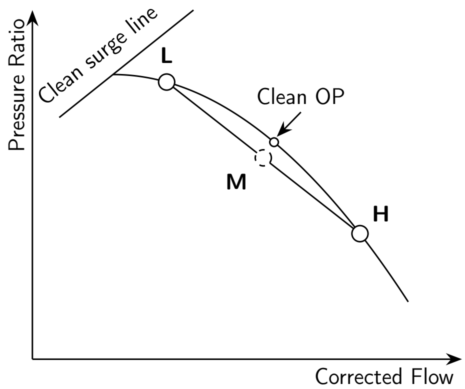

(a)

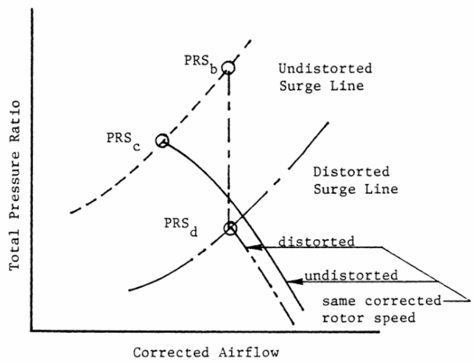

(b)

Figure 2.6: (a) Compressor map with compressors in parallel operating points. (b) Compressor distorted and clean characteristic showing pressure stall ratio in clean and distorted conditions [7]

Assumption 1 of the model implies that the distorted inflow compressor will surge if one of the parallel compressors operates on the clean surge line. Since the compressor representing the distorted sector operates at a lower corrected mass flow value, it will operate closest to the clean surge line, this results in a reduction of the overall compressor surge limit, as shown in Figure 2.6b. The distorted Surge line will be lower than the clean one, reducing the operational range on the machine. The parallel compressor model can also be used to predict the loss in stall pressure ratio due to the inlet distortion. The loss of stall pressure ratio can be defined as [7]:

$$\Delta PRS_N = \frac{PRS_c - PRS_d}{PRS_c} \tag{2.1}$$

Where PRS_d is the stall pressure ratio of the distorted compressor, and PRS_c is the stall pressure ratio of the clean compressor at the same engine speed. PRS_b is the stall pressure ratio of the clean compressor at the same corrected airflow, and it can be alternatively used to define the ΔPRS_N.

Given a total pressure inlet distortion, the loss of stall pressure ratio can be derived as follows [7]:

$$\Delta PRS_N = 1 - \frac{\frac{P_{\min}}{P_{\max}}}{1 - \frac{\theta_d}{2\pi}\left(1 - \frac{P_{\min}}{P_{\max}}\right)} \tag{2.2}$$

where P_{min} and P_{max} are respectively the minimum and maximum pressure values on the compressor annulus, and $\bar{P}$ is their average, weighted on the distorted sector extent θ_d. The above expression gives $\Delta PRS_N = 0$ for $\theta_d = 2\pi$ and $1 - P_{min}/P_{max}$ for $\theta_d = 0$. The highest loss is predicted to be for the smallest spoiled sector extent, this result highly deviates from the experimental data. Reid's research [27] showed how increasing the spoiled sector extent, the surge delivery static pressure reduces up to a certain angle value, the *critical sector angle*, after which it stays constant, as shown in Figure 2.7a.

In the research he also investigates the effects of dividing the spoiled area, showing how the worst possibility for compressor stability is one big sector, as opposed to many small sectors of the same total extent. A possible explanation of this behaviour is that the propagation and onset of stall is dependent on the duration of time each blade is operating in the distorted region.

Reid proposed to include the concept of the critical sector angle in the parallel compressor model to better predict the loss in stall pressure ratio. For inlet distortions narrower than θ_c the loss of pressure stall ration is set to be proportional to θ_d/θ_c, this is done by creating a distortion of size θ_c and defining a *minimum effective total pressure* P^e_{min} from the following equation:

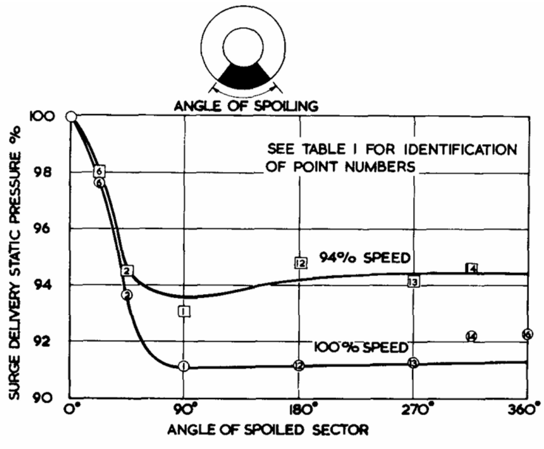

(a)

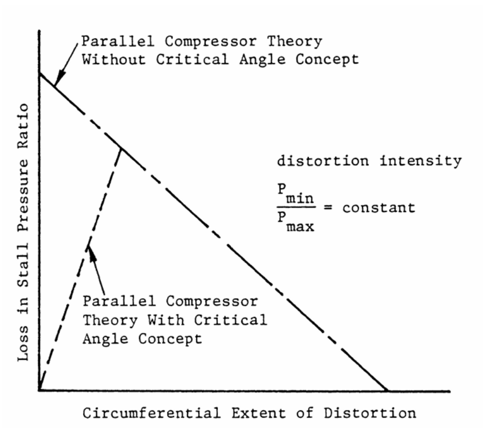

(b)

Figure 2.7: (a) Effects on the surge pressure ratio of varying the spoiled sector angle [27]. (b) Loss in pressure stall ratio prediction with and without critical angle concept [7]

$$\theta_c(P_{max} - P^e_{min}) = \theta_d(P_{max} - P_{min}) \tag{2.3}$$

Equation 2.2 can be modified to include this effect by replacing P_{min}/P_{max} with P^e_{min}/P_{max} when the distortion extent is lower than the critical angle [30]:

$$\Delta PRS_N = 1 - \frac{1 - \frac{\theta_d}{\theta_c}(1 - \frac{P_{min}}{P_{max}})}{1 - \frac{(\theta_d)^2}{2\pi\theta_c}(1 - \frac{P_{min}}{P_{max}})} \qquad \text{for } \theta_d < \theta_c \tag{2.4}$$

Results of the parallel compressor theory with and without critical angle concept for a constant distortion intensity are shown in Figure 2.7b. The implication of the Reid correction is that it is possible for a small section of the annulus to operate beyond the clean stability boundary, given that there is enough annulus operating in clean conditions, maintaining the overall stability.

3 | Experimental and numerical methodology

3.1. Experimental methodology

The von Karman Institute for Fluid Dynamics (VKI) has conducted an extensive experimental campaign to characterize the influence of inlet flow distortions on the aerodynamic performance and stability of an axial compressor. The campaign was conducted on the DREAM compressor, designed by Safran Aero Boosters as a research highly-loaded stage representative of the next generation boosters. The DREAM test section is a 1.5 stage, composed by an Inlet Guide Vane (IGV) row with 100 blades, a rotor with 76 blades and a stator with 100 blades [30]. Figure 3.1 shows a sectional view of the stage.

The DREAM test section is installed and tested within the VKI closed loop high speed compressor test rig: R4. The test rig permits at the test section inlet a total temperature control through a water heat exchanger and total pressure control through a pressure source and a vacuum pump. This allows an independent control of Reynolds and Mach numbers, allowing to test different operating conditions of the compressor (e.g. cruise, take-off).

3.1.1. Distortion screen

The total pressure distortion is generated through a non-uniform distortion screen and replicates real engine environments. The reference distortion pattern corresponds to the fan outlet flow of a ultra high bypass ratio and ultra high overall pressure ratio engine, corresponding to the physics described in Section 2.1. The distortion is only in total pressure. Considering the actual distortion pattern downstream of the fan under the specified operating conditions, a representative pattern was selected based on the portion of the flow most likely to affect the downstream axial compressor, which has a significantly

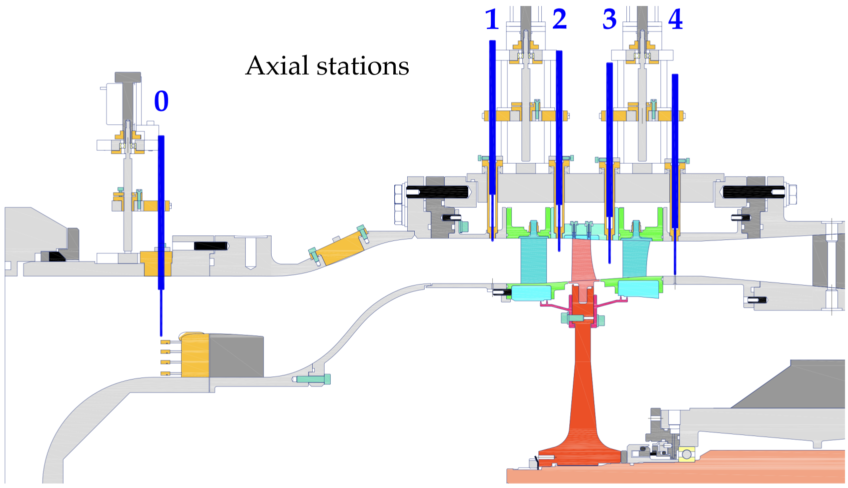

Figure 3.1: Cross sectional view of the DREAM test section, with the axial measurement planes: 0 (stage inlet), 1 (IGV inlet), 2 (IGV outlet/rotor inlet), 3 (rotor outlet/stator inlet), 4 (stage outlet) [30]

smaller mean diameter. The resulting distortion is therefore assumed to depend solely on the circumferential coordinate. Figure 3.2a shows the measured total pressure loss coefficient pattern.

The distortion screen is a metal wire mesh screen, it has been designed following a procedure aimed at achieving a specific total pressure loss, based on 1D correlations, function of it's porosity and wire diameter [30] [32].

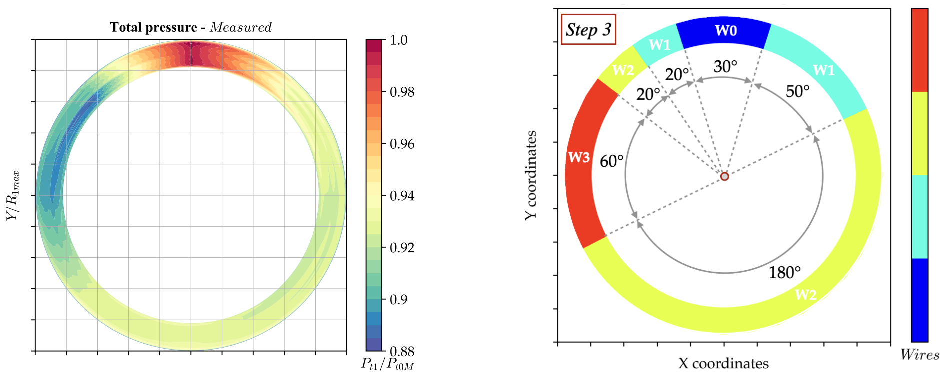

(a) (b)

Figure 3.2: (a): Measured distortion pattern as a fuction of K [30]. (b): Distortion screen geometry, output of the screen design process [30]

Figure 3.2b shows the distortion screen geometry, which is subdivided into six circumferential sectors. The sectors are defined using a set of four distinct wire mesh configurations (W0, W1, W2, and W3), which are distributed across the sectors as shown in the Figure 3.2b. Table 3.1 summarizes the geometric characteristics of each wire mesh type employed in the different sectors: wire diameter d_w, the distance between two wire centres (aperture) w and the mesh count n, which is the number of apertures per linear inch. The porosity β can be calculated from other quantities through equation 3.1.

$$\beta = (w^2)/(w+d) = 1 - \left(\frac{d_w \cdot n}{0.0254}\right)^2 \tag{3.1}$$

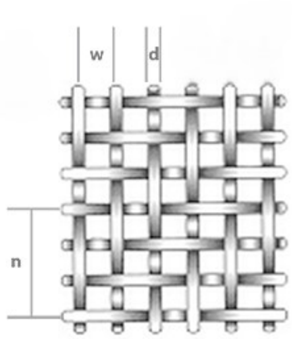

Figure 3.3: Metal mesh geometry

	W0 (clean)	W1	W2	W3
d_w [mm]	–	1.2	0.6	0.6
w [mm]	–	5.150	1.940	1.517
n	–	4	10	12
β	–	0.66	0.58	0.51

Table 3.1: Geometrical parameters of the wire mesh configurations

3.1.2. Distortion screen installation

The distortion screen was mounted right upstream of the experimental measurement Plane 1 (IGV inlet). This was done to limit modifications of the existing stage components, hence using predefined stage interfaces, and secondly to avoid the excessive dissipation of the distortion upstream of the IGV, in order to replicate as closely as possible the desired distortion at the IGV inlet. Figure 3.4 shows the meridional view of the facility with the screen mounting point. The screen is mounted one IGV axial chord upstream of the IGV itself.

The distortion screen is installed at a specific axial distance upstream of the IGV (ΔX), which is defined as a fraction of the mean diameter of the machine (D_m).

$$\Delta X_{norm} = \Delta X / D_m = 0.206$$

This geometrical parameter is of primary importance, as it governs the extent to which the redistribution mechanisms of the screen and the IGV are able to interact with each other. In particular, a smaller axial spacing may allow the potential field and the mass-flow redistribution generated by the IGV to influence the flow field at the screen location, altering the resulting distortion pattern.

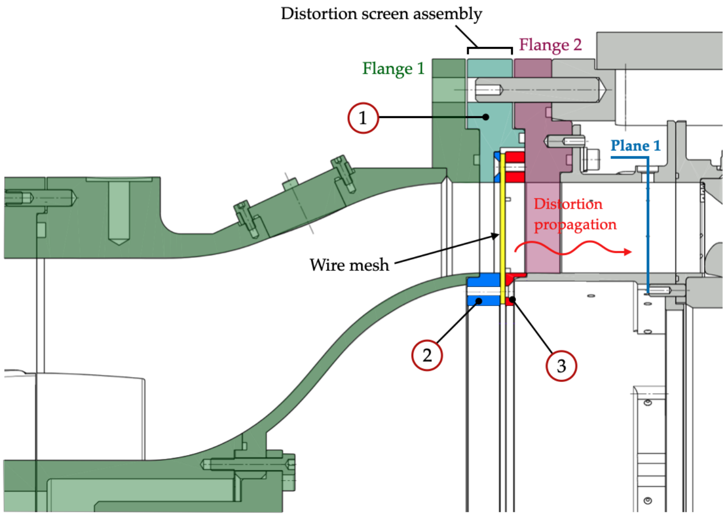

Figure 3.4: Meridional view of the compressor and positioning of the distortion screen assembly upstream of Measurement Plane 1. [30]

3.2. Experimental findings

3.2.1. Performance assessment

In the first stages of the experimental campaign, both the clean and distorted configurations have been characterized for multiple rotational speed and operating conditions. Figure 3.5 presents the total to total pressure ratio of the stage (π_{tt}) as a function of the corrected mass flow rate (W_{R1}), both referenced to the conditions at Plane 1. The distorted performance map shows that, contrary to classical expectations, the machine is capable of sustaining stable operation at corrected mass flow values below the clean stability limit. However, beyond the clean stability limit the stage does not exhibit a positive slope pressure rise characteristic; instead, the total pressure ratio decreases as mass flow is reduced, while the total temperature ratio increases, this behaviour is caused by the losses generated within the distorted regions of the annulus. This corresponds to a degradation of isentropic efficiency exceeding 10% relative to the clean design condition. The dominant mechanism driving this loss is the intensification of secondary flow structures, most notably the rotor hub corner separation, in the highly distorted sectors, where the elevated incidence angle promotes the growth of this separation to an extent comparable to the clean machine operating near its stability limit [30].

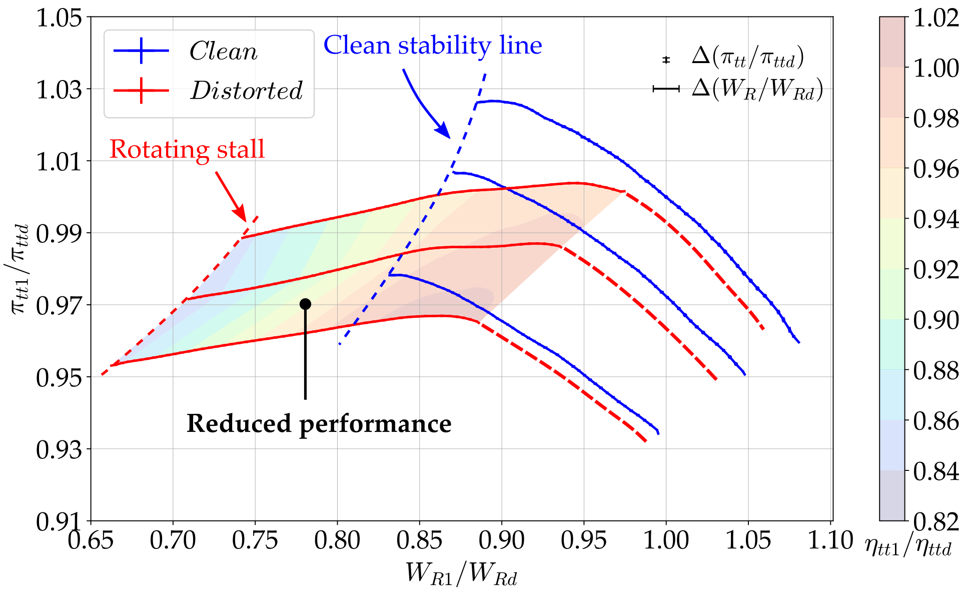

Figure 3.5: Compressor map of the stage with clean, distorted stability lines and the efficiency contour map. [30]

3.2.2. Comparison of Experimental and CFD Results

Steady and unsteady Reynolds Averaged Navier–Stokes (RANS/URANS) simulations were also carried out during the experimental campaign for the distorted configuration, in order to provide an interpretation of the experimental observations. A critical aspect of the domain definition is the choice of the upstream boundary location. The CFD domain was initiated at Plane 1, which coincides with the aerodynamic interface plane located at the IGV inlet, and corresponds to the experimental measurement plane situated immediately downstream of the distortion screen. This choice was driven by practical modelling considerations: Plane 1 represents one of the instrumented cross sections of the experimental facility, providing a detailed circumferential survey of total pressure, static pressure and Mach number, through pneumatic probe traverses. Furthermore, initiating the domain at this location avoids the need to model explicitly the distortion screen geometry and its associated complex loss mechanisms, including the pressure drop scaling with local velocity and the wire mesh aerodynamics. Experimental profiles of total pressure, total temperature and swirl angle, were imposed as inlet boundary conditions at Plane 1 [30]. Figure 3.6 presents a direct comparison of the circumferential distributions of four key flow quantities measured at Plane 1 (downstream of the distortion screen): the total pressure ratio P_t/P_{t0M}, the static pressure ratio P_s/P_{t0M}, the Mach number M, and the flow yaw angle. The total pressure distribution coincides given that the experimental profile was imposed as inlet boundary condition in the CFD. However, significant discrepancies are

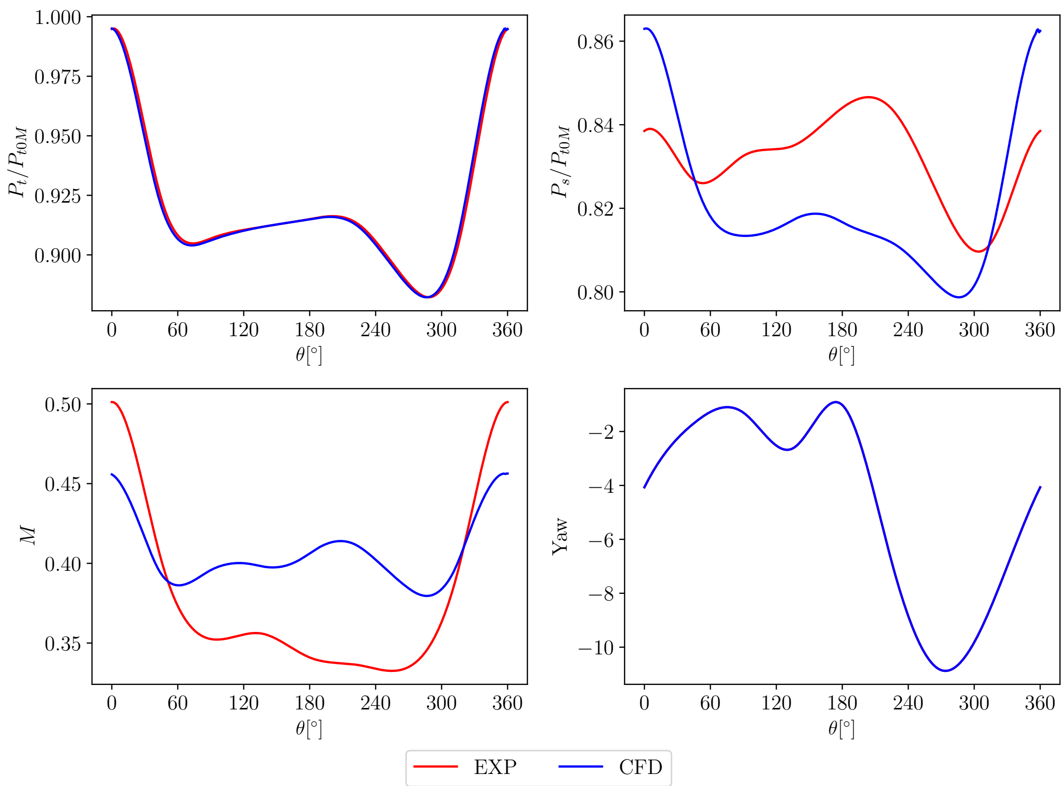

Figure 3.6: Comparison of CFD vs Experimental measurements at Plane 1 of total pressure, static pressure, mach number and yaw angle

evident in the static pressure and Mach number distributions. The CFD predicts a lower static pressure across the distorted sectors compared to the experimental measurements, while simultaneously over predicting the Mach number variation around the annulus. In the region of maximum distortion (270°–315°), the experimental static pressure remains substantially higher than the numerical prediction, and the corresponding experimental Mach number is 12% lower than the CFD value, indicating that the numerical simulation fails to capture the degree of circumferential flow redistribution actually present in the experiments.

The implications of the mismatch between CFD and experimental measurements for the downstream flow field are significant. The incorrect CFD velocity triangle at the IGV inlet leads to wrong incidence angles on the IGV blades, which in turn modify the deviation angles, the secondary flow intensity, and ultimately the rotor inlet conditions. Since rotor inlet incidence is the primary driver of hub corner separation growth and performance loss in the distorted configuration, the downstream mismatch between simulations and experiments is a direct consequence of the failure to capture the upstream redistribution.

3.3. Numerical methodology for screen assessment

To validate the analytical model, two-dimensional Computational Fluid Dynamics simulations were carried out in ANSYS Fluent. The CFD results serve as a reference solution against which the model predictions can be assessed, providing insight into the flow redistribution mechanisms that the model aims to capture.

3.3.1. Computational domain and boundary conditions

The strategy adopted to simulate the full annular duct consists of unrolling the annulus into a planar two-dimensional channel, in which the axial direction X represents the flow direction and the circumferential direction Y represents the unwrapped arc length of the annulus. Periodic boundary conditions are imposed on the top and bottom faces of the channel, so that the flow leaving one circumferential edge re-enters at the opposite edge with no phase shift. This setup is physically equivalent to a full 360° annular simulation: the periodicity enforces the same continuity of mass, momentum and total pressure that would hold across the closing plane of the annulus, while the two-dimensional planar geometry drastically reduces the mesh size and computational cost compared to a fully three dimensional annular model. The screen non-uniformity is therefore captured in its entirety, using an actuator disk approach in which all sectors of the screen are modelled. Further details about the distortion screen modelling are reported in the next paragraph.

The domain is divided into two axial sub-regions by the screen plane: an upstream block of length H and a downstream block of length $2H$, where H is the total circumferential height of the channel, equal to the unwrapped perimeter of the annulus at the screen mid-height. The asymmetric axial layout ensures that sufficient downstream length is available for the circumferential pressure gradients induced by the screen to relax towards a uniform state, consistent with the far-downstream hypothesis of the analytical model.

The boundary conditions are illustrated schematically in Figure 3.7 and are as follows:

- **Inlet**: total pressure $P_t = 116\,820$ Pa and total temperature $T_t = 293.05$ K are prescribed uniformly, consistent with the undistorted inflow hypothesis of the analytical model and equal to the measured inlet values.
- **Outlet**: a target mass flow rate is imposed. Because ANSYS Fluent internally treats the two-dimensional domain as having a unit depth in the third dimension (i.e. a reference out-of-plane thickness of $\Delta z = 1$ m), the mass flow rate entered in the solver is not the physical annular value but a scaled equivalent. Specifically, the

value $\dot{m}_{2D}$ is set so that the specific mass flow rate per unit area is preserved:

$$\frac{\dot{m}_{2D}}{H \cdot \Delta z} = \frac{\dot{m}_{real}}{A_{annulus}}, \tag{3.2}$$

where $A_{annulus}$ is the physical annular cross-sectional area of the Inlet duct and $\Delta z = 1$ m is the Fluent reference thickness. This ensures that the local velocity field – and hence the screen pressure drop – matches the real operating condition, even though the absolute mass flow value entered in the solver differs from the physical one.

- **Top and bottom faces**: periodic boundary conditions, which close the unrolled annulus and make the simulation equivalent to a full 360° computation.
- **Screen plane**: a porous jump interface positioned at $X = H$, modelling the pressure drop introduced by the wire mesh screen (see Section 3.3.2).
- **Front and Back**: symmetry boundary conditions

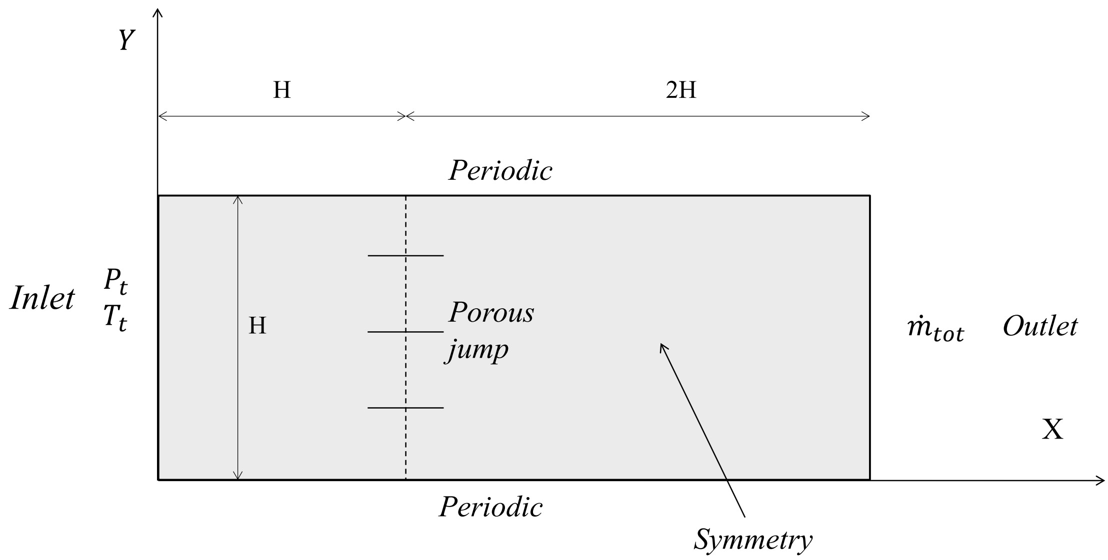

Figure 3.7: Two-dimensional CFD domain geometry and boundary conditions.

3.3.2. Screen modelling: porous jump boundary condition

The distortion screen is represented in ANSYS Fluent as a *porous jump* boundary condition, which acts as an infinitely thin actuator disk imposing a prescribed static pressure drop across the interface. This approach is well suited to the screen modelling problem, since the wire mesh is aerodynamically thin relative to the duct dimensions and the modelling of its detailed flow structure is not within the scope of the present work.

The Fluent porous jump formulation expresses the static pressure drop as:

$$\Delta p_s = -\left(C \cdot \frac{1}{2}\rho v^2\right) \Delta m, \tag{3.3}$$

where v is the face-normal velocity, ρ is the local density, Δm is the nominal thickness of the porous medium, and C is the inertial resistance coefficient specified by the user.

The analytical model expresses the screen loss in terms of a total pressure drop coefficient K_c relative to the isentropic dynamic head:

$$\Delta p_t = K_c \cdot (p_t - p_s) = K_c \cdot p_t \left(1 - \pi(M_1)^{-1}\right), \tag{3.4}$$

where $\pi(M)$ is the isentropic total-to-static pressure ratio:

$$\pi(M) = \left(1 + \frac{\gamma - 1}{2} M^2\right)^{\frac{\gamma}{\gamma-1}}. \tag{3.5}$$

To map the model coefficient K_c onto the Fluent coefficient C, the static pressure drops implied by the two formulations are equated, yielding:

$$C = \frac{K_c \cdot p_t(1 - \pi(M_1)^{-1}) \cdot \pi(M_2)}{\Delta m \cdot \frac{1}{2}\rho v^2}, \tag{3.6}$$

where M_1 and M_2 are the upstream and downstream Mach numbers at the screen face, respectively. A distinct value of C is assigned to each circumferential sector of the porous jump interface, reflecting the sector-dependent wire mesh properties (porosity and wire diameter).

3.3.3. Numerical setup

All simulations are performed with ANSYS Fluent using a *pressure-based solver* with the *coupled* pressure–velocity scheme. In the coupled formulation, the continuity and momentum equations are solved simultaneously rather than sequentially, which removes the approximate pressure–velocity decoupling inherent in segregated approaches such as SIMPLE and leads to superior convergence rates and robustness when strong pressure–velocity coupling is present [3]. For the subsonic Mach numbers encountered in the present simulations ($M \leq 0.6$), density variations are moderate and no shock waves are present, so the pressure-based coupled solver captures the compressible effects accurately without requiring the density-based solver, which is recommended primarily for high-speed flows involving shock resolution [3].

Air is modelled as a compressible ideal gas, so that density responds to local pressure and temperature variations through the equation of state $\rho = p/(RT_s)$. The remaining thermodynamic properties are held constant at standard ambient conditions, as summarised in Table 3.2.

The pseudo-time relaxation factors adopted for all simulations are listed in Table 3.3. The body-force relaxation factor is reduced to 0.5, below its default value, to improve solver stability near the porous jump interface, as discussed below.

Table 3.2: Air thermodynamic properties.

Property	Value	Unit
c_p	1006.43	$\mathrm{J\,kg^{-1}\,K^{-1}}$
λ	0.0242	$\mathrm{W\,m^{-1}\,K^{-1}}$
μ	1.8×10^{-5}	$\mathrm{kg\,m^{-1}\,s^{-1}}$

Table 3.3: Relaxation factors.

Variable	Factor
Pressure	0.5
Momentum	0.5
Density	1.0
Body Forces	0.5
Turbulent Kinetic Energy	0.75
Specific Dissipation Rate	0.75
Turbulent Viscosity	1.0

Spatial discretisation employs second-order upwind schemes for momentum, turbulent kinetic energy and specific dissipation rate, and a least-squares cell-based method for gradient reconstruction. The pressure interpolation scheme is set to *Body Force Weighted*, which is the recommended choice when concentrated body-force source terms are present in the momentum equations [3]. In Fluent, the porous jump boundary condition is internally implemented as a localised body force acting on the face-adjacent cells at the screen interface; the Body Force Weighted scheme accounts for this source term in the pressure interpolation stencil, improving accuracy and stability in the vicinity of the screen compared to the standard or linear schemes. For the same reason, the body force relaxation factor is lowered to 0.5: because the porous jump imposes a sharp, spatially concentrated pressure source, the corresponding body force term can introduce inter iteration oscillations near the screen interface. Reducing its relaxation factor damps these oscillations and allows the coupled solver to converge to a steady solution.

Turbulence is modelled with the SST k–ω formulation [22], which blends a k–ω closure near solid walls with k–ε behaviour in the free stream. It is important to note, however, that in the present simulation the turbulence model plays a secondary role with respect to the screen pressure losses. The total pressure drop introduced by the distortion screen is not the result of resolving the viscous flow around the individual wire filaments; instead, it is prescribed analytically and input directly into the momentum equations via the porous jump body force, whose magnitude is set from the empirical loss coefficient K_c. As a consequence, the turbulence model does not govern the screen losses, and its influence on the overall total pressure distribution is negligible.

The role of the SST k–ω model is therefore confined to capturing the turbulent mixing that occurs in the wake region downstream of the screen, where adjacent stream-tubes with significantly different axial velocities interact. Because the non-uniform loss distribution across the screen circumference produces large spanwise gradients of velocity and total pressure, intense shear layers develop at the boundaries between high and low loss sectors. The turbulence model governs the rate at which these shear layers diffuse and the circumferential non uniformity relaxes towards the uniform far downstream state. This mixing process is physically relevant to the downstream pressure equalisation, but it does not affect the magnitude of the losses themselves, which are set mainly by the porous jump formulation.

3.3.4. Mesh

Mesh topology and constraints

The porous jump boundary condition in ANSYS Fluent requires the screen to coincide exactly with a face shared between two adjacent cell layers; it cannot be positioned across the interior of a cell. This geometric constraint requires a structured quadrilateral mesh, in which cell face lines are aligned with the screen plane so that the interface is unambiguously defined along a single row of cell boundaries throughout the full circumferential extent of the domain. The mesh is generated using the ANSYS Fluent 2D meshing environment.

Mesh configurations

Two structured mesh configurations were investigated, differing in the distribution of cell spacing in the axial direction:

- **Uniform mesh**: square cells of uniform size are used throughout the entire domain. This configuration is straightforward to generate and produces cells with an aspect ratio of unity everywhere, but it distributes computational effort uniformly regardless of the local flow gradients.

- **Biased mesh**: the axial cell spacing is progressively reduced in the vicinity of the screen interface, using a geometric bias function, while larger cells are retained in the far-upstream and far-downstream regions where the flow is nearly uniform. This concentrates cells where the strongest circumferential pressure gradients and velocity redistributions occur. The refinement inevitably introduces high aspect ratio cells near the screen, but this is acceptable given that the dominant flow gradients in this region are axial. A fine axial resolution near the screen is physically justified: the redistribution of the flow between sectors occurs over a finite downstream length, and correctly capturing the axial decay of the circumferential non uniformity requires a sufficient number of cell layers in this region.

Grid convergence study

The sensitivity of the numerical solution to mesh refinement was assessed for both configurations using the Grid Convergence Index (GCI) methodology of Celik et al. [9], based on the Richardson extrapolation, was originally proposed by Roache [29]. Three successively refined meshes were generated for each configuration, maintaining a constant refinement ratio r between levels. The monitored quantity is the distortion coefficient DC, equation 3.7, evaluated at the far downstream plane. The details of the GCI procedure, including the definition of the apparent order of convergence p and the computation of the extrapolated value ϕ_{ext}, are reported by Celik et al. [9]

$$DC = \frac{P_{t,max} - P_{t,min}}{0.5\rho V_0^2} \tag{3.7}$$

The results of the two grid convergence studies are shown in Figure 3.8. For the uniform mesh, the GCI analysis yields an apparent order of convergence $p = 0.64$ and a Grid Convergence Index of 0.33%, with an extrapolated value $\phi_{ext} = 1.2505$. The low observed order of convergence, below the formal second-order accuracy of the spatial discretisation scheme, suggests that the uniform mesh does not refine efficiently: as the cell size is reduced uniformly across the whole domain, the solution improvement by refining the mesh is limited, since the majority of cells are added in regions where the solution is already well resolved.

In contrast, the biased mesh yields an apparent order of convergence $p = 2.16$ and a GCI of only 0.05%, with an extrapolated value $\phi_{ext} = 1.2508$. The observed order is consistent with, and slightly exceeds, the formal second order accuracy of the solver, which is characteristic of a well resolved solution operating in the asymptotic convergence

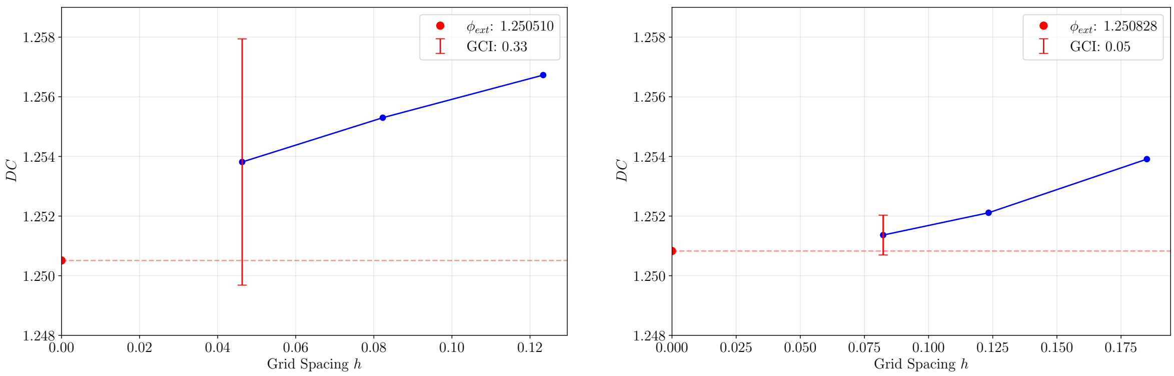

(a) Uniform mesh: $p = 0.64$, GCI $= 0.33\%$.

(b) Biased mesh: $p = 2.16$, GCI $= 0.05\%$.

Figure 3.8: Grid convergence study for the two mesh configurations. The blue curve shows the monitored quantity DC as a function of the normalised grid spacing h; the red dashed line and dot mark the Richardson-extrapolated value ϕ_{ext}; the red error bar indicates the GCI uncertainty band on the finest mesh.

regime. The GCI of 0.05% indicates that the discretisation uncertainty on the finest biased mesh is negligible relative to the physical quantities of interest.

On the basis of these results, the biased mesh is adopted for all simulations. The uniform mesh is retained only as a reference to illustrate the superior efficiency of the biased configuration.

3.4. Numerical methodology for IGV assessment

To assess the aerodynamic response of the IGV row under the non-uniform inlet conditions produced by the distortion screen, a dedicated set of CFD simulations was conducted in ANSYS Fluent. A full three-dimensional annular computation resolving all blade passages at once would be computationally prohibitive for the purposes of the present parametric study. A *2.5D* approach is therefore adopted, which retains the full circumferential extent of the annulus while limiting the radial discretisation to a single cell layer.

3.4.1. Computational domain and boundary conditions

The 2.5D computational domain is obtained by extracting a thin meridional strip of thickness equal to 1% of the total blade span from a three-dimensional full annulus mesh of the DREAM stage. Because the DREAM duct is aerodynamically convergent in the meridional plane (as visible in Figure 3.1), this thin strip retains the converging cross-sectional area of the original geometry: both the radial surfaces follow the meridional contours of the three-dimensional annulus, so that the local cross-sectional area of the 2.5D domain decreases in the axial direction exactly as it does in the full machine.

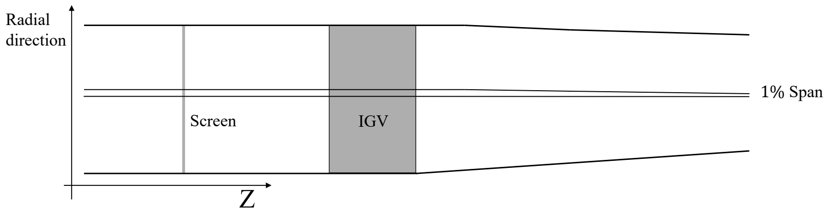

Figure 3.9: Meridional cross-section scheme of the 2.5D domain showing the porous jump interface and the IGV.

The domain includes the full 360° circumferential extent of the annulus, incorporating both the distortion screen and the IGV blade row, as illustrated in Figures 3.10 and 3.9. The screen is positioned upstream of the IGV at the same normalised axial distance employed in the experimental configuration ($\Delta X_{norm} = 0.206$), and the domain extends sufficiently far downstream of the IGV trailing edge to avoid effects of the domain boundary on the redistribution mechanism.

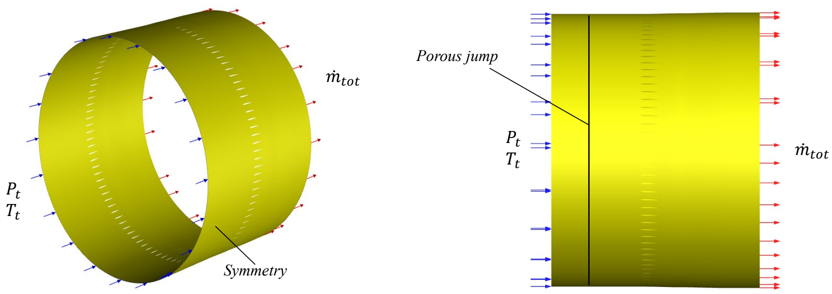

Figure 3.10: Three-dimensional view of the 2.5D annular domain showing the inlet boundary conditions (P_t, T_t) and the outlet mass flow rate $\dot{m}_{tot}$.

The boundary conditions are consistent with those described for the screen assessment simulations (Section 3.3.1) and are applied as follows:

- **Inlet**: uniform total pressure $P_t = 116\,820$ Pa and total temperature $T_t = 293.05$ K are imposed at the upstream face of the domain, replicating an undistorted far-field inflow condition upstream of the screen.
- **Outlet**: a target total mass flow rate $\dot{m}_{tot}$ is prescribed at the downstream outlet plane. Because the 2.5D domain represents only 1% of the full blade span, the mass flow rate imposed in the solver is scaled accordingly, so that the specific mass flux per unit area is preserved relative to the physical machine.

- **Lateral (radial) faces**: symmetry boundary conditions are applied to the two faces bounding the domain in the radial direction.
- **Screen interface**: the distortion screen is represented by the same porous jump boundary condition described in Section 3.3.2, with sector-dependent inertial resistance coefficients C assigned in accordance with the wire mesh properties of each circumferential sector.
- **Blade surfaces**: no-slip, adiabatic wall conditions are applied to the IGV blade surfaces.

3.4.2. Numerical setup

The numerical setup of the 2.5D IGV simulations follows the same configuration as described in Section 3.3.3 for the screen assessment simulations. All computations are performed in ANSYS Fluent using a *pressure-based solver* with the *coupled* pressure–velocity formulation. Air is treated as a compressible ideal gas, with thermodynamic properties held constant at the values reported in Table 3.2. Turbulence is modelled with the SST k–ω closure [22], which provides a physically appropriate treatment both in the near-wall blade boundary layers and in the free-stream mixing regions between sectors.

Spatial discretisation employs the same second-order upwind schemes for momentum, turbulent kinetic energy, and specific dissipation rate as used in the screen simulations, together with a least-squares cell-based gradient reconstruction method. The *Body Force Weighted* pressure interpolation scheme is again selected to ensure stability and accuracy in the vicinity of the porous jump interface. The pseudo-time relaxation factors are identical to those reported in Table 3.3.

3.4.3. Mesh

Screen section mesh

The outer domain mesh, encompassing the region upstream of the IGV and downstream of the blade passages, is structured and generated using the ANSYS Fluent meshing environment, following the same approach described in Section 3.3.4. In particular, the mesh in the axial region between the distortion screen and the IGV leading edge is constructed with an axial bias function, concentrating cell density near the screen interface to correctly capture the sharp circumferential pressure gradients imposed by the porous jump. This upstream mesh topology is consistent with the biased mesh configuration selected on the basis of the grid convergence study reported in Section 3.3.4, and the cell spacing in this region is held at the same density as in the validated screen assessment simulations.

IGV blade passage mesh

The mesh within the IGV blade passages was not generated from scratch for this study. Instead, a pre-existing structured mesh, originally developed and optimised for three-dimensional RANS simulations of the DREAM IGV, was adopted [30]. This mesh had previously undergone a dedicated grid convergence study; it is therefore considered sufficiently resolved for the purposes of the present investigation.

The blade passage mesh is a multi-block structured grid, generated using Cadence AutoGrid5 and IGG softwares. The mesh of a single channel, in the Blade-to-Blade (B2B) plane, is generated by seven blocks per blade row: a O4H topology characterized by five blocks surrounding the blade plus two inlet/outlet blocks located adjacent to the interface of the next row [30]. Figure 3.11 shows a close-up view of the mesh in the blade passage region, illustrating the *O*-grid refinement around the leading and trailing edges and the smooth transition to the passage interior cells.

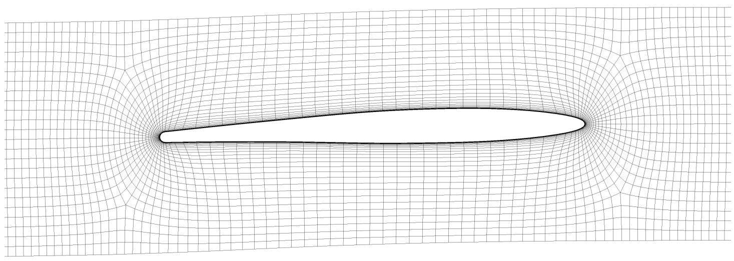

Figure 3.11: Close-up view of the structured blade passage mesh around the IGV profile.

The 2.5D domain mesh is assembled by extruding both the upstream domain mesh and the blade passage mesh by a single cell in the radial direction, with the radial extent set to 1% of the full blade span.

The resulting mesh constitutes a single-layer three-dimensional representation of the full annular flow field, retaining the correct circumferential periodicity, the convergent meridional geometry, and the resolved blade passage topology, at a computational cost several orders of magnitude lower than a full three-dimensional annular simulation.

4 | Single Screen Model

This chapter presents the analytical model developed to predict the circumferential flow redistribution produced by a non-uniform distortion screen in an annular duct. The spatial discretization, physical hypothesis and model inputs are initially discussed, the total pressure loss correlation is described in depth, and a parametric validation against experimental data is presented. Then the model structure and iterative solution algorithm are described. Finally, the model results are presented for the screen configuration used at VKI. The results are then compared to the CFD simulations run with only the distortion screen and the experimental data obtained from the test campaign.

4.1. Spatial discretization

4.1.1. Circumferential sectors

The distortion screen of the VKI R4 facility is composed of four distinct wire mesh configurations, denoted W0, W1, W2, and W3, distributed over six circumferential sectors of different angular widths, as described in Chapter 4 in Figure 3.2b. Since each mesh type has uniform geometric properties within its own sector, the model associates one stream-tube with each distinct mesh type. This is not a modelling limit, since the mass-flow through each stream-tube is not imposed, and the stream-tube cross sectional area far upstream and far downstream is allowed to vary to preserve total mass-flow. Each stream-tube is representing the amount of mass-flow going through a single screen sector, but the value of said mass-flow is a model outut and depends on the blockage imposed by the different screen sectors. The annulus is therefore discretised into four stream-tubes, indexed $i \in \{\mathrm{W0}, \mathrm{W1}, \mathrm{W2}, \mathrm{W3}\}$, each occupying an angular extent $\Delta\theta_i$ that corresponds to a cross sectional area A_i:

$$A_i = \frac{\Delta\theta_i}{360^\circ} \cdot S \tag{4.1}$$

where S is the total annular cross-sectional area of the duct at the screen plane (Plane 1). The circumferential extents $\Delta\theta_i$ are identical to the screen sectors extent on the upstream and downstream stations of the screen, since no area change is imposed across the mesh, while they are calculated for the far upstream and downstream stations, as a consequence of mass flow conservation.

For each stream-tube, the mass flow is conserved but not set to a fixed values, instead it is a result of the flow redistribution. The total mass flow, sum of the ones of the single stream-tubes, is, instead, set to a fixed value.

4.1.2. Axial stations

The model domain spans from a far-upstream reference plane to a far-downstream plane. Four distinct axial stations are defined along each stream-tube:

- **Station 1 – Far upstream**: Located sufficiently far upstream of the screen for the flow to be considered circumferentially uniform in static pressure.
- **Station 2 – Screen upstream**: Located immediately upstream of the screen. This is the station where the loss correlations are evaluated, since the local Mach number, Reynolds number and dynamic pressure involved in the calculation of the loss coefficient are those of the inlet flow.
- **Station 3 – Screen downstream**: Located immediately downstream of the screen. The total pressure at Station 3 is reduced relative to Station 2 by the screen pressure drop coefficient K_c, computed from the local loss correlations.
- **Station 4 – Far downstream**: Located sufficiently far downstream of the screen for the static pressure to be circumferentially uniform.

The four station and multiple segment structure is represented schematically in Figure 4.1, which shows the flow path through each stream-tube, and a qualitative representation of the stations axial position. The variable θ and X are respectively the circumferential and axial coordinates. The circumferential extent of each sector in Figure 4.1 is only qualitative.

4.2. Physical hypotheses

The following physical hypotheses are adopted in the model:

1. **Losses are only generated by the screen**, modelled through empirical loss

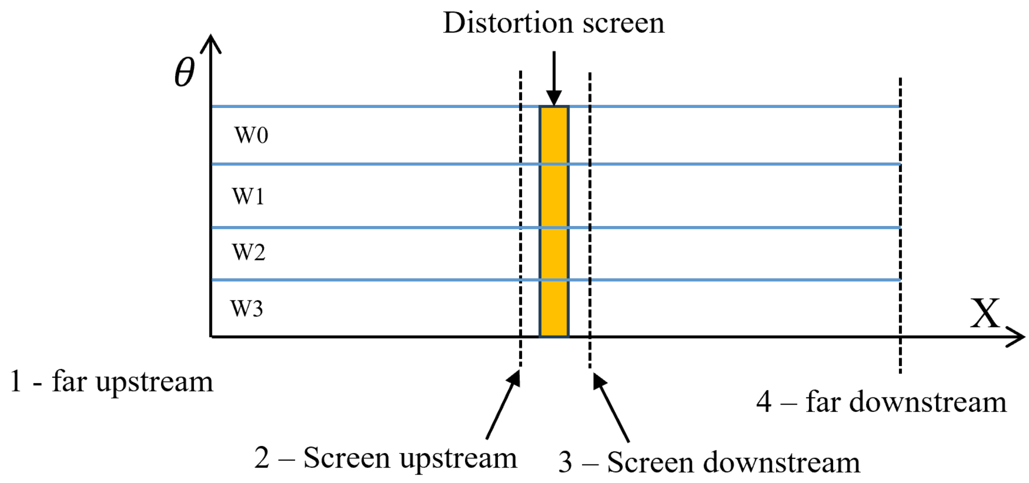

Figure 4.1: Analytical model schematics, showing the multiple station and segment approach

correlations. This results in an isentropic flow within each stream-tube, except across the screen. The total pressure is conserved along each stream-tube on both the upstream and downstream sides of the screen.

2. **Circumferential discretisation into independent stream-tubes.** The annulus is subdivided into a finite number of circumferential sectors, each treated as an independent one dimensional stream-tube, and one dimensional screen losses correlations are used. Mass, momentum and energy are exchanged between sectors only indirectly, through the static pressure hypothesis, rather than through explicit cross-flow terms.

3. **Steady flow.** All quantities are time-averaged; no unsteady effects are considered.

4. **Uniform total pressure at the inlet.** The far-upstream inlet total pressure $P_{t,\infty}$ is assumed to be circumferentially uniform, consistent with a clean, undistorted inflow upstream of the screen (the values corresponds to the uniform total pressure value experimentally measured at Plane 0).

5. **Uniform static pressure at the outlet.** The far downstream static pressure is assumed to be circumferentially uniform, leaving only total pressure (and thus Mach number) distortion.

6. **Axially thin screen**. The stream-tube cross sectional area does not change between section 2 and 3. In these axial stations, the cross sectional area of the stream-tubes corresponds to the cross sectional area of the distortion screen sectors.

7. **Antisymmetric static pressure condition across the screen.** The static pressure in the immediate vicinity of the screen is assumed to satisfy an antisymmetric relation: the pressure averaged between planes 2 and 3 is a constant across the entire screen:
$$\frac{P_{s2,i}+P_{s3,i}}{2}=\overline{\left(\frac{P_{s2}+P_{s3}}{2}\right)}=\overline{P}_{avg}\quad\forall\, i, \tag{4.2}$$
where subscripts 2 and 3 denote the upstream and downstream faces of the screen, respectively, as described in Section 4.1.2. The $\overline{P}_{avg}$ value is a result of the calculation, not set to a specific value. This hypothesis implies that the static pressure does not equalise immediately downstream of the screen, but rather at a plane further downstream. The validation and all considerations behind this hypothesis are reported and analysed in detail in Section 4.3.
8. **Zero swirl angle.** The flow is assumed to be purely axial at all stations ($\alpha = 0$), so that the axial velocity equals the total velocity: $V_{ax} = V$. This implies that kinetic energy from transverse components of velocity is negligible.
9. **Calorically perfect gas.** Air is treated as a calorically perfect gas with specific heat ratio γ and specific gas constant R, both constant throughout the domain.

4.3. The antisymmetric static pressure hypothesis

The closing condition of the system is provided by the antisymmetric static pressure hypothesis introduced in Section 4.2. Rather than enforcing full static pressure equalization at the screen exit, the model enforces that the average of the upstream and downstream static pressures is circumferentially uniform:

$$\frac{P_{s,2,i}+P_{s,3,i}}{2}=\overline{P}_{avg},\quad\forall\, i, \tag{4.3}$$

where $\overline{P}_{avg}$ is the circumferential average of the left hand side of the quation, common to all sectors.

This assumption has first been introduced by Gillespiere [11]. However, to verify the validity of such hypothesis, a CFD simulation has been performed in a simplified configuration with only two sectors: a clean and a distorted one. The results of the simulations are reported in Figure 4.2, which shows the two-dimensional distribution of the normalised static pressure P_s/P_{ref} in the X–Y plane. The black line represents the distortion screen, where the total pressure drop is imposed. The colourmap reveals a clear spatial anti symmetry between the upstream and downstream pressure fields in the distorted sector:

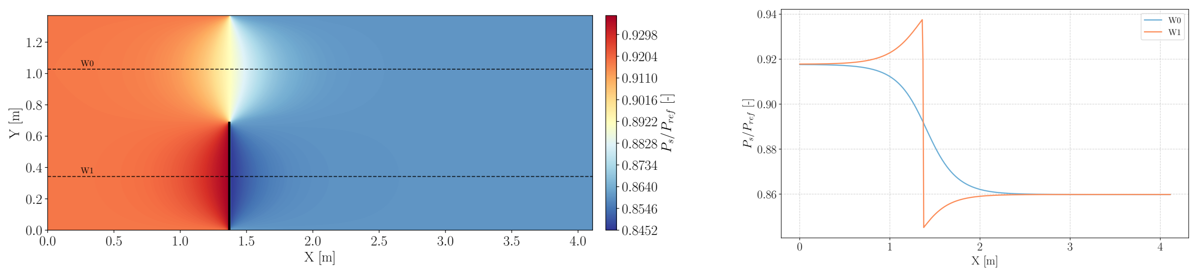

(a) (b)

Figure 4.2: (a) Two dimensional colour map of the adimensional static pressure in the X–Y plane. The black line represents the distortion screen, where the total pressure jump is imposed. (b) Adimensional static pressure values P_s/P_{ref} versus axial coordinate X, extracted from the two axial lines W0, W1 shown in the colour map.

it exhibits an elevated static pressure level immediately upstream of the screen and a reduced level just downstream. The clean sector, where no pressure jump is imposed, shows a gradual static pressure gradient.

4.4. Model inputs

The inputs required by the single screen model are listed below:

- **Total mass flow** $\dot{m}_{tot}$: the total mass flow through the annulus.
- **Inlet total pressure** $P_{t,0}$
- **Inlet total temperature** $T_{t,0}$
- **Screen geometric data**: for each sector i,the wire diameter $d_{w,i}$, the angular extent $\Delta\theta_i$ and the porosity β_i, defined as the ratio of the open area to the total area.
- **Duct geometry**: the total annular cross-sectional area S at all the axial stations.
- **Fluid properties**: the specific heat ratio γ, the specific gas constant R, and the dynamic viscosity μ.

These inputs correspond to the quantities that are available from the design specification of the VKI R4 distortion screen and from the operating condition of the test rig.

4.5. Screen loss correlation

When developing a model for woven screens into duct flow systems, the accurate estimation of the pressure drop across the mesh is essential for predicting overall flow characteristics and having results that can be compared to the experimental data. This section aims to develop a total pressure loss correlation that decouples the individual contributions of geometry, Reynolds number, and Mach number. By isolating each variable, a parametric study can be carried out to identify the combination of correlations that best matches the experimental data.

Because the current experimental setup utilizes a single wire mesh, the "flow around" approach is adopted. This approach treats the flow through the mesh by analogy to the flow around isolated cylinders. This is the standard and most accurate methodology for single screens. The approach was formally expanded by Wieghardt [32], who applied empirical drag coefficients of isolated transverse cylinders to single woven round wires. In this correlation, resistance is expressed as a pressure loss coefficient (K_c), defined as the ratio of total pressure drop to the dynamic pressure of the approaching unperturbed flow.

$$K_c = \frac{p_{t2} - p_{t1}}{p_{t1} - p_1} \tag{4.4}$$

To reliably predict this pressure loss coefficient across a wide spectrum of varying operating conditions, the overall aerodynamic resistance must be decomposed into a series of independent correlating functions, each accounting for the distinct influences of the screen's geometric porosity β, the viscous and inertial forces captured by the Reynolds number Re_d, and the fluid compressibility dictated by the inlet Mach number M [26].

$$K_c = G(\beta) \cdot F(Re_d) \cdot f_M(M) \tag{4.5}$$

The total pressure drop across the screen for each sector is expressed in terms of the isentropic dynamic head:

$$P_{t,3,i} = P_{t,2,i} - K_{c,i} \cdot P_{t,2,i} \cdot \left(1 - f_\gamma(M_{2,i})^{-1}\right), \tag{4.6}$$

where the term $P_{t,2,i}\left(1 - f_\gamma^{-1}\right) = P_{t,2,i} - P_{s,2,i}$ is the compressible dynamic pressure.

Porosity Function

The screen porosity function, denoted as $G(\beta)$, isolates the geometric effects of the wire mesh. The porosity β is defined as the fraction of open area, calculated using an orthogonal projection of the screen, resulting in orthogonal porosity.

Various mathematical forms for the porosity function exist in the literature to normalize the pressure loss. Pinker and Herbert [26], as well as other reviews [4], identified four primary geometric parameters:

$$\begin{cases} G_1(\beta) = \dfrac{1-\beta}{\beta^2} \\ G_2(\beta) = \dfrac{1-\beta^2}{\beta^2} \\ G_3(\beta) = \dfrac{1-\beta}{\beta} \\ G_4(\beta) = \dfrac{(1-\beta)^2}{\beta^2} \end{cases}$$

Despite the variety of formulations, extensive experimental validation has repeatedly shown that normalizing the loss coefficient using the function $G_2(\beta)$ provides the most effective and consistent data correlation [26].

Reynolds number Function

The Reynolds number function, $F(Re)$, accounts for the balance of viscous and inertial forces as the fluid flows around the wire matrices. This function is most frequently correlated using a Reynolds number based on the wire diameter, calculated from equation 4.7.

$$Re_d = \frac{\rho U_0 d_w}{\mu} \tag{4.7}$$

The pressure loss correlation typically takes the form of a summation of two terms: one describing the viscous, laminar contributions, and another describing the inertial, turbulent contributions.

Table 4.1 reports the equations of eight Reynolds functions from their respective authors. Most of them share the same structure, being different only in the coefficients, which were calibrated on experimental data.

While these models utilize different exponents and coefficients, they all demonstrate that the pressure loss coefficient decreases continuously with an increase in flow velocity. More importantly, as the Reynolds number becomes large and the flow enters a fully turbulent

Authors	$\mathbf{F(Re_d)}$
Annand (1953) [2]	$0.484 + \left(8.665\ Re_d^{-0.7847}\right)$
Roach (1987) [28]	$0.52 + \left(66\ Re_d^{-4/3}\right)$
Groth and Johansson (1988) [12]	$0.4 + \left(8.4\ Re_d^{-4/5}\right)$
Wakeland and Keolian (2003) [31]	$0.4 + \left(11.5\ Re_d^{-1}\right)$
Kurian and Fransson (2009) [16]	$0.5 + \left(26\ Re_d^{-1}\right)$
Brundrett (1993) [6]	$\left(7\ Re_d^{-1}\right) + \left(0.9\ (\log_{10}(Re_d + 1.25))^{-1}\right) + (0.05\ \log_{10}(Re_d))$
Bailey et al. (2003) [5]	$\left(18\ Re_d^{-1}\right) + \left(0.75\ (\log_{10}(Re_d + 1.25))^{-1}\right) + (0.055\ \log_{10}(Re_d))$
Azizi (2019) [4]	$0.4537 + 10.76\ Re_d^{-0.8213}$

Table 4.1: Reynolds functions from eight authors

regime, the friction losses become independent of the flow and the function converges to a constant value.

However, a comparison of these models reveals that they exhibit different convergence values and trends at high Reynolds numbers ($Re_d > 1000$). The asymptotic plateau values reported in the literature fluctuate significantly, generally falling between 0.4 and 0.63. Figure 4.3 reports the trends of $F(Re_d)$ versus Re for all the considered function shapes.

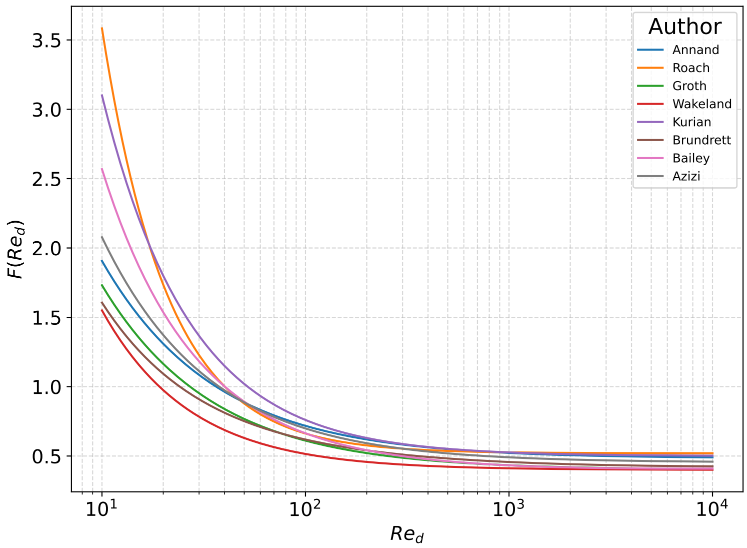

Figure 4.3: Trend of the Reynolds functions of Table 4.1

Mach Number Function

For experiments conducted at higher duct velocities, compressibility becomes a dominant factor. When the inlet Mach number causes the compressibility effects in the wire mesh to be significant, the experiments deviate from the incompressible correlations, which only accounted for porosity and Reynolds effects. A critical contribution to this field by Pinker and Herbert [26] was the isolation of the inlet Mach number's effect from the Reynolds number and porosity, variables that had been heavily mixed in previous literature accounting for the Mach number effect [1]. With this approach, the variations due to Mach number are evaluated independently of the specific value of the Reynolds number.

Therefore, for compressible flows, a reliable prediction strategy involves initially calculating an incompressible pressure loss coefficient (K_0) based solely on the screen's porosity and Reynolds number. Once this baseline is established, a compressibility correction ratio, defined as the compressible total pressure loss over the incompressible loss (K_c/K_0), is applied as a direct function of the inlet Mach number. This decoupled approach ensures that the total pressure loss across the distortion screen can be reliably determined across a wide range of operating conditions. Figure 4.4 shows the Mach number function reported by Pinker and Herbert [26], obtained by interpolating experimental pressure-loss measurements taken across a range of Mach numbers for several distortion screens. The trend is function of both the Mach number and the porosity value.

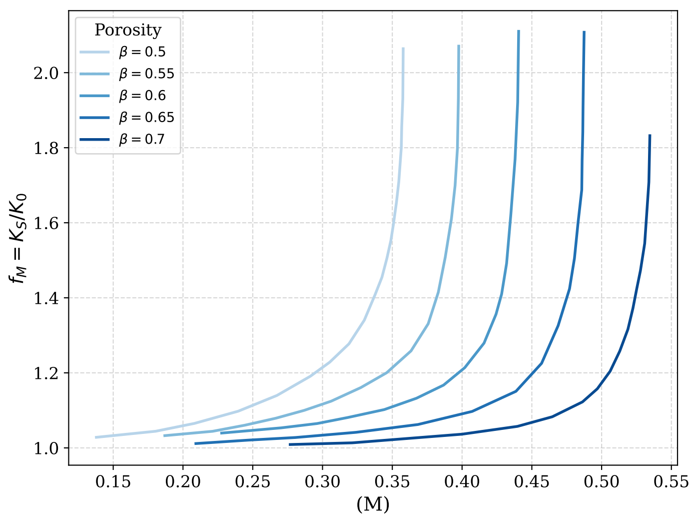

Figure 4.4: Trend of the Mach number correction function, as function of Mach number and screen porosity [26]

As observed in the plotted curves, the compressibility correction ratio approaches a vertical asymptote for each given porosity. This asymptotic behaviour is caused by the onset of aerodynamic choking within the restrictions of the distortion screen, a condition where the pressure loss coefficient theoretically rises to infinity. The specific inlet Mach number at which this phenomenon occurs is defined as the choking Mach number (M^*).

When attempting to correlate M^* with the screen geometry, it was observed that the traditional orthogonal porosity significantly underestimates the effective minimum flow area. To provide a more physically representative model, that more accurately represents the tridimensional shape of the metal wire mesh, Pinker and Herbert [26] proposed an alternative approach known as "sinusoidal porosity". This formulation assumes that the centreline of each wire is bent into a sine wave, the resulting porosity is calculated with equation 4.8, where m is the mesh count and d_w is the wire diameter. By modelling the mesh in this manner, the bounding curves in the plane of the minimum flow area do not overlap, which correctly results in a larger calculated open area, as shown in Figure 4.5. Consequently, to accurately predict the choking Mach number, this sinusoidal representation must be used instead of the traditional one dimensional orthogonal projection.

$$\alpha' = 1 - \frac{2}{\pi^2}\left\{(1+2N^2)\left(\frac{\pi}{2} - \cos^{-1} N\right) + 3N\sqrt{(1-N^2)}\right\} \tag{4.8}$$
$$N = \pi m d/2$$

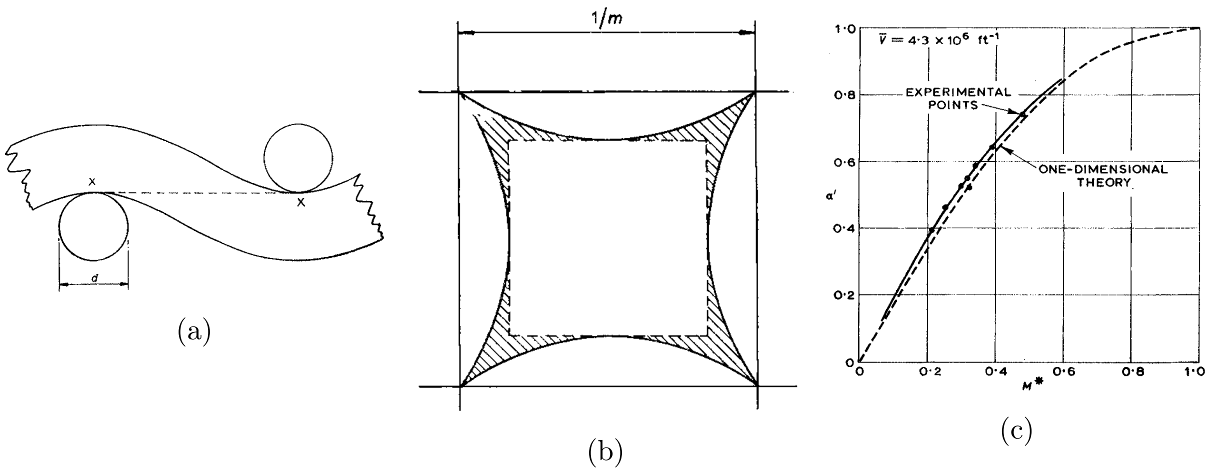

Figure 4.5: (a) Sinusoidal shape of the wire centreline [26]. (b) Minimum flow area in plane X-X. Shaded area is the underestimate in porosity by orthogonal projection [26]. (c) Choking Mach number versus sinusoidal porosity. Experimental points, their interpolation and one dimensional theory curve [26].

To theoretically predict the choking Mach number for a given wire mesh, the principles of one dimensional isentropic flow are utilized [15]. By treating the open passages of the mesh as the throat of a nozzle where sonic conditions are reached, the ratio of the upstream unperturbed duct area to the minimum flow area can be equated to the standard isentropic area ratio (A/A^*). Substituting the sinusoidal porosity (α') as the area ratio, the choking Mach number is computed by solving the following equation:

$$\frac{1}{\alpha'} = \frac{1}{M^*}\left[\frac{2}{\gamma+1}\left(1+\frac{\gamma-1}{2}M^{*2}\right)\right]^{\frac{\gamma+1}{2(\gamma-1)}} \tag{4.9}$$

where γ is the specific heat ratio of the fluid. Pinker [26] conducted an extensive experimental study to validate this theoretical limit. Their results demonstrated that the one dimensional theory (Calculating M^* from Equation 4.9), closely align with their experimental results when the sinusoidal porosity (α') is used. Figure 4.5c shows the comparison between the experimental and analytic approaches, proving their good matching. However, a slight discrepancy remains between the theoretical prediction and the empirical data. This deviation occurs because the flow passing through the woven interstices undergoes flow separation, forming a *vena contracta*. As a result, the effective area is slightly smaller than the purely geometric open area, indicating that the mesh behaves as a choked passage with a discharge coefficient slightly below unity (typically around 0.95). Consequently, the actual aerodynamic choking of the gauze occurs at a marginally lower inlet Mach number (M) than the ideal one dimensional theory predicts.

4.5.1. Validation with experimental data

The analytical model developed in the preceding sections is validated against the experimental measurements acquired through the VKI R4 facility. The quantity of interest for this comparison is the circumferential distribution of the normalised total pressure ratio P_t/P_{t0M} at the measurement Plane 1, located immediately downstream of the distortion screen. Experimental data are available for seven distinct operating conditions, covering a range of corrected mass flow rates representative of the compressor map described in Chapter 3. The complete set of comparisons for all operating conditions is reported in Appendix A, while the present section focuses on a representative case (Case 7, $\dot{m} = 9.254$ kg/s) to illustrate the behaviour and the sensitivity of the model to its parameters.

The loss correlation adopted by the model contains three parameters, each of which is studied independently through a parametric sweep:

1. the porosity function $G(\beta)$, chosen among the four formulations G_1–G_4 described in Section 4.5;
2. the Reynolds number function $F(Re_d)$, selected from the eight correlations listed in Table 4.1;
3. the compressibility correction $f_M(M)$, which can be enabled or disabled.

For each parameter, the remaining two parameters are held fixed at a reference configuration, and the model output is compared to the experimental total pressure profile. The agreement is quantified through the Root Mean Square Error (RMSE) computed over the measurement points at Plane 1, expressed as a fraction of the inlet total pressure P_{t0M}:

$$\text{RMSE} = \sqrt{\frac{1}{N}\sum_{k=1}^{N}\left(\frac{P_{t,k}^{\text{model}} - P_{t,k}^{\text{exp}}}{P_{t0M}}\right)^2}, \tag{4.10}$$

where N is the number of circumferential measurement points and P_{t0M} is the reference total pressure at Plane 0. The combination yielding the lowest RMSE is identified as the best-fit configuration.

Sensitivity to the porosity function

Figure 4.6 shows the circumferential profiles of P_t/P_{t0M} predicted by the four porosity functions G_1–G_4 alongside the experimental measurements for Case 7. All four formulations reproduce the qualitative shape of the total pressure distribution. The quantitative difference among the four functions is non negligible: G_1, G_3 and G_4 tending to underestimate the losses and G_2 providing the closest match to the experimental data. This is consistent with the theoretical arguments reviewed in Section 4.5, where G_2 was identified as the most widely validated porosity function in the reviewed literature [26] [4].

Sensitivity to the Reynolds number function

Figure 4.7 shows the comparison for the eight Reynolds number functions of Table 4.1, with the porosity function held fixed at G_2. The spread among the different $F(Re_d)$ correlations is visibly smaller than that observed for the porosity functions: all eight predictions fall within a narrow band close to the experimental profile, reflecting the fact that at the operating Reynolds numbers encountered, the $F(Re_d)$ functions have largely converged to their asymptotic turbulent values. Despite the reduced sensitivity, the RMSE discriminates clearly among the candidates: the Roach [28] correlation provides the best agreement with the experimental data.

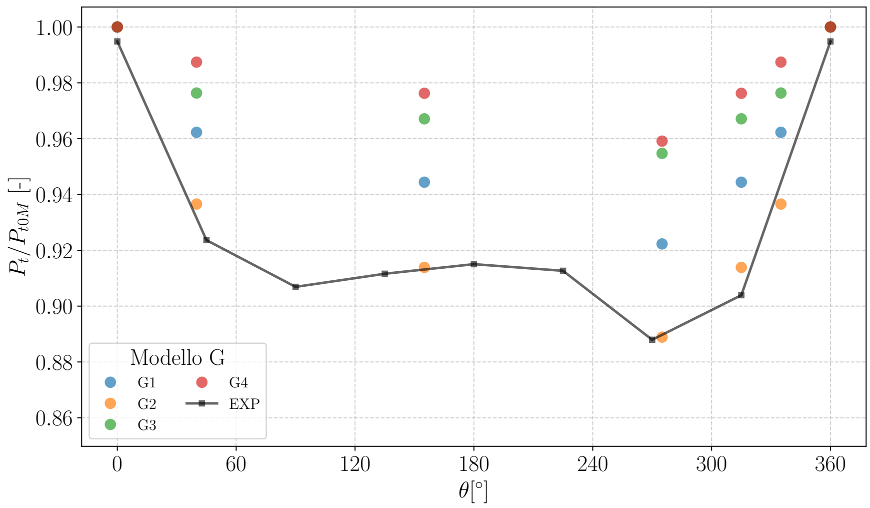

Figure 4.6: Sensitivity of the predicted P_t/P_{t0M} profile to the porosity function $G(\beta)$. Case 7 ($\dot{m}$ = 9.254 kg/s). The Reynolds function is fixed and the Mach correction is used.

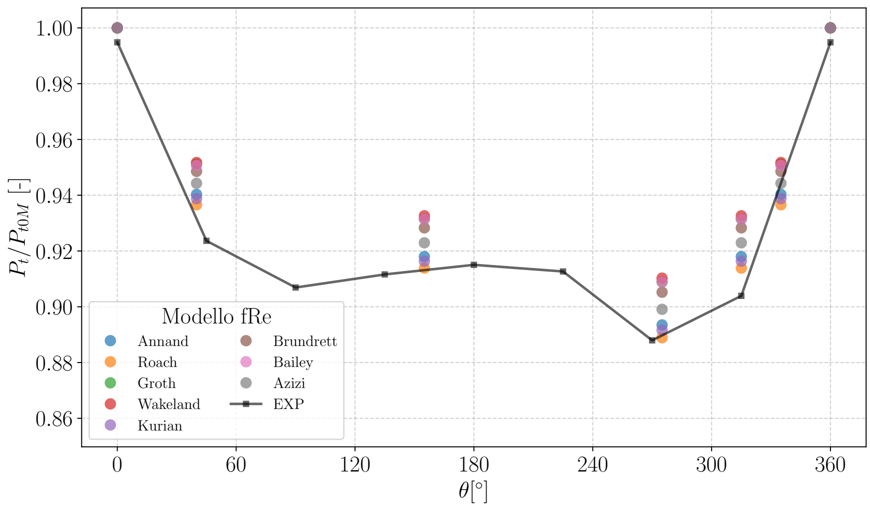

Figure 4.7: Sensitivity of the predicted P_t/P_{t0M} profile to the Reynolds number function $F(Re_d)$. Case 7 ($\dot{m}$ = 9.254 kg/s). The porosity function is held fixed at G_2 and the Mach correction is applied.

Sensitivity to the Mach number correction

Figure 4.8 compares the model predictions obtained with the Mach number compressibility correction enabled and disabled, using the best fit parameters identified above (G_2 and Roach). When the correction is active, the total pressure loss predicted in the distorted sectors is slightly reduced relative to the incompressible baseline, since the compressibility correction function $f_M(M)$ amplifies the effective resistance. The Mach correction reduces the RMSE, confirming that the compressibility correction is a necessary component of the model for the regime screen operating conditions encountered in the VKI R4 facility.

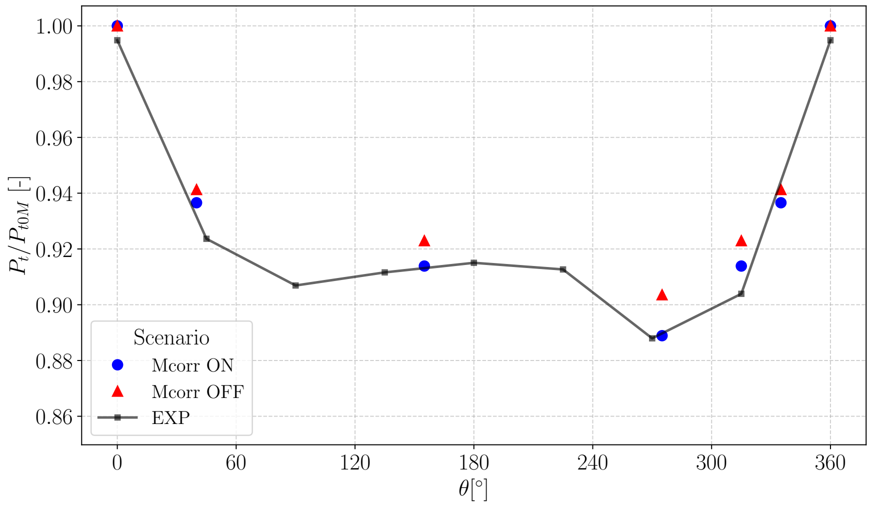

Figure 4.8: Effect of the Mach number compressibility correction on the predicted P_t/P_{t0M} profile. Case 7 ($\dot{m}$ = 9.254 kg/s). The porosity function is held fixed at G_2 and the Reynolds function at Roach.

Best-fit configuration

The parametric study identifies the combination G_2 + Roach + Mach correction as the best fit model configuration, achieving a minimum RMSE of 1.08%, calculated using the data from all seven operating conditions. This configuration is consistent across all seven operating conditions examined, confirming the robustness of the selection and ruling out overfitting to a single operating point. The detailed RMSE tables and circumferential profiles for all seven conditions are collected in Appendix A.

4.6. Iterative Solution Algorithm

Within each stream-tube, the flow is assumed isentropic on both sides of the screen. The standard compressible isentropic relations are used to relate total and static quantities through the local Mach number M:

$$P_s = P_t \left(1 + \frac{\gamma - 1}{2} M^2\right)^{-\frac{\gamma}{\gamma-1}}, \tag{4.11}$$

$$T_s = T_t \left(1 + \frac{\gamma - 1}{2} M^2\right)^{-1}, \tag{4.12}$$

$$\rho = \frac{P_s}{R T_s}, \tag{4.13}$$

$$V = M \sqrt{\gamma R T_s}. \tag{4.14}$$

The sector mass flow is computed as:

$$\dot{m}_i = \rho_i \, V_{ax,i} \, A_i = \rho_i \, V_i \cos \alpha_i \, A_i, \tag{4.15}$$

where $\alpha_i = 0$ under the zero-swirl hypothesis. The global mass flow constraint requires that the sum of sector mass flows equals the prescribed total mass flow $\dot{m}_{tot}$:

$$\sum_i \dot{m}_i = \dot{m}_{tot}. \tag{4.16}$$

The system of equations is non linear and strongly coupled: the upstream Mach number determines the local dynamic pressure and Reynolds number, which in turn determine K_c and the downstream total pressure, which itself modifies the downstream Mach number and static pressure. the residual of the antisymmetric constraint is then calculated and it feeds back to the upstream Mach number. A direct analytical solution is therefore not available, and the system is solved iteratively.

The overall algorithm is organised around a main loop that simultaneously enforces the antisymmetric static pressure condition (equation 4.3) and the global mass flow constraint (equation 4.16). The algorithm is illustrated in Figure 4.9, and the individual steps are described below.

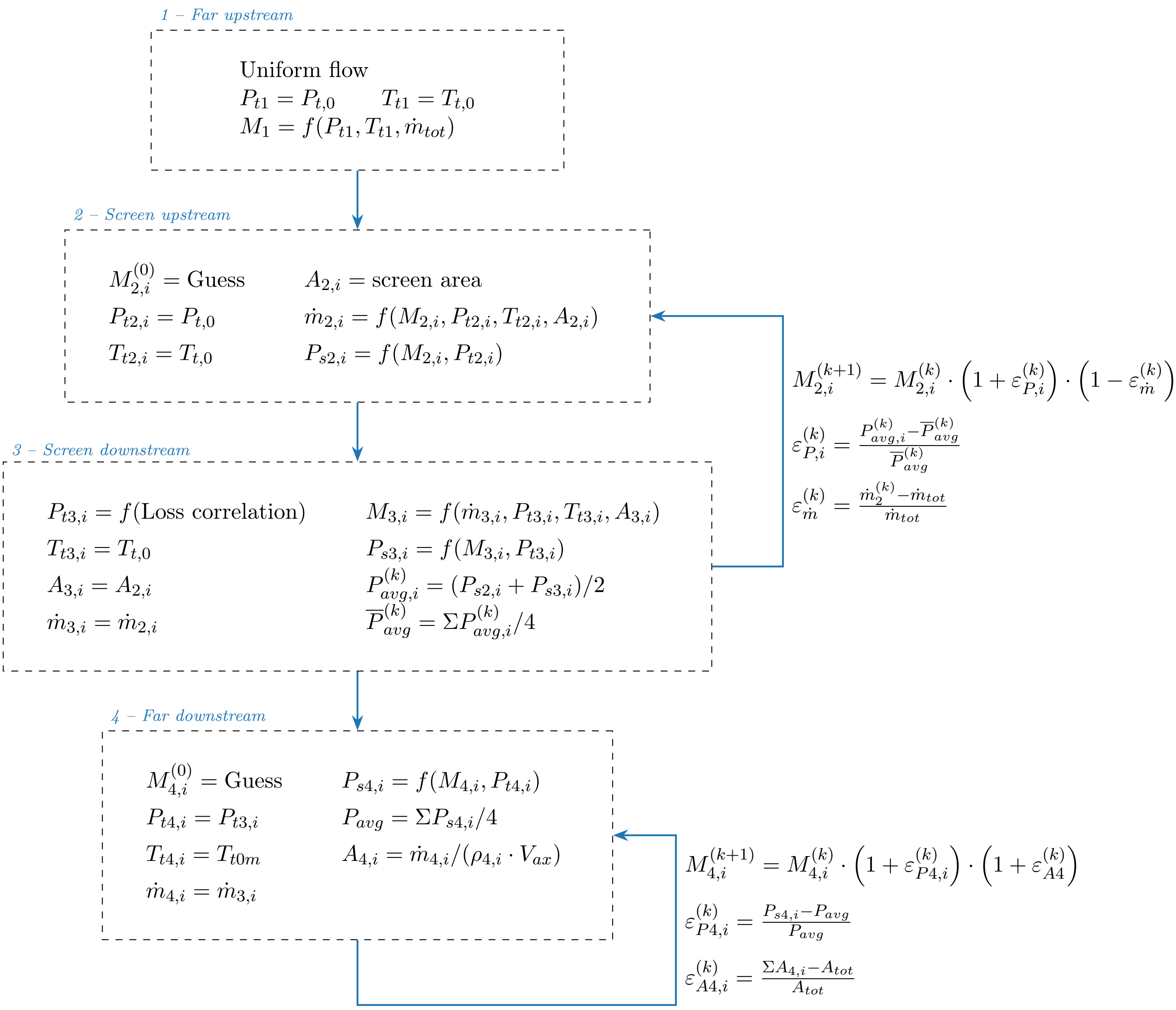

Figure 4.9: Computational flowchart of the single screen model

Main iteration loop

Initialization . All sector Mach numbers at Station 2 are initialised to a fixed uniform value $M_{2,i}^{(0)}$, equal to the uniform inlet value at Station 1.

Screen Upstream (Station 2). Given the current estimate $M_{2,i}^{(k)}$ and the known uniform values of $P_{t,0}$ and $T_{t,0}$, the isentropic relations (equations 4.11–4.14) are applied at Station 2 to compute $P_{s2,i}$, $T_{s2,i}$, $\rho_{2,i}$ and $V_{2,i}$. The sector area $A_{2,i}$ is set equal to the screen sectors areas. The sector mass flow is computed from equation 4.15, and the total mass flow $\dot{m}_2 = \sum_i \dot{m}_{2,i}$ is evaluated.

Screen loss coefficients. The wire-diameter Reynolds number $\mathrm{Re}_{d_w,i}$ is computed from equation 4.7. The three correction factors $G(\beta_i)$, $f_{Re,i}$ and $f_{Ma,i}$ are then evaluated from the corresponding correlations, and the loss coefficient $K_{c,i}$ is assembled from equation 4.5. The choking Mach number M_i^* is also checked against the current $M_{2,i}$.

Screen Downstream (Station 3). The total pressure at Station 3 is computed from the pressure drop relation (equation 4.6). The sector area $A_{2,i}$ is set equal to the screen sectors areas. The total temperature is conserved from Station 2. The sector mass flow at Station 3 is set equal to that at Station 2, consistently with the mass conservation hypothesis. The Mach number at Station 3 is recovered by inverting the isentropic mass flow function:

$$\dot{m}_{3,i} = \frac{P_{t,3,i}}{\sqrt{T_{t,3,i}}} \cdot A_{3,i} \cdot \frac{\sqrt{\gamma/R}\, M_{3,i}}{\left(1 + \frac{\gamma-1}{2} M_{3,i}^2\right)^{\frac{\gamma+1}{2(\gamma-1)}}}. \tag{4.17}$$

The static pressure $P_{s,3,i}$ is then obtained from equation 4.11.

Residual evaluation and Mach number update. The sector-averaged static pressure $P_{avg,i} = (P_{s,2,i} + P_{s,3,i})/2$ is computed for each sector, and its circumferential average $\overline{P}_{avg}$ is obtained. The relative residual of the antisymmetric constraint for each sector is:

$$\varepsilon_{P,i}^{(k)} = \frac{P_{avg,i}^{(k)} - \overline{P}_{avg}^{(k)}}{P_{avg,i}^{(k)}}. \tag{4.18}$$

The relative residual of the global mass flow constraint is:

$$\varepsilon_{\dot{m}}^{(k)} = \frac{\dot{m}_2^{(k)} - \dot{m}_{tot}}{\dot{m}_2^{(k)}}. \tag{4.19}$$

The sector Mach numbers are updated simultaneously using a proportional correction:

$$M_{2,i}^{(k+1)} = M_{2,i}^{(k)} \cdot \left(1 + \varepsilon_{P,i}^{(k)}\right) \cdot \left(1 - \varepsilon_{\dot{m}}^{(k)}\right). \tag{4.20}$$

It is relevant to notice how $\varepsilon_{P,i}^{(k)}$ has a different value for each sector, while $\varepsilon_{\dot{m}}^{(k)}$ is the same value for all sectors. The physical motivation for these correction is as follows. A sector whose local averaged static pressure exceeds the circumferential mean is one where the flow resistance is too low relative to the average; increasing its Mach number raises the screen loss, driving the averaged pressure back towards uniformity. If the total mass flow exceeds $\dot{m}_{tot}$, all sector Mach numbers are reduced proportionally.

Convergence criteria The iterative loop is declared converged when both of the following conditions are satisfied simultaneously:

$$\sum_i \left|\varepsilon_{P,i}^{(k)}\right| < 10^{-7}, \quad \left|\varepsilon_{\dot{m}}^{(k)}\right| < 10^{-7}. \tag{4.21}$$

The loop is limited to a maximum of 300 iterations; if convergence is not achieved within this bound, a warning is printed together with the residual values and the iteration count.

Far-upstream (Station 1)

Once the main loop has converged, the far-upstream flow state at Station 1 is determined by a direct calculation. No iterative loop is needed since the flow is uniform. From the known values of $\dot{m}_{tot}$, $P_{t,0}$, $T_{t,0}$, all the other quantities can be calculated.

From the iterative loop in stations 2 and 3, the mass flow passing through each screen sector is known. From the values of $\dot{m}_{1,i} = \dot{m}_{2,i}$, the areas of the stream-tubes at station 1 can be obtained. The sector area at Station 1 follows from the mass flow:

$$A_{1,i} = \frac{\dot{m}_{1,i}}{\rho_{1,i}\, V_{ax,1,i}}, \tag{4.22}$$

Far-downstream (Station 4)

The far-downstream flow state at Station 4 is computed by a second iterative loop. The total pressure at Station 4 are set equal to the converged values at Station 3. The Mach numbers are adjusted iteratively to enforce:

1. circumferentially uniform static pressure at Station 4 ($\varepsilon_{P4,i} < 10^{-7}$);

2. the sum of the sector areas at Station 4 equal to the total duct area S ($\varepsilon_{A4} < 10^{-7}$).

4.7. Model Outputs and Physical Interpretation

The iterative solution of the analytical model yields the complete thermodynamic and kinematic state of the flow along the four axial stations. The evolution of the stream-tube area, Mach number, static pressure, and total pressure for a representative operating point is presented in Figure 4.10.

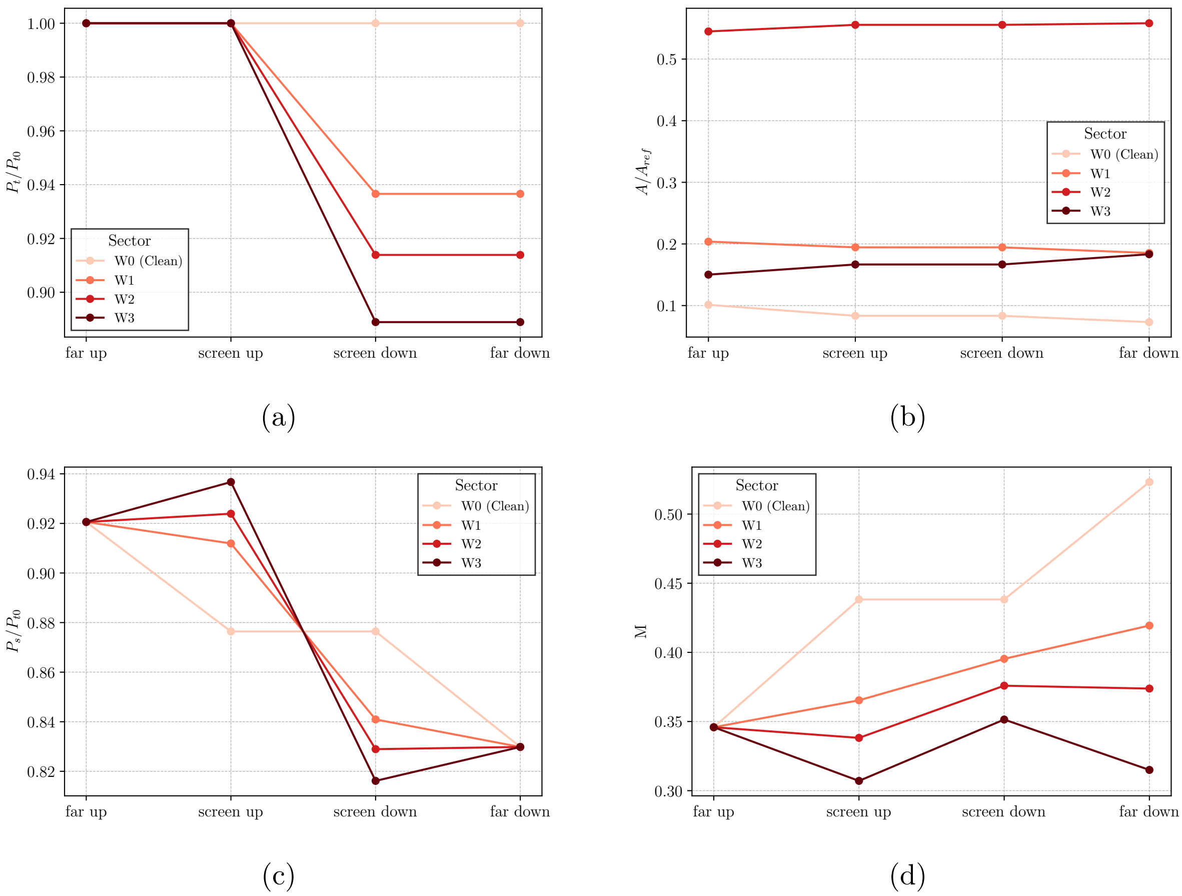

Figure 4.10: Evolution of stream-tube properties across the four axial stations for the different screen sectors: (a) total pressure, (b) cross section area, (c) static pressure, and (d) Mach number. Total and static pressure are made adimensional with the inlet total pressure.

The physical mechanisms driving the flow redistribution can be interpreted by analysing the four parameters:

Total Pressure As imposed by the model hypotheses, the flow is isentropic everywhere except across the screen. Consequently, the total pressure (Figure 4.10a) remains circumferentially uniform and constant between the far upstream station and the screen upstream face (Stations 1 to 2). Across the screen (Stations 2 to 3), the total pressure drops in accordance with the local loss coefficient $K_{c,i}$ of each mesh sector. The finest mesh (W3) exhibits the highest total pressure drop, while the clean sector (W0) experiences no loss, preserving $P_{t,3,W0} = P_{t,0}$. The total pressure is then conserved again in the downstream duct (Stations 3 to 4).

stream-tube Area To satisfy mass conservation under varying density and velocity conditions, the effective area of each stream-tube adjusts dynamically (Figure 4.10b). Since the geometric boundaries of the sectors are strictly fixed at the screen faces (Stations 2 and 3), the area is constant across the interface. However, in the unconstrained domains upstream and downstream, the stream-tubes expand or contract. For instance, the highly restricted flow approaching the W3 sector requires a larger capture area upstream to balance the strong local deceleration. Conversely, the high-velocity stream-tube passing through the clean sector (W0) contracts relative to its screen-plane geometric area.

Static Pressure The static pressure field (Figure 4.10c) acts as the primary mechanism for mass flow redistribution. Starting from a uniform state far upstream, the presence of the screen generates an upstream blockage effect. To force the flow through the varying resistances, the static pressure must rise upstream of the denser meshes (W3 and W2) and decrease upstream of the clean sector (W0). This lateral pressure gradient deflects the flow toward the path of least resistance (W0).

Across the screen, the static pressure changes drastically, bounded by the antisymmetric condition enforced by the model. Because sector W0 has no physical screen, its local loss is zero; with constant area and constant total pressure across the interface, its static pressure remains perfectly flat from Station 2 to Station 3. Far downstream (Station 4), the model correctly enforces the full mixing of the fluid, resulting in the re equalization of the static pressure across all circumferential sectors.

Mach Number The Mach number (Figure 4.10d) responds directly to the static and total pressure variations. In the upstream region (Stations 1 to 2), where total pressure is uniform, the Mach number mirrors the static pressure behaviour: the flow decelerates significantly in front of the dense W3 sector and accelerates towards the clean W0 sector.

Downstream of the screen, as the static pressure equalizes toward Station 4, the persistent total pressure deficit dictates the final velocity field. Consequently, W3 features the lowest far-downstream Mach number, while the clean sector W0 accelerates to the highest Mach number value to conserve the overall mass flow.

4.8. CFD Results and Model Comparison

The converged CFD solution for the single-screen configuration is analysed by examining the total pressure field, the static pressure field, and the Mach number field. The analytical model is then compared quantitatively with the CFD solution by extracting axial profiles of each quantity at the circumferential midpoint of each of the four circumferential sectors, at the axial stations indicated by the dashed lines in the colourmap figures. The extraction lines are located at the Y-coordinate corresponding to the centre of each sector, away from the boundaries between adjacent sectors. This choice is taken because the one-dimensional stream-tube model does not include the inter-sector boundary regions, where the two-dimensional shear layers and lateral pressure gradients produce a flow structure that the model cannot represent. Comparing the model against midpoint values rather than sector-averaged values therefore provides the most physically meaningful assessment of the model's predictive capability within its own domain of validity.

The four comparison points per sector correspond to the four axial stations of the model: far upstream, screen upstream, screen downstream, and far downstream. The axial positions for the model points close to the screen have been chosen to match the peaks in static pressure of the CFD for the screen upstream and downstream points. The far upstream and downstream positions have been chosen at axial coordinates where the static pressure distortion has been fully recovered. This is a necessary assumption, since the model does not predict the axial position of the axial stations.

4.8.1. Total Pressure

The total pressure field is the most immediate indicator of the loss distribution imposed by the screen on the flow, and its comparison is presented first, as it establishes the correspondence between the loss correlations used in the model and the CFD. Total pressure is a conserved quantity in isentropic flow and is altered only by the irreversible losses introduced by the wire mesh screen. The sector-dependent total pressure drop across the screen is therefore the primary output of the loss model, governed by the screen resistance correlations: if the model fails to reproduce the correct total pressure levels at the screen downstream station, it becomes harder to isolate discrepancies due to the flow redistribution mechanism alone, since part of the discrepancy would be caused by a mismatch in the total pressure level itself.

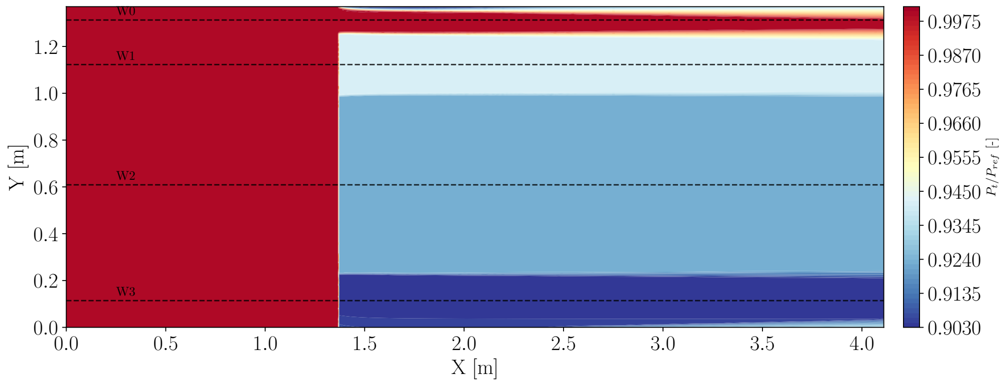

Figure 4.11: CFD results for the single-screen configuration: normalised total pressure field P_t/P_{ref} over the full two-dimensional domain. Dashed horizontal lines delimit the four circumferential sectors W0–W3; dashed vertical lines indicate the axial stations at which the profiles of Figure 4.12 are extracted. The screen plane is located at $X = 1.37$ m.

The normalised total pressure colourmap is shown in Figure 4.11. Upstream of the screen, the total pressure is uniform across the entire domain at $P_t/P_{\text{ref}} \approx 1$, confirming the homogeneous inlet boundary condition and the absence of upstream losses. Immediately downstream of the screen, the total pressure drops sharply in each sector by an amount directly proportional to the local wire mesh resistance: sector W0, where no losses are imposed, retains a total pressure ratio close to unity, while sectors W1, W2, and W3 exhibit progressively larger losses, with W3 showing the most severe deficit. The resulting stratification is maintained throughout the entire downstream domain with only marginal attenuation, as turbulent diffusion across the shear layers at the sector boundaries is slow relative to the axial velocity.

The corresponding axial profiles, extracted at the stations marked in Figure 4.11, are shown in Figure 4.12. Upstream of the screen, all four sectors share a uniform total pressure of unity, and both CFD and model correctly agree at this station. At the screen downstream station, the model predictions are in good agreement with the CFD midpoint extractions at all four sectors, correctly reproducing the sector-dependent loss pattern described above. In the far downstream region, both CFD and model confirm that this stratification persists with negligible attenuation, as expected in the absence of significant inter-sector mixing. This agreement validates that the correlation set in the CFD porous jump boundary condition matches the one used by the model. Having established this correspondence, it is now physically meaningful to examine how the flow redistributes circumferentially in response to the non-uniform loss pattern.

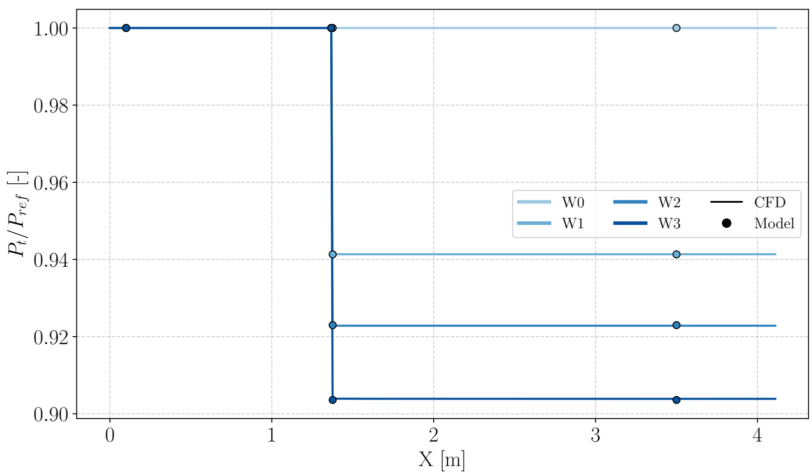

Figure 4.12: Axial profiles of normalised total pressure P_t/P_{ref} extracted at the midpoint of each sector for the single-screen configuration. Solid lines denote CFD extractions; filled symbols denote model predictions at the four axial stations.

4.8.2. Static Pressure

The static pressure field reveals the mechanism by which the non-uniform screen interacts with the flow *upstream* of the screen plane, driving the circumferential mass flow redistribution.

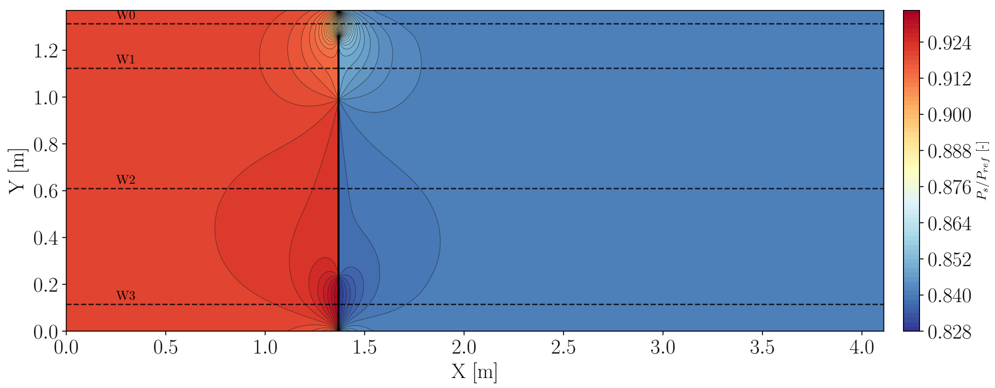

Figure 4.13: CFD results for the single-screen configuration: normalised static pressure field P_s/P_{ref} over the full two-dimensional domain. Dashed horizontal lines delimit the four circumferential sectors W0–W3; dashed vertical lines indicate the axial stations at which the profiles of Figure 4.14 are extracted. The screen plane is located at $X = 1.37$ m.

The normalised static pressure colourmap is shown in Figure 4.13. Far upstream, the static pressure is entirely uniform across all sectors, as expected from the prescribed inlet conditions, confirming that the domain inlet is sufficiently far upstream of the screen and that the full redistribution process is captured by the simulation. As the flow approaches the screen, the contours diverge between sectors due to the potential upstream influence of the screen's resistance distribution: sectors W2 and W3, where the highest losses occur, develop an elevated upstream static pressure acting as a distributed back pressure on the approaching flow, while the low-resistance sector W0 is characterised by a relatively lower upstream static pressure. This circumferential static pressure gradient is the driving force of the lateral mass flow redistribution, deflecting streamlines away from the high-resistance sectors and towards the low-resistance ones before the flow reaches the screen plane. Immediately downstream of the screen, the static pressure field exhibits sharp circumferential distortion, and then gradually relaxes towards a circumferentially uniform level as the flow progresses downstream, recovering full azimuthal uniformity at the far-downstream plane.

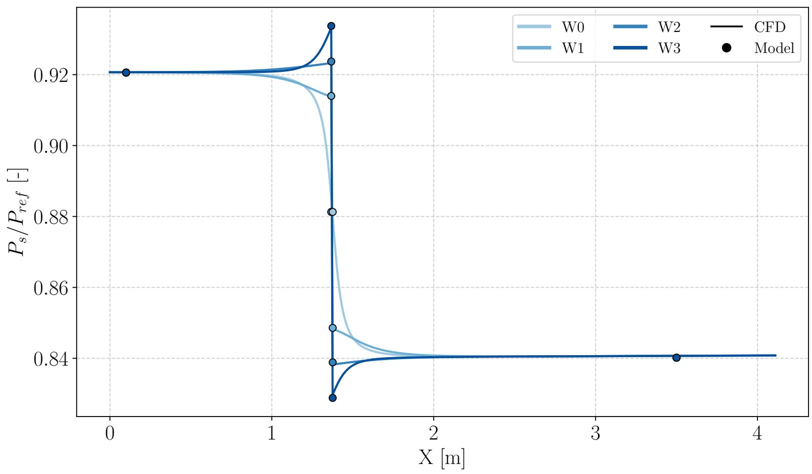

Figure 4.14: Axial profiles of normalised static pressure P_s/P_{ref} extracted at the midpoint of each sector for the single-screen configuration. Solid lines denote CFD extractions; filled symbols denote model predictions at the four axial stations.

The corresponding axial profiles, extracted at the stations marked in Figure 4.13, are shown in Figure 4.14. The CFD profiles reproduce the behaviour described above: upstream uniformity giving way to a sector-dependent divergence approaching the screen, a sharp non-uniform distribution immediately downstream, and full azimuthal recovery in the far downstream region. The model predictions are in good agreement with the CFD midpoint values at all stations, correctly capturing the upstream back-pressure imbalance between sectors and the sharp sector-to-sector contrast immediately behind the screen. This confirms that the static pressure assumption in the model correctly captures the static pressure imbalance caused by the distortion screen.

4.8.3. Mach Number

The Mach number field is a direct consequence of the total pressure and static pressure distributions described above: for a given local total pressure, the Mach number is uniquely determined by the local static pressure through the isentropic relation, and its circumferential distortion is therefore fully determined by the two quantities already validated.

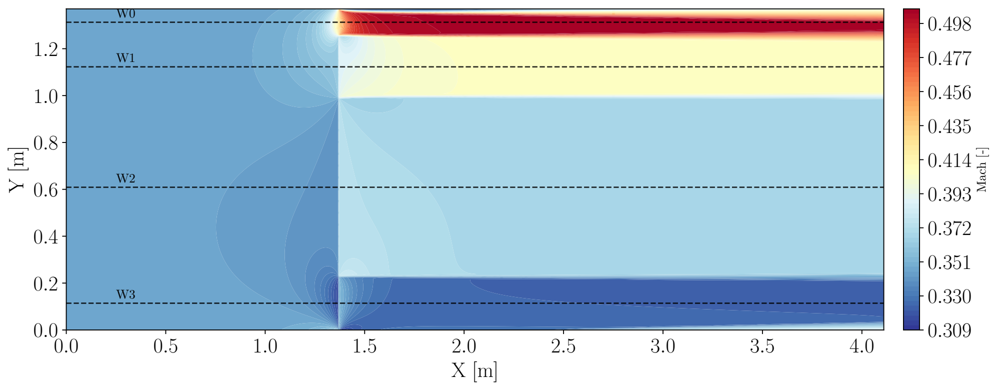

Figure 4.15: CFD results for the single-screen configuration: Mach number field over the full two-dimensional domain. Dashed horizontal lines delimit the four circumferential sectors W0–W3; dashed vertical lines indicate the axial stations at which the profiles of Figure 4.16 are extracted. The screen plane is located at $X = 1.37$ m.

The Mach number colourmap is shown in Figure 4.15. Far upstream, the flow is entirely uniform at $M = 0.346$, consistent with the prescribed mass flow operating point. As the flow approaches the screen, the circumferential static pressure gradient established by the upstream potential effect induces a lateral redistribution of velocity: sector W0 accelerates due to its lower back pressure, while sectors W2 and W3 decelerate. The Mach number distortion between sectors reaches its maximum at the screen plane itself, where sector W0 reaches Mach numbers well above $M = 0.5$ immediately downstream of the screen, while sector W3 shows a pronounced deficit, the combined result of its higher total pressure loss and the static pressure drop due to the coupling with the adjacent sectors. Downstream of the screen, the Mach number distortion persists and only partially attenuates through the shear layers forming at the sector boundaries. After $X \approx 1.9$ m, where the static pressure has equalised, the residual Mach number distortion corresponds directly to the total pressure stratification established at the screen plane.

The corresponding axial profiles, extracted at the stations marked in Figure 4.15, are shown in Figure 4.16. At the far upstream station, the model correctly reproduces the

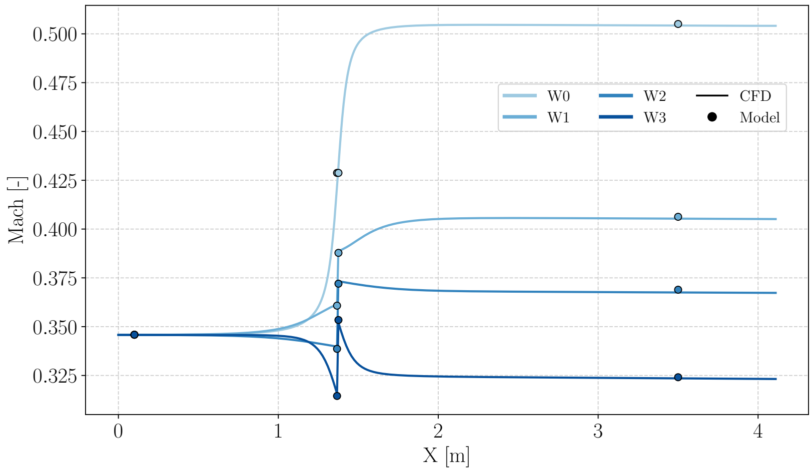

Figure 4.16: Axial profiles of Mach number extracted at the midpoint of each sector for the single-screen configuration. Solid lines denote CFD extractions; filled symbols denote model predictions at the four axial stations.

uniform Mach number of $M = 0.346$ shared by all sectors. Approaching the screen, the model correctly predicts the upstream velocity redistribution driven by the circumferential static pressure gradient: the deceleration of the high-loss sectors and the acceleration of W0. At the screen downstream station, the strong sector-to-sector contrast is captured with reasonable accuracy: the model predicts a sharp velocity excess in W0 and a corresponding deficit in W3, both in good agreement with the CFD midpoint extractions. In the far downstream region, both model and CFD approach distinct asymptotic Mach numbers for each sector, consistent with the non-uniform total pressure stratification persisting beyond the point of static pressure equalisation.

4.8.4. Quantitative Error Analysis

The agreement between the analytical model and the CFD solution is assessed quantitatively through three scalar metrics. The pointwise signed percentage error at each station s and sector i is defined as:

$$\varepsilon_{s,i} = \frac{\phi_{s,i}^{\text{model}} - \phi_{s,i}^{\text{CFD}}}{\phi_{s,i}^{\text{CFD}}} \times 100, \tag{4.23}$$

where ϕ denotes the quantity of interest. The Mean Absolute Relative Error (MARE) and the Root Mean Square Relative Error (RMSRE) are then computed over all N_S station and N_i sectors as:

$$\mathrm{MARE} = \frac{1}{N_s N_i} \sum_{s,i} |\varepsilon_{s,i}|\,, \qquad \mathrm{RMSRE} = \sqrt{\frac{1}{N_S N_i} \sum_{s,i} \varepsilon_{s,i}^2}. \tag{4.24}$$

The MARE quantifies the average magnitude of the deviation, while the RMSRE penalises large outliers more heavily and therefore provides a more sensitive indicator of worst-case disagreement.

The pointwise errors for static pressure, Mach number, and total pressure are reported in Tables 4.2–4.4.

Station	**W0 [%]**	**W1 [%]**	**W2 [%]**	**W3 [%]**
Far Upstream	−0.01	−0.01	−0.01	−0.01
Screen Upstream	−0.39	+0.02	+0.05	+0.05
Screen Downstream	+0.19	+0.04	+0.07	−0.11
Far Downstream	−0.06	−0.06	−0.06	−0.06

Table 4.2: Signed percentage error $\varepsilon_{s,i}$ of normalized static pressure P_s/P_{ref}. MARE = 0.08%, **RMSRE = 0.12%**.

Station	**W0 [%]**	**W1 [%]**	**W2 [%]**	**W3 [%]**
Far Upstream	+0.02	+0.01	+0.03	+0.02
Screen Upstream	+1.60	−0.15	−0.34	−0.40
Screen Downstream	−0.79	−0.23	−0.33	+0.39
Far Downstream	+0.15	+0.23	+0.39	+0.17

Table 4.3: Signed percentage error $\varepsilon_{s,i}$ of Mach number. MARE = 0.33%, **RMSRE = 0.50%**.

Station	**W0 [%]**	**W1 [%]**	**W2 [%]**	**W3 [%]**
Far Upstream	+0.00	−0.00	+0.00	+0.00
Screen Upstream	+0.00	+0.00	+0.00	+0.00
Screen Downstream	+0.00	−0.00	+0.02	−0.04
Far Downstream	+0.00	−0.00	+0.02	−0.03

Table 4.4: Signed percentage error $\varepsilon_{s,i}$ of normalized total pressure P_t/P_{ref}. MARE = 0.01%, **RMSRE = 0.01%**.

The error metrics confirm the overall agreement between the model and the CFD solution across all three quantities. The total pressure errors are small at every station and sector (MARE = 0.01%), which is consistent with the fact that the loss correlations used in the porous jump boundary condition and in the model are identical by construction. The static pressure errors are also small (MARE = 0.08%), with the largest deviation of −0.39% occurring at the screen upstream station of sector W0. The Mach number errors are the largest of the three (MARE = 0.33%, RMSRE = 0.50%), with the peak error of +1.60% again localised at the screen upstream station of sector W0. All remaining points exhibit errors well below 0.5%, confirming that the one dimensional stream-tube model captures the dominant physics of the circumferential redistribution with high fidelity.

The biggest absolute error values is found in the clean sector W0, in the two station upstream and downstream the screen. Since the sector has no total pressure loss, the model predicts no static pressure or Mach number variation between these two stations, but the far upstream and far downstream values of the two quantities show that the static pressure and Mach are respectively decreasing and increasing across the screen. The discrepancy lies in the fact that the CFD outputs a smooth decreasing or decreasing trend, while the model does it with a discreet approach. As a result, the model assigns to the W0 stations adjacent to the screen the values that correspond to the screen interface conditions in the CFD solution, rather than the local values immediately upstream and downstream of the screen that a continuous representation would predict.

4.9. Model vs Experimental Data

The model predictions are compared here against the experimental measurements acquired at Plane 1, downstream of the distortion screen. The experimental setup and the distortion screen geometry are described in detail in Chapter 3.

As shown in Figure 3.2b, the physical distortion screen installed in the VKI R4 facility is subdivided into six circumferential sectors of non-equal angular extent, assembled from four distinct wire mesh configurations: W0 (clean, no mesh), W1, W2, and W3. Configurations W1, W2 each appear in two separate, not adjacent angular locations around the annulus, while W0 and W3 occupy only one sector each. The resulting circumferential pattern is therefore more complex than a simple four sector arrangement, exhibiting two separate occurrences of some mesh types.

The analytical model, by contrast, discretises the annulus into exactly four stream-tubes, one per distinct mesh type, and splitting some of the sectors would output the same result, since the model has no information about sectors adjacency. Each model stream-tube is assigned an angular extent equal to the total combined angular width of all physical screen sectors sharing the same wire mesh configuration. This condensation is consistent with the model: since each stream-tube is characterised solely by its loss coefficient and total cross-sectional area, the two separate W1 sectors are aerodynamically equivalent to a single sector of the same total width. Splitting a sector would give the same model output as if they were combined, since the model has no information about sectors' adjacency.

As a consequence, the model produces a single scalar prediction for each aerodynamic quantity (total pressure, static pressure, Mach number, yaw angle) per mesh type. When comparing against the experimental data, each model point is therefore plotted at the circumferential midpoint of its corresponding physical screen sector. Since W1 and W2 each appear twice, the same model prediction is shown at two distinct angular positions, reflecting the symmetry of the condensed representation.

Comparison at Plane 1

Figure 4.17 shows the circumferential distributions of P_t/P_{t0M}, P_s/P_{t0M}, Mach number M, and yaw angle at Plane 1, comparing the experimental traverse against the two model axial stations that bracket the measurement location: $\text{MODEL}_{\text{down}}$ (Station 3, immediately downstream of the screen) and $\text{MODEL}_{\text{fardown}}$ (Station 4, far downstream where static pressure is circumferentially uniform).

The total pressure distribution is well reproduced by both model stations, with a RMSRE of 0.82%. Since total pressure is conserved between Station 3 and Station 4 within each stream-tube and is entirely governed by the screen loss correlations. The two sets of model points therefore coincide for P_t, and the agreement with experimental data has been discussed in Section 4.5.1

The most significant difference between the two model stations appears in the static pressure and in the Mach number. At Station 3, immediately downstream of the screen, the static pressure retains a strong circumferential non-uniformity, consistent with the anti-symmetric pressure condition described in Section 4.2. At Station 4, the static pressure has equalised to a common circumferential level by construction, leading to higher Mach numbers in the clean sector W0 and lower values in the distorted sectors. The experimental static pressure distribution at Plane 1 lies between these two limiting states: it is neither as non-uniform as Station 3 nor as uniform as Station 4, suggesting that the physical measurement plane is located at an intermediate axial position within the pressure relaxation region between the screen and the far downstream equilibrium.

This observation motivates an axial interpolation between the two model stations. Since

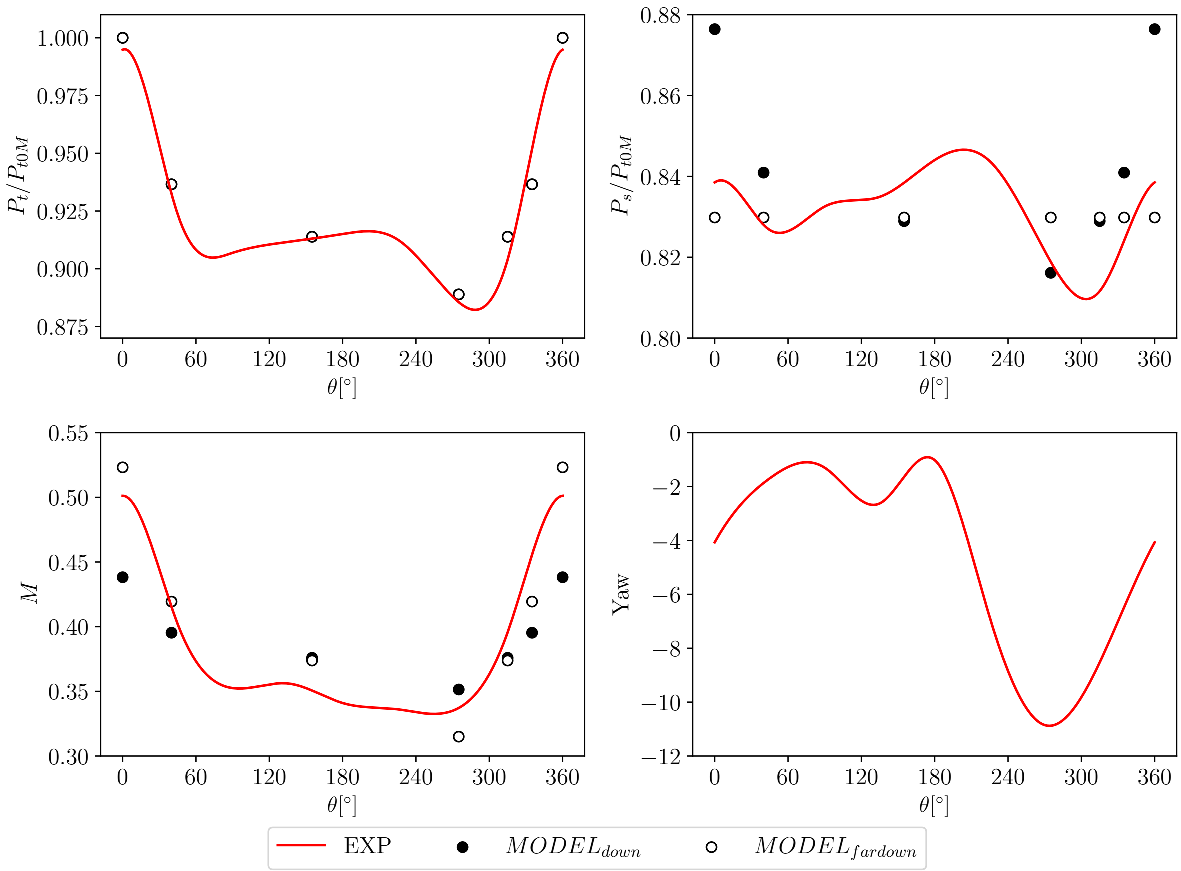

Figure 4.17: Circumferential distributions of P_t/P_{t0M}, P_s/P_{t0M}, M, and yaw angle at Plane 1. Red solid line: experimental data; filled circles: $\text{MODEL}_{\text{down}}$ (Station 3, screen downstream); open circles: $\text{MODEL}_{\text{fardown}}$ (Station 4, far downstream).

the exact position of Plane 1 relative to the screen is known (the screen is installed one IGV axial chord upstream of the IGV, at a normalised axial distance $\Delta X_{\text{norm}} = 0.206$, as described in Chapter 3), a linear interpolation at 70% of the distance between Station 3 and Station 4 is performed. The result, denoted $\text{MODEL}_{70\%}$, is shown in Figure 4.18.

The interpolated predictions show a markedly improved agreement with the experimental data for both static pressure and Mach number, with RMSRE respectively of 1.14% and 5.01% .This confirms that the 70% interpolation point provides a reasonable approximation of the physical axial location of Plane 1.

Two sources of residual discrepancy deserve attention. First, the experimental static pressure distribution is not fully uniform at Plane 1, exhibiting a residual circumferential variation that the far-downstream model station cannot reproduce by construction. This

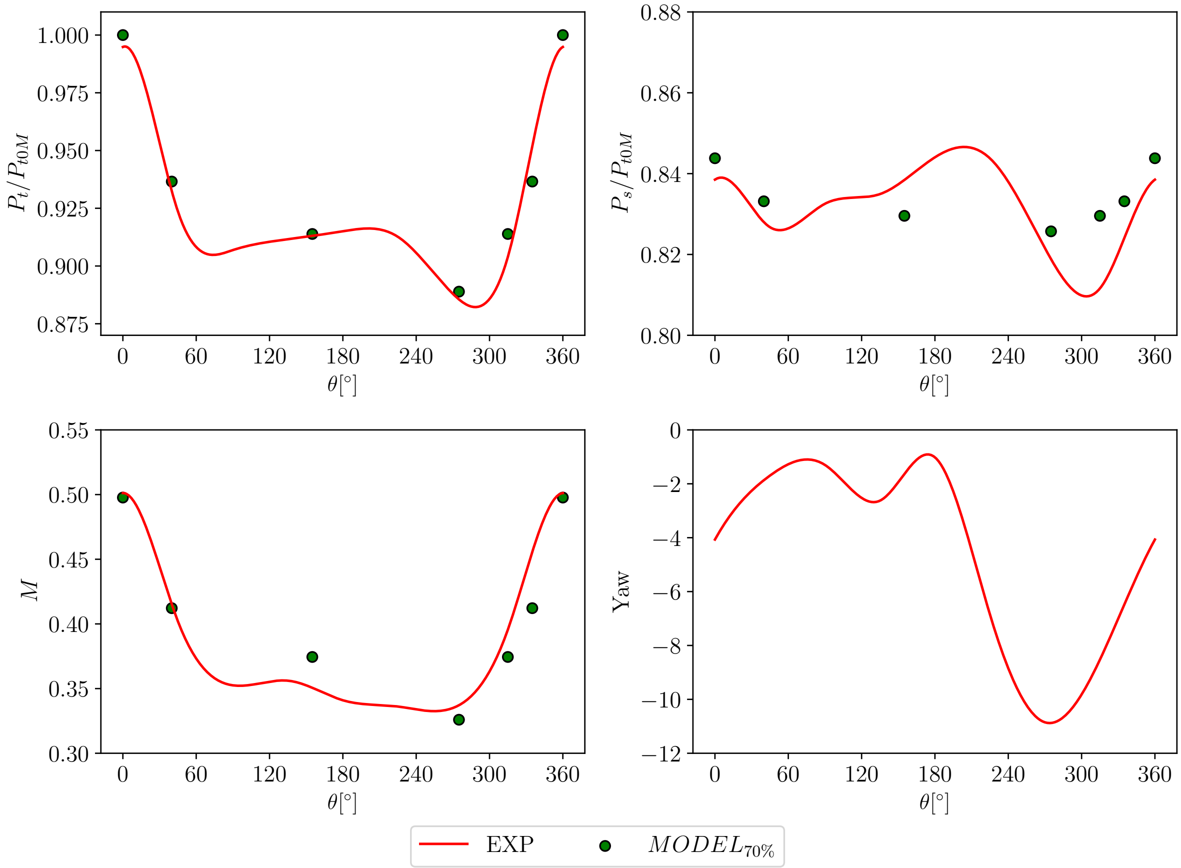

Figure 4.18: Circumferential distributions of P_t/P_{t0M}, P_s/P_{t0M}, M, and yaw angle at Plane 1. Red solid line: experimental data; green filled circles: $\mathrm{MODEL}_{70\%}$.

non-uniformity has a dual origin: on one hand, the axial gap between the screen and Plane 1 may be insufficient for the pressure field to reach full circumferential equilibrium, so that the distortion imposed by the screen is still partially active at the measurement location; on the other hand, the compressor itself, operating at non-uniform mass flow conditions imposed by the distortion, induces a circumferentially varying back-pressure on the incoming flow, which modifies the local static pressure distribution upstream of the IGV.

Second, the model assumes zero swirl angle at all stations (hypothesis 8 in Section 4.2), whereas the experimental data reveal a non negligible yaw component throughout the annulus, as shown in Figures 4.17 and 4.18. The presence of swirl carries additional kinetic energy in the circumferential direction, which modifies both the static pressure and the Mach number distributions.

5 | Dual Screen Model

This chapter extends the single screen model developed in Chapter 4 to the case of two screens placed in series within the same annular duct. Two distinct modelling strategies are proposed, differing in how the antisymmetric static pressure assumption is implemented in the two screen configuration: the *Coupled* model (Section 5.2) and the *Decoupled* model (Section 5.3). The two formulations are physically different: the Coupled model assumes that the two screens are close enough for their pressure fields to interact directly, while the decoupled model assumes that the flow has enough distance between the two screens to re-equalize its static pressure completely before encountering the second screen. The two models represents two limits in terms of the distance between the two screens. In order to best models the intermediate screen distance cases, the *Hybrid* model has been developed, which is an interpolation of the two models, as a function of the normalised axial screen distance.

5.1. Circumferential Discretisation

The annular domain is discretised into a set of circumferential stream-tubes, each defined by its angular extent $\Delta\theta_i$. Because Screen 1 and Screen 2 may in general have different sector boundaries, the combined discretisation is obtained by taking the union of all sector boundaries of both screens. If Screen 1 has boundaries $\{\theta_j^{(1)}\}$ and Screen 2 has boundaries $\{\theta_k^{(2)}\}$, the resulting set of combined boundaries is:

$$\Theta = \{0°\} \cup \{\theta_j^{(1)}\} \cup \{\theta_k^{(2)}\} \cup \{360°\}, \tag{5.1}$$

The values are then ordered in ascending order, then each interval $[\Theta_n, \Theta_{n+1}]$ defines a stream-tube. This procedure guarantees that all relevant circumferential transitions of both screens are captured simultaneously within a single unified grid, regardless of whether the two screens share the same sector boundaries. The ultimate goal of this

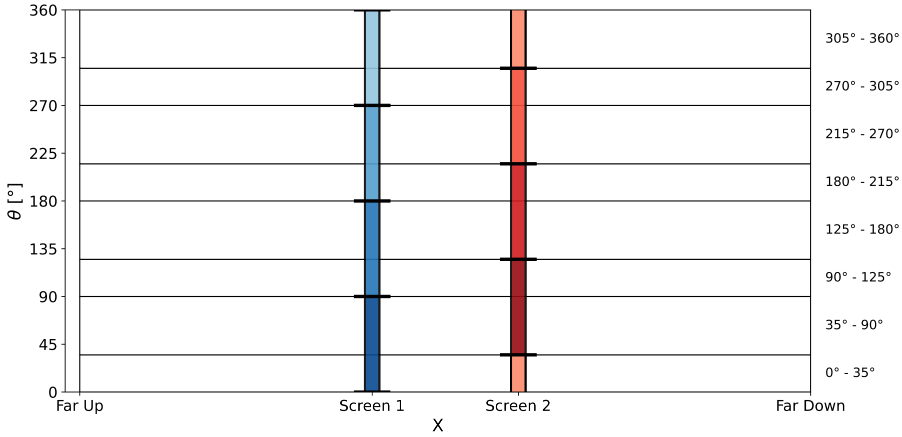

Figure 5.1: Schematic of the geometrical discretization and stream-tubes in the annular domain. Screen 1 and Screen 2 are divided into distinct sectors (coloured in blue and red gradients to indicate varying porosity). The horizontal white bands represent the independent 1D stream-tubes extracted from the overlapping screen boundaries, extending along the axial direction.

procedure is to ensure that each stream-tube goes through a uniform portion of each screen. The area of each composite stream-tube at the screen planes is:

$$A_i = \frac{\Delta\theta_i}{360^\circ} \cdot S, \tag{5.2}$$

where S is the total annular cross sectional area. This discretisation is adopted by both the Coupled and Decoupled models described in the sections that follow.

Figure 5.1 shows an example of discretization for two arbitrary screen geometries. Each screen sector boundary creates a new stream-tube boundary, so that each stream-tube only goes through uniform sections of the two distortion screens.

5.2. Coupled Model

5.2.1. Axial Stations and Physical hypotheses

Five axial stations are defined for the Coupled model, as illustrated schematically in Figure 5.2:

- **Station 1 – Far upstream**: sufficiently far upstream of Screen 1 for the static pressure to be circumferentially uniform. The inlet total pressure $P_{t,1,i} = P_{t,0}$ and total temperature $T_{t,1,i} = T_{t,0}$ are uniform across all sectors.

- **Station 2 – Screen 1 upstream**: located immediately upstream of Screen 1. This is the station where the loss correlations for Screen 1 are evaluated, since the local Mach number, Reynolds number and dynamic pressure involved in the calculation of the loss coefficient are those of the inlet flow. The total pressure is still undisturbed $P_{t,1,i} = P_{t,0}$.
- **Station 3 – Inter screen plane**: located immediately downstream of Screen 1 and immediately upstream of Screen 2. The total pressure at this station is reduced relative to Station 2 by the local Screen 1 loss coefficient $K_{c1,i}$. This is the station where the loss correlations for Screen 2 are evaluated.
- **Station 4 – Screen 2 downstream**: located immediately downstream of Screen 2. The total pressure is further reduced relative to Station 3 by the Screen 2 loss coefficient $K_{c2,i}$.
- **Station 5 – Far downstream**: sufficiently far downstream of Screen 2 for the static pressure to equalize circumferentially. The total pressure at this station equals that of Station 4 for each sector, since the downstream flow is assumed isentropic.

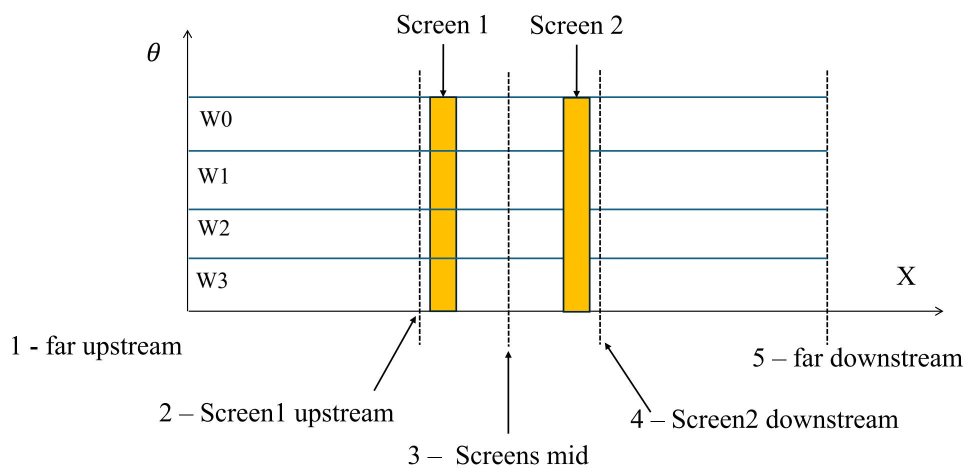

Figure 5.2: Schematic of the Coupled dual screen model showing the five axial stations. θ: circumferential direction. X: Axial direction.

The Coupled model retains all the physical hypotheses of the single screen model listed in Section 4.2, and extends them to a two screen configuration. The key additional hypothesis introduced here concerns the static pressure field at the inter screen plane, located between the downstream face of Screen 1 and the upstream face of Screen 2.

Only one axial station is present in the middle of the two screens, where quantities are calculated as the output of screen 1 and used as an input for screen 2 losses correlations. The only global static pressure constraint is applied once, across the entire two screen assembly. The antisymmetric hypothesis is extended to read:

$$\frac{P_{s,2,i} + P_{s,4,i}}{2} = \overline{\left(\frac{P_{s,2} + P_{s,4}}{2}\right)} = \overline{P_{avg}} \quad \forall\, i, \tag{5.3}$$

This condition, which mirrors the single-screen formulation of equation 4.3, now bridges the entire two screen assembly, embeds the aerodynamic coupling between the two elements: the Mach number at Station 2 is adjusted by the combined effect of both screens simultaneously, since the residual of equation 5.3 depends on the loss coefficients and Mach numbers of both screens.

5.2.2. Governing Equations and Loss Model

The isentropic relations and the screen loss model are identical to those described in Chapter 4. The loss coefficient for Screen 1, $K_{c1,i}$, is evaluated at Station 2 conditions:

$$K_{c1,i} = G(\beta_{1,i}) \cdot f_{Re}(\mathrm{Re}_{d_{w1},i}) \cdot f_{Ma}(M_{2,i}, \beta_{1,i}), \tag{5.4}$$

and the total pressure at the inter-screen plane Station 3 is:

$$P_{t,3,i} = P_{t,2,i} - K_{c1,i} \cdot P_{s,2,i} \cdot (f_\gamma(M_{2,i}) - 1). \tag{5.5}$$

The loss coefficient for Screen 2, $K_{c2,i}$, is evaluated at Station 3 conditions using the inter screen Mach number $M_{3,i}$ and the Screen 2 porosity $\beta_{2,i}$:

$$K_{c2,i} = G(\beta_{2,i}) \cdot f_{Re}(\mathrm{Re}_{d_{w2},i}) \cdot f_{Ma}(M_{3,i}, \beta_{2,i}), \tag{5.6}$$

and the total pressure at Station 4 is:

$$P_{t,4,i} = P_{t,3,i} - K_{c2,i} \cdot P_{s,3,i} \cdot (f_\gamma(M_{3,i}) - 1). \tag{5.7}$$

Note that the Mach number and static pressure at Station 3 depend on the upstream Mach number $M_{2,i}$ through the loss and isentropic relations; consequently, the static pressure at Station 4 also depends on $M_{2,i}$. This is the mathematical expression of the coupling: the closing condition of equation 5.3 must be satisfied simultaneously for both screens, and a single iterative loop acting on $M_{2,i}$ is enough to achieve convergence.

5.2.3. Iterative Solution Algorithm

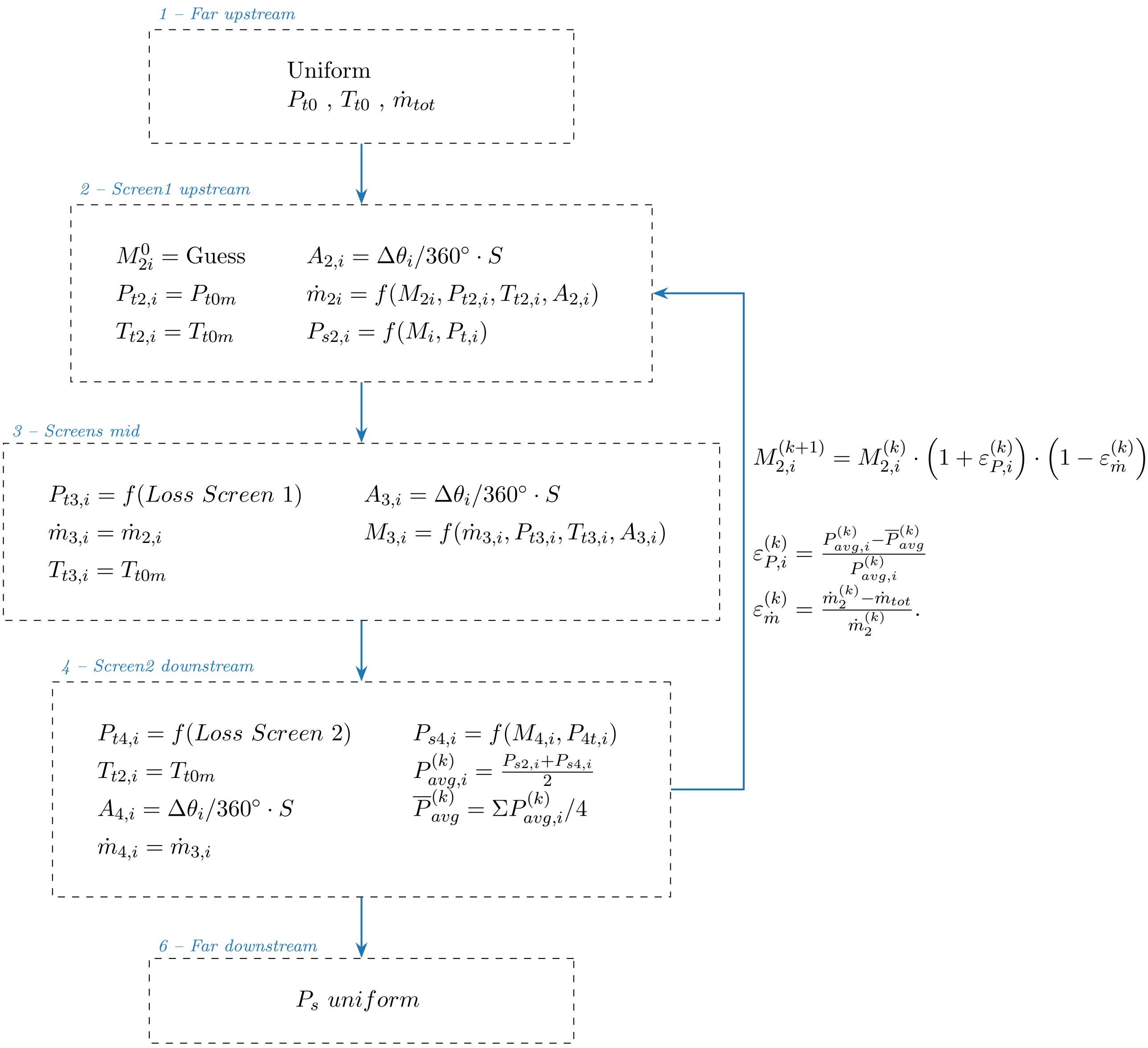

Figure 5.3: Flowchart of the iterative solution algorithm for the Coupled dual screen model.

The Coupled model is solved by a single main iterative loop that simultaneously enforces the unified antisymmetric static pressure condition, equation 5.3, and the global mass flow constraint, equation 4.16. The structure of the loop is an extension of the single screen algorithm described in Section 4.6.

Initialisation. All sector Mach numbers at Station 2 are initialised to a fixed uniform value $M_{2,i}^{(0)}$.

Main loop. At each iteration k, the following steps are performed in sequence:

1. **Screen 1 upstream (Station 2).** From the current estimate $M_{2,i}^{(k)}$ and the known uniform values $P_{t,0}$ and $T_{t,0}$, the isentropic relations are applied to compute $P_{s,2,i}$, $T_{s,2,i}$, $\rho_{2,i}$ and $V_{2,i}$. The sector mass flow $\dot{m}_{2,i} = \rho_{2,i} V_{2,i} A_i$ and the total mass flow $\dot{m}_2 = \sum_i \dot{m}_{2,i}$ are evaluated.

2. **Screen 1 loss and inter-screen state (Station 3).** The Screen 1 loss coefficient $K_{c1,i}$ is computed. The total pressure $P_{t,3,i}$ is obtained from equation 5.5. The Mach number $M_{3,i}$ is calculated from equation 4.17, and the static pressure $P_{s,3,i}$ follows from the isentropic relation.

3. **Screen 2 loss and downstream state (Station 4).** The Screen 1 loss coefficient $K_{c1,i}$ is computed at Station 3 conditions. The total pressure $P_{t,4,i}$ is obtained from equation 5.7. The Mach number $M_{3,i}$ is calculated from equation 4.17, and the static pressure $P_{s,3,i}$ follows from the isentropic relation..

4. **Residual evaluation and Mach number update.** The sector-averaged static pressure is computed as the mean of the upstream static pressure of screen 1 and downstream static pressure of screen 2 :

$$P_{avg,i}^{(k)} = \frac{P_{s,2,i}^{(k)} + P_{s,4,i}^{(k)}}{2}. \tag{5.8}$$

The circumferential average $\overline{P}_{avg}^{(k)}$ is then obtained. The relative residuals are:

$$\varepsilon_{P,i}^{(k)} = \frac{P_{avg,i}^{(k)} - \overline{P}_{avg}^{(k)}}{P_{avg,i}^{(k)}}, \qquad \varepsilon_{\dot{m}}^{(k)} = \frac{\dot{m}_2^{(k)} - \dot{m}_{tot}}{\dot{m}_2^{(k)}}. \tag{5.9}$$

The sector Mach numbers are updated with the same proportional correction used in the single-screen model:

$$M_{2,i}^{(k+1)} = M_{2,i}^{(k)} \cdot \left(1 + \varepsilon_{P,i}^{(k)}\right) \cdot \left(1 - \varepsilon_{\dot{m}}^{(k)}\right). \tag{5.10}$$

Convergence is declared when $\max_i |\varepsilon_{P,i}^{(k)}| < 10^{-6}$ and $|\varepsilon_{\dot{m}}^{(k)}| < 10^{-6}$ simultaneously.

Once the main loop has converged, the far-upstream state (Station 1) is calculated analytically from the sector mass flows, and the far-downstream state (Station 5) is computed by a secondary iterative loop that enforces circumferential static pressure equalization and total area conservation at the exit plane, following the identical procedure described in Section 4.6 for the single screen model.

5.3. Decoupled Model

5.3.1. Axial Stations and Physical Hypothesis

Six axial stations are defined for the decoupled model, as illustrated schematically in Figure 5.4:

- **Station 1 – Far upstream**: circumferentially uniform inlet conditions with $P_{t,1,i} = P_{t,0}$ and $T_{t,1,i} = T_{t,0}$ for all sectors i.
- **Station 2 – Screen 1 upstream**: immediately upstream of Screen 1. This is the station where the loss correlations for Screen 1 are evaluated, since the local Mach number, Reynolds number and dynamic pressure involved in the calculation of the loss coefficient are those of the inlet flow.
- **Station 3 – Screen 1 downstream**: immediately downstream of Screen 1. Total pressure is reduced by $K_{c1,i}$ relative to Station 2.
- **Station 4 – Screen 2 upstream**: immediately upstream of Screen 2. The total pressure at this station is set to the converged values of Station 3, $P_{t,4,i} = P_{t,3,i}$, so that the distorted total pressure profile produced by Screen 1 is carried forward. This is the station where the loss correlations for Screen 2 are evaluated.
- **Station 5 – Screen 2 downstream**: immediately downstream of Screen 2. Total pressure is further reduced by $K_{c2,i}$ relative to Station 4.
- **Station 6 – Far downstream**: sufficiently far downstream of Screen 2 for the static pressure to equalize circumferentially.

The decoupled model is based on a different assumption regarding the inter screen region: the axial distance between Screen 1 and Screen 2 is assumed to be large enough for the flow redistribution mechanism to happen independently in each distortion screen. This implies that the upstream potential effect of screen 2 does not affect the flow redistribution of screen 1. Each screen then operates as an independent aerodynamic element, and the model reduces to two successive applications of the single screen model described in Chapter 4.

The decoupled model applies the antisymmetric static pressure condition independently

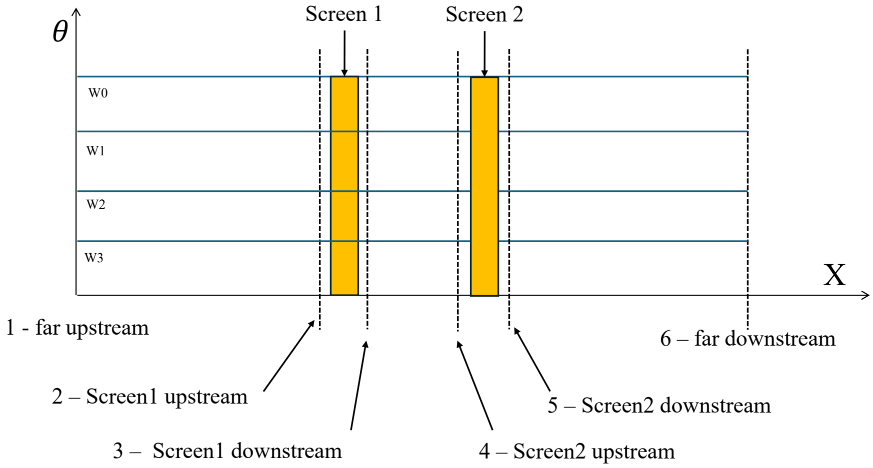

Figure 5.4: Schematic of the decoupled dual screen model showing the six axial stations. θ: circumferential direction. X: Axial direction.

to each screen:

$$\frac{P_{s,2,i} + P_{s,3,i}}{2} = \overline{\left(\frac{P_{s,2} + P_{s,3}}{2}\right)} = \overline{P_{avg,1}} \quad \forall\, i, \tag{5.11}$$

$$\frac{P_{s,4,i} + P_{s,5,i}}{2} = \overline{\left(\frac{P_{s,4} + P_{s,5}}{2}\right)} = \overline{P_{avg,2}} \quad \forall\, i, \tag{5.12}$$

The two conditions, equations 5.11 and 5.12, are enforced by two separate and independent iterative loops. The quantities $\overline{P_{avg,1}}$ and $\overline{P_{avg,2}}$ are not imposed to a fixed value, they are a result of the model.

5.3.2. Iterative solution algorithm

The decoupled model is implemented through a modular architecture built around the function which includes the complete iterative algorithm of the single screen model for a generic screen. The single screen model takes as inputs the ones defined in Section 4.4 and outputs the fluid properties in the four axial stations.

The two-screen analysis is then performed by calling this function twice in sequence. A flowchart of the Decoupled model is presented in Figure 5.5:

Stage 1: Screen 1 analysis. The solver is called with the Screen 1 mesh properties and a uniform inlet total pressure $P_{t,in,i} = P_{t,0}$. This produces the converged screen 1 upstream state, the screen 1 downstream state and the far upstream uniform conditions.

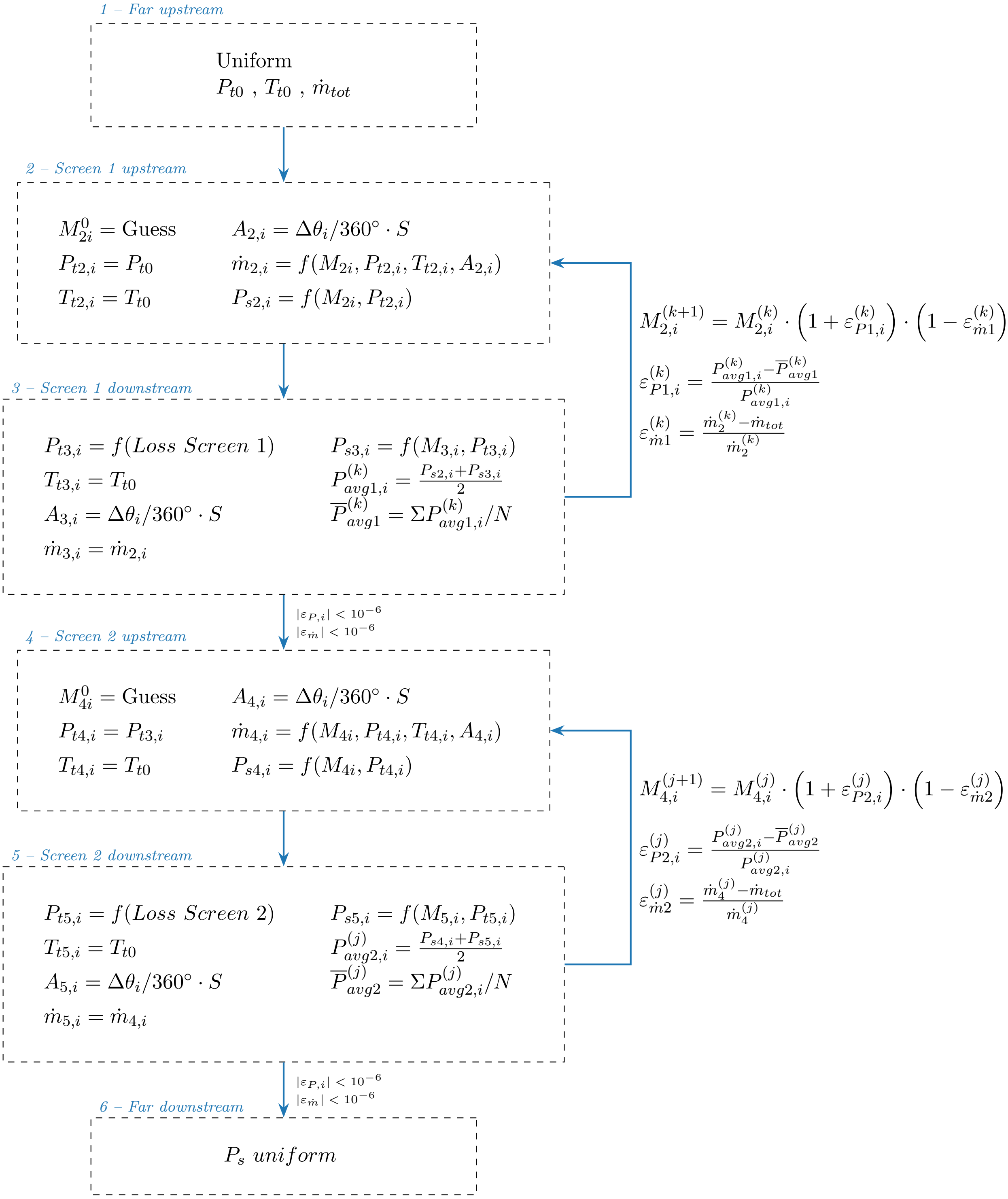

Figure 5.5: Flowchart of the iterative solution algorithm for the Decoupled dual screen model.

The antisymmetric condition of equation 5.11 is enforced internally by the solver, and the converged sector Mach numbers at Station 2 reflect the redistribution produced by Screen 1 alone.

Stage 2: Screen 2 analysis. The solver is called again, now with the Screen 2 mesh properties and the downstream total pressure of Screen 1 as inlet condition: $P_{t,in,i}^{(S2)} = P_{t3,i}$, where $P_{t,3,i}$ is the converged pressure distortion profile generated by Screen 1. The antisymmetric condition of equation 5.12 is enforced independently within the second solver call: a new iterative loop adjusts the Mach numbers at Station 4 until the condition is satisfied for Screen 2 alone, with no reference to any upstream state of Screen 1.

Once the two screen analysis have converged, the far downstream section is calculated, where the static pressure has become uniform, following the same procedure as the one described in Section 4.6.

This sequential structure is the mathematical expression of the uncoupling assumption: the convergence of the Screen 2 loop depends only on the total pressure inherited from Screen 1 and on the Screen 2 mesh properties, not on the static pressure at Station 2 or on the Mach number redistribution produced by Screen 1.

5.4. Results and Physical Interpretation

The results of both the Coupled and Decoupled models are presented in Figures 5.6–5.8, which show the axial evolution of the normalised total pressure P_t/P_{ref}, Mach number M, and normalised static pressure P_s/P_{ref} for four circumferential sectors.

the resulted are presented for a specific application case: two identical screens in series, both with the same characteristics are the one described in Chapter 3.

Total pressure. In both models the 0–30° sector is characterized by the lowest total pressure losses, since it is clean for both screens, while the 100–300° sector experiences the greatest drop. The key difference between the two models in the total pressure drop is the quantities used to calculate the total pressure coefficient. Since the total pressure drop depends on both the upstream Reynolds number and the upstream dynamic pressure, which have different values between the two models, given their different structure, the two models show different total pressure loss values across the two screens.

Static pressure. The static pressure evolution makes the physical distinction between the two models most apparent. The yellow shaded bands indicate the axial regions where

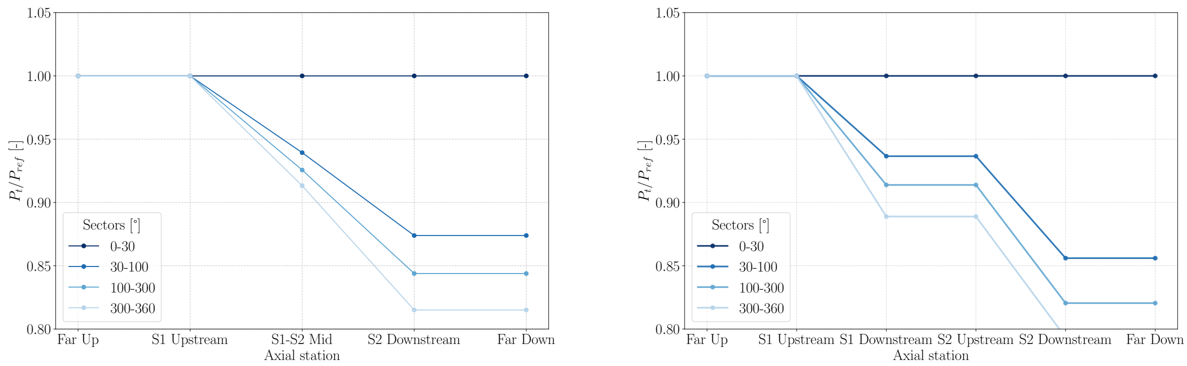

(a) (b)

Figure 5.6: Normalised total pressure P_t/P_{ref} along the axial stations for the Coupled model (a) and the Decoupled model (b).

the antisymmetric static pressure condition is enforced: in the Coupled model this spans from Screen 1 upstream to Screen 2 downstream as a single region, whereas in the Decoupled model two separate bands appear, one for each screen independently. Both models recover a common static pressure level at the Far Down section.

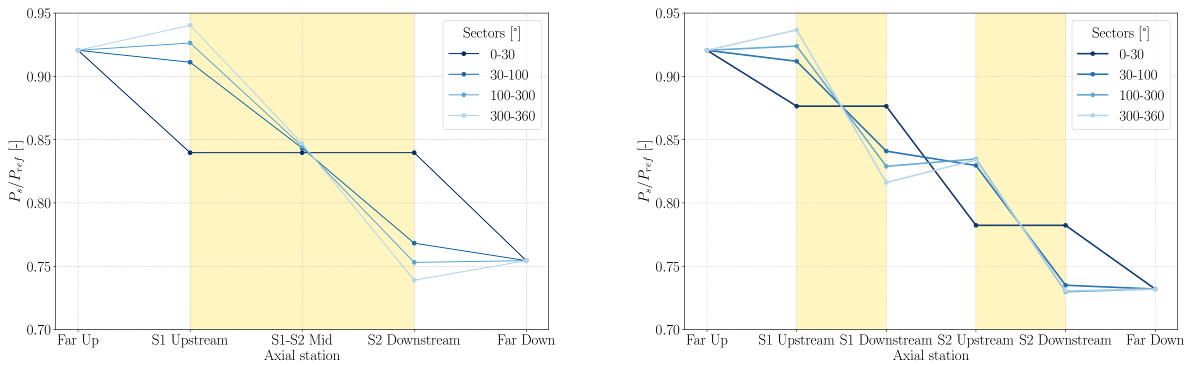

(a) (b)

Figure 5.7: Normalised static pressure P_s/P_{ref} along the axial stations for the Coupled model (a) and the Decoupled model (b). The yellow bands indicate the axial regions where the antisymmetric static pressure condition is applied.

Mach number. The Mach number profiles reflect the mass flow redistribution driven by the screen resistance. In the Coupled model the 0–30° sector accelerates sharply across the merged screen station, reaching $M \approx 0.65$ at the Far downstream plane. The Decoupled model produces a two stage acceleration for the same sector: M rises to approximately 0.60 already at S2 Upstream before climbing further to $M \approx 0.68$ far downstream, a

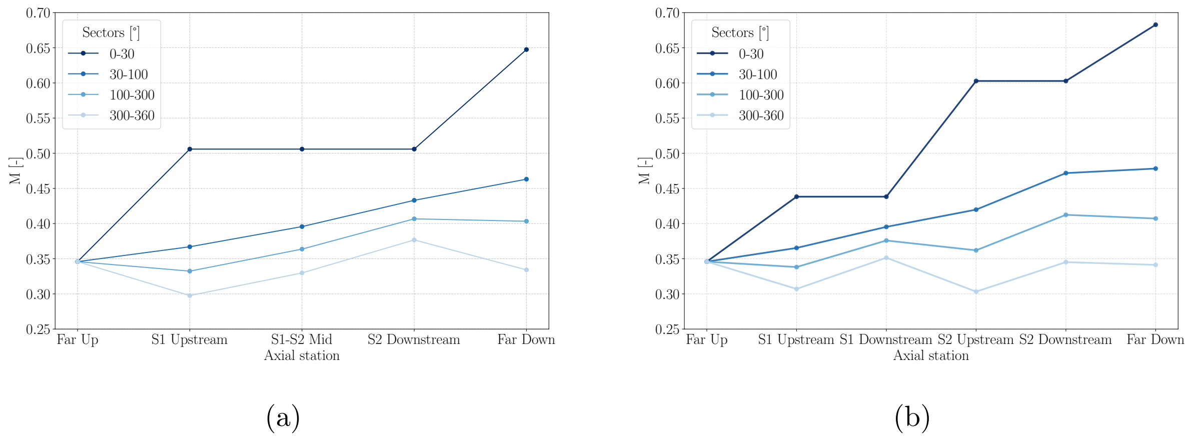

Figure 5.8: Mach number M along the axial stations for the Coupled model (a) and the Decoupled model (b).

notably higher peak than in the Coupled case.

The two formulations represent opposite physical limits. The Decoupled model is appropriate when the downstream screen's potential effects does not affect the upstream screen's redistribution; the Coupled model becomes appropriate when the two screens share the same flow redistribution mechanism.

Since the potential back pressure effect of a single screen is limited to a certain axial region in the vicinity of the screen, the most relevant variable to represent this different behaviour is the axial distance ΔX between the two screens: the Coupled model represents the case where the two screens are almost adjacent ($\Delta X \approx 0$), while the Decoupled model represents the condition where the two screens are sufficiently distant to avoid any back pressure effect on the upstream screen. This distance will be estimated in the following sections.

5.5. Validation Against Two Screen CFD

The Coupled and Decoupled models are validated against a set of two screen CFD simulations, computed with the same numerical setup as described in Chapter 3 for the single screen reference case. Two identical distortion screens, each sharing the same sector geometry and mesh properties as the screen characterised in Chapter 3, are placed in series within the annular duct. The axial separation between the two screens, ΔX, is expressed as a fraction of the duct mean diameter D_m: $\Delta X_{adim} = \Delta X / D_m$. The normalised screen distance is varied parametrically to span the range from nearly adjacent ($\Delta X_{adim} = 0.06$) to well separated ($\Delta X_{adim} = 1.15$), thereby covering both the regime where the Coupled model is expected to be appropriate and the regime where the Decoupled model should converge to the correct limit.

For each separation distance, the CFD solution provides axial profiles of normalised static pressure P_s/P_{ref} and Mach number M extracted along four axial lines at the circumferential midpoint of each sector W0–W3. The model predictions are evaluated at the five (Coupled) or six (Decoupled) axial stations defined in Sections 5.2 and 5.3, and superimposed on the continuous CFD profiles.

5.5.1. Small Screen Distance: $\Delta X_{adim} = 0.06$

Figure 5.9 shows the normalised total and static pressure profiles for the small screen separation case. Because the two screens are nearly adjacent at this spacing, the X axis doesn't show the full domain but only the portion near the screens for better visualization.

When the distortion screens are so close to each other, the static pressure value stays almost constant between the two screens in the distorted sectors, where the back pressure effect of the downstream screen impacts the upstream one. The Coupled model clearly has a better match than the Decoupled model for this screen distance. A quantitative analysis of the model's accuracy is presented in Section 5.5.3

5.5.2. Large Screen Distance: $\Delta X_{adim} = 1.15$

Figure 5.10 shows the total and static pressure profiles for the large screen separation case. At this separation, the flow has sufficient axial length between the two screens to develop a distinct second distortion region: the CFD profiles show a clear two step pressure structure, with one pressure transition at the first screen and a second, equally sharp transition at the second screen.

By enforcing the antisymmetric static pressure condition independently at each screen, the Decoupled model matches the two step pressure structure observed in the CFD. The model predictions at the second screen upstream and downstream stations agree well with the CFD profiles for all four sectors. The far downstream asymptotic levels are also correctly recovered by both models.

5.5.3. Model Validity Range

The qualitative comparisons at the two screen separation already establish that the Coupled and Decoupled models represent two opposite physical limits. To quantify this behaviour systematically across the full range of screen separations investigated, an error

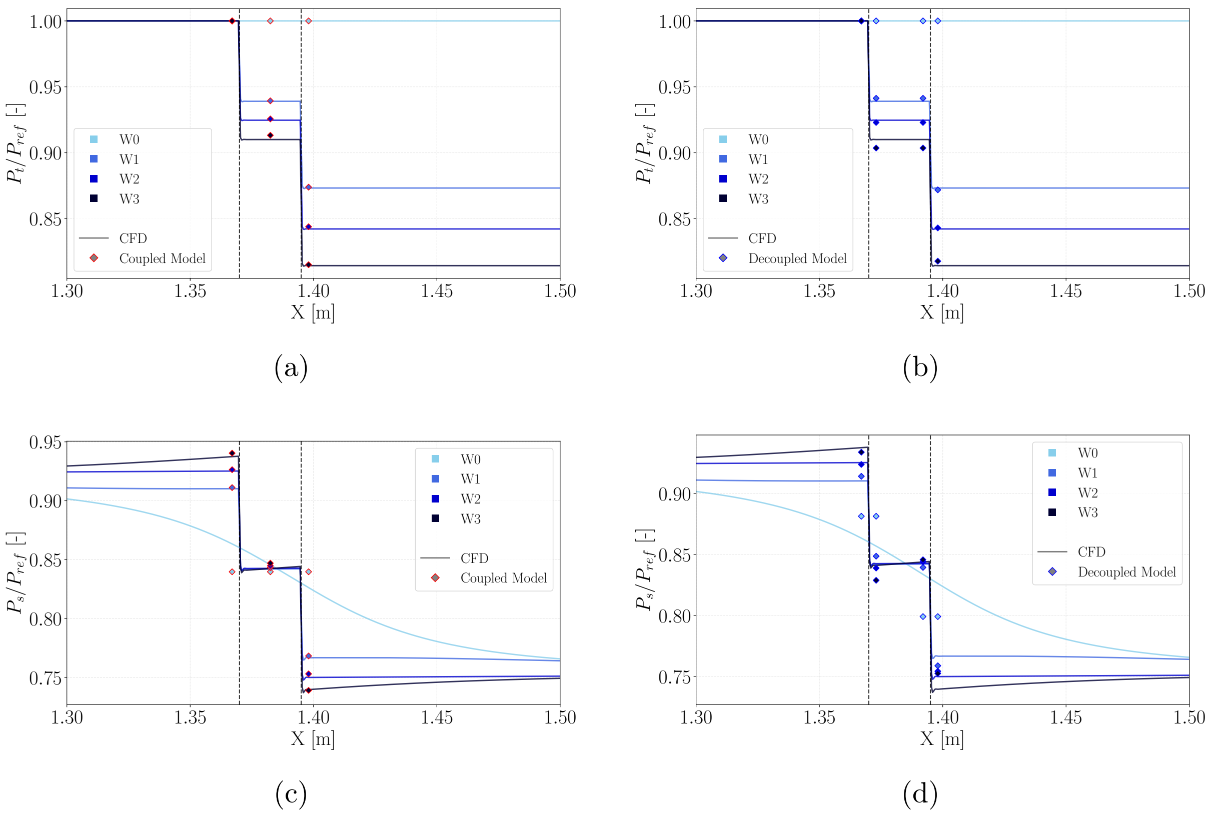

Figure 5.9: Normalized pressures for the two-screen configuration with $\Delta X_{adim} = 0.06$. The top row shows normalized total pressure P_t/P_{ref} for (a) the Coupled model and (b) the Decoupled model. The bottom row shows normalized static pressure P_s/P_{ref} for (c) the Coupled model and (d) the Decoupled model. Solid lines denote CFD profiles. Filled symbols represent model predictions: Coupled model (blue diamonds) and Decoupled model (red diamonds).

analysis has been carried out by comparing model predictions against CFD reference data at seven inter screen distances ΔX_{adim}: 0.06, 0.11, 0.23, 0.46, 0.69, 0.92, 1.15.

The error metric adopted to compare each model against the CFD reference is the Root Mean Square Relative Error (RMSRE). For a given flow variable q (Mach number M, static pressure P_s, or total pressure P_t), the local relative error at axial station k and circumferential sector i is defined as the ratio:

$$\epsilon_{k,i} = \frac{q_{k,i}^{\text{model}} - q_{k,i}^{\text{CFD}}}{q_{k,i}^{\text{CFD}}}, \tag{5.13}$$

where $q_{k,i}^{\text{CFD}}$ is the CFD value sampled at the axial position closest to the model station k, and $q_{k,i}^{\text{model}}$ is the corresponding model prediction.

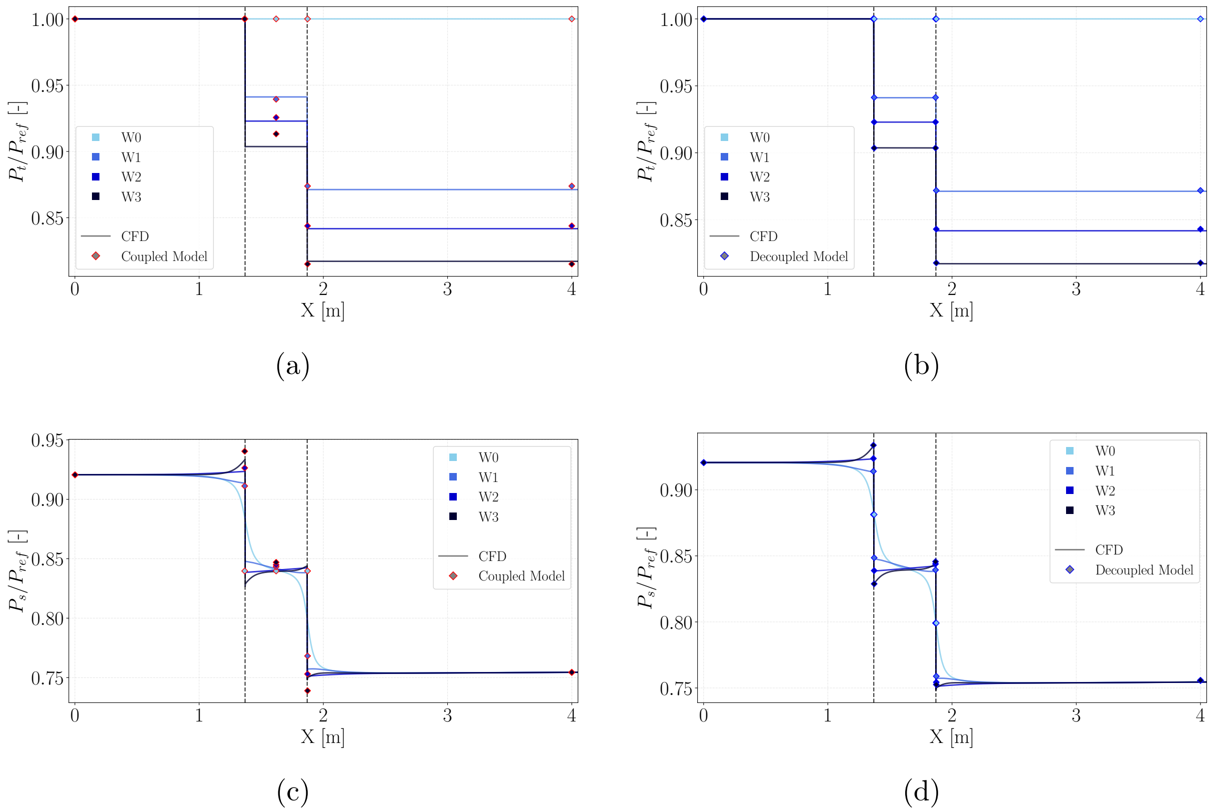

Figure 5.10: Normalized pressures for the two-screen configuration with $\Delta X_{adim} = 1.15$. The top row shows normalized total pressure P_t/P_{ref} for (a) the Coupled model and (b) the Decoupled model. The bottom row shows normalized static pressure P_s/P_{ref} for (c) the Coupled model and (d) the Decoupled model. Solid lines denote CFD profiles. Filled symbols represent model predictions: Coupled model (blue diamonds) and Decoupled model (red diamonds).

The RMSRE aggregates the local errors over all N_s model stations and N_c circumferential sectors into a single scalar:

$$\text{RMSRE} = \sqrt{\frac{1}{N_s \cdot N_c} \sum_{k=1}^{N_s} \sum_{i=1}^{N_c} \epsilon_{k,i}^2}. \tag{5.14}$$

By squaring the individual relative errors before averaging, the RMSRE naturally penalises large local discrepancies more heavily than small ones.

The results of this analysis are shown in Figure 5.11 for the two models across all seven screen separations. The behaviour is clear: the Coupled model (red) achieves its lowest RMSRE at small screen separations and its error grows as ΔX_{adim} increases, reaching a plateau above approximately $\Delta X_{adim} = 1$. The Decoupled model (blue) shows the

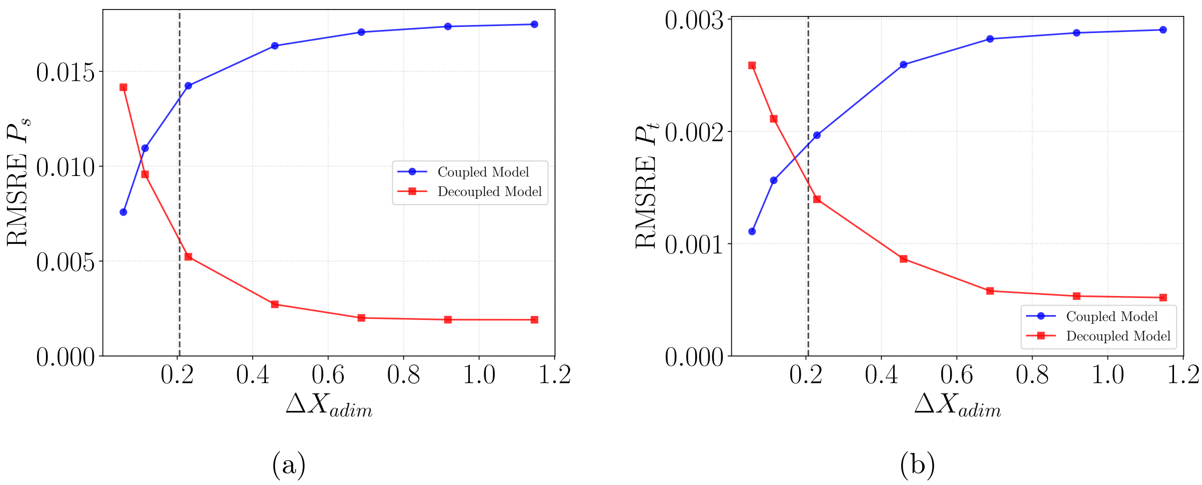

Figure 5.11: Root Mean Square Relative Error (RMSRE) as a function of inter-screen distance ΔX for static pressure (a), and total pressure (b). Blue curve and dots: Coupled model. Red curve and dots: Decoupled model.

opposite trend: its RMSRE is highest at small separations, as expected.

These error curves make explicit what the qualitative comparisons already suggested: neither model is universally valid across the full range of ΔX. The Coupled model is appropriate only in the limit of closely spaced screens ($\Delta X_{adim} \lesssim 0.1$), where its low-error behaviour is maintained, while the Decoupled model is the correct choice only for well-separated screens ($\Delta X_{adim} \gtrsim 0.7$). In the intermediate range both models incur significant errors, and neither formulation is physically self consistent. The transition between the two regimes is gradual, and no single threshold ΔX_{adim} separates them cleanly. Furthermore, in the VKI experimental setup, the axial distance between the distortion screen and the IGV row, shown in Figure 5.11 as a black dashed line, is in the middle of the transition region, where neither one of the two models correctly represents the flow physics.

This observation motivates the construction of a third modelling approach that interpolates continuously between the two models as a function of the inter screen distance, combining the strengths of each formulation across the full operating range.

5.6. Hybrid Model

5.6.1. Interpolation Scheme

The normalised distance is defined as:

$$x_{\text{norm}} = \frac{\Delta X - \Delta X_{\text{min}}}{\Delta X_{\text{max}} - \Delta X_{\text{min}}} \tag{5.15}$$

Where ΔX is the physical inter screen distance and ΔX_{min}, ΔX_{max} are the reference distances corresponding to the fully coupled and fully decoupled limits, respectively. In the present study, they are chosen to span the transition region identified by the error curves.

For simplicity, in the equations, the Decoupled model is referred as V1, while the Coupled model is referred as V2. The weight assigned to the Coupled model is defined by the exponentially decaying function:

$$W_{V2}(x_{\text{norm}}) = \frac{e^{-k\,x_{\text{norm}}} - e^{-k}}{1 - e^{-k}}, \tag{5.16}$$

where $k \geq 0$ is a shape parameter that controls the rate of decay. In the limit $k \to 0$, equation 5.16 reduces to a purely linear interpolation $W_{V2} = 1 - x_{\text{norm}}$, while for $k > 0$ the transition becomes increasingly concentrated at small x_{norm}, rapidly down-weighting the Coupled model as soon as the screens are no longer in close proximity. The complementary weight for the Decoupled model is:

$$W_{V1}(x_{\text{norm}}) = 1 - W_{V2}(x_{\text{norm}}). \tag{5.17}$$

The normalisation in equation 5.16 ensures that $W_{V2}(0) = 1$ and $W_{V2}(1) = 0$ for all values of k, so that the hybrid model reduces exactly to the Coupled model at $x_{\text{norm}} = 0$ and to the Decoupled model at $x_{\text{norm}} = 1$.

5.6.2. Station Grid Matching

The two constituent models do not share the same axial station layout: the Coupled model is defined on six stations (far upstream, S1 upstream, S1 downstream, S2 upstream, S2 downstream, far downstream), while the Decoupled one uses five stations (far upstream, S1 upstream, inter-screen midplane, S2 downstream, far downstream). To form a well posed weighted average, the Coupled model must first be mapped onto the Decoupled model station grid.

The only region where interpolation is needed is the axial stations in between the two distortion screens. This region is modelled with two axial stations by the Decoupled model: S1 downstream, S2 upstream; and only with one axial station by the Coupled model: Screens mid. The resampling is done by linearly interpolating the value of the Decoupled model between S1 downstream and S2 upstream, and using the mid point value, which corresponds to the Screens mid axial station.

Once the Coupled model has been resampled onto the five Decoupled model stations, the hybrid prediction at each station and sector is the weighted average. The quantity q at an axial station j and sector i can be calculated:

$$q_{j,i}^{\mathrm{Hyb}} = W_{V1} \cdot q_{j,i}^{V1} + W_{V2} \cdot q_{j,i}^{V2} \tag{5.18}$$

where the weights W_{V1} and W_{V2} depend only on ΔX through equations 5.15–5.17 and are therefore constant across all stations and sectors for a given configuration.

To ensure thermodynamic and kinematic consistency within the hybrid model, a specific set of base flow variables and geometric parameters are spatially interpolated between the decoupled and coupled solutions. Specifically, the total pressure, Mach number, total temperature, stream-tube area, and absolute flow angle are linearly interpolated.

Conversely, dependent flow variables, such as static pressure, static temperature, density, flow velocity, and sector mass flow rate, are not directly interpolated, as the linear combination of these non-linear quantities would violate the gas dynamic equations of state. Instead, a provisional sector mass flow rate is initially evaluated from the interpolated base variables.

To strictly enforce the conservation of the overall mass flow, a correction factor is applied to these provisional local mass flow rates, scaling them to match the target global mass flow. From this corrected, mass-conserving flow rate, the true Mach number is inversely recalculated using the compressible mass flow equation. Subsequently, all other Mach-dependent static and kinematic quantities, namely static pressure, static temperature, density, and flow velocity, are derived with the exact isentropic relations and the ideal gas law, ensuring the complete physical and thermodynamic closure of the hybrid model.

5.6.3. Sensitivity to the Shape Parameter k

The shape parameter k governs how rapidly the hybrid model transitions from the Coupled to the Decoupled limit. To assess its influence systematically, the hybrid model was evaluated for $k \in \{0, 2, 4, 6, 8\}$ across the full range of inter-screen distances. The corresponding weight functions and RMSRE curves for all three flow variables are shown in

Figure 5.12.

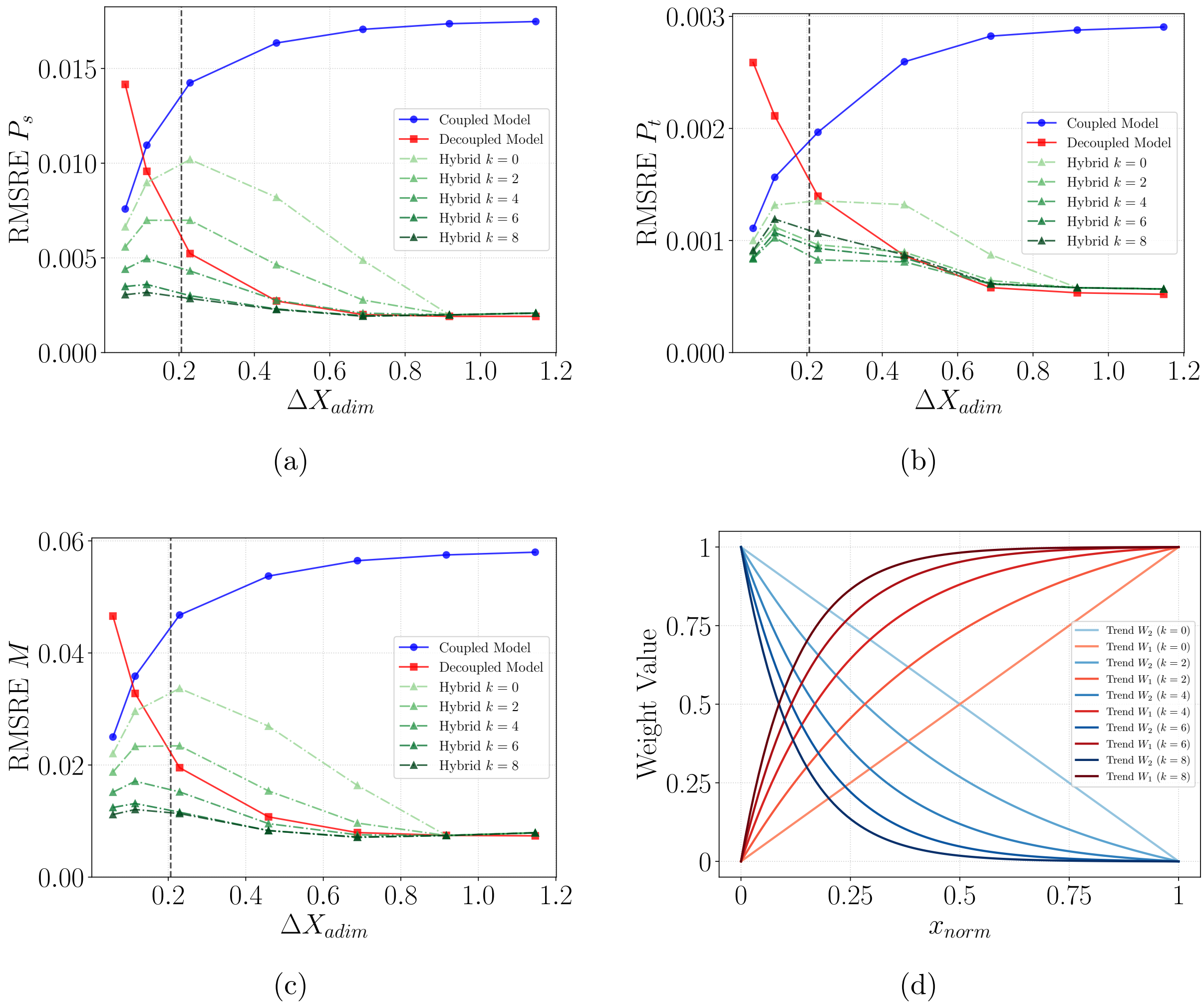

Figure 5.12: Sensitivity of the Hybrid model to the shape parameter k. RMSRE as a function of inter-screen distance ΔX_{adim} for static pressure (a), total pressure (b), and Mach number (c). Blue curve: Coupled model. Red curve: Decoupled model. Green curves of increasing darkness: Hybrid model for $k = 0, 2, 4, 6, 8$. Plot (d) shows the corresponding weight functions W_{V1} and W_{V2} as a function of x_{norm} for each value of k.

The results show a clear and consistent trend across all three variables: larger values of k produce lower RMSRE across the full range of ΔX_{adim}, with the most significant improvement occurring in the intermediate range $0.05 \lesssim \Delta X_{adim} \lesssim 0.4$. At $k = 0$ (linear interpolation) the hybrid model still exhibits a pronounced error bump in this intermediate region, which is progressively suppressed as k increases. This behaviour is consistent with the weight plot in Figure 5.12d: a larger k concentrates the transition at small x_{norm}, rapidly assigning dominant weight to the Decoupled model as soon as the screens are no longer in close proximity, which is physically consistent with the exponential growth of the Coupled model error observed in Figure 5.11.

To determine the optimal value of k quantitatively, which is the value that minimized the overall error, the RMSRE over static and total pressure was minimised over a continuous range $k \in [0, 12]$. The result is shown in Figure 5.13.

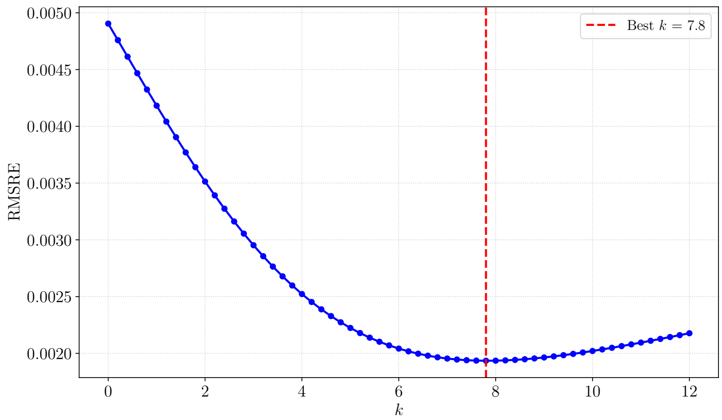

Figure 5.13: Mean RMSRE over static and total pressure as a function of the shape parameter k. The red dashed line marks the optimal value $k^* = 7.8$ that minimises the global error.

The error curve exhibits a well-defined minimum at $k^* = 7.8$, confirming that the optimal transition corresponds to a specific exponential decay rate that matches the physical relaxation of aerodynamic coupling with inter-screen distance.

5.6.3.1. Flow Field Comparison

To illustrate the improvement provided by the Hybrid model, Figure 5.14 shows the Mach number profiles predicted by the three models against the CFD reference for an inter-screen distance of $\Delta X_{adim} = 0.11$. This distance falls in the intermediate transition region identified in Figure 5.11, where neither the Coupled nor the Decoupled model individually provides an accurate representation of the flow.

At this separation the screens are far enough apart that the flow has partially re-equilibrated between them, so the Coupled assumption is too rigid. The Decoupled model, Figure 5.14b, applies the opposite assumption: it treats each screen as fully independent. This assumption is equally incorrect, as the inter-screen distance is too short for the screens to be completely independent from each other.

The Hybrid model, Figure 5.14c, blends the two constituent solutions with weights determined by the optimised shape parameter $k^* = 7.8$. At $\Delta X_{adim} = 0.11$ the hybrid

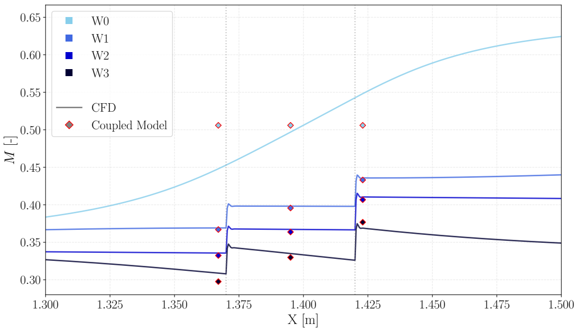

(a) Coupled Model

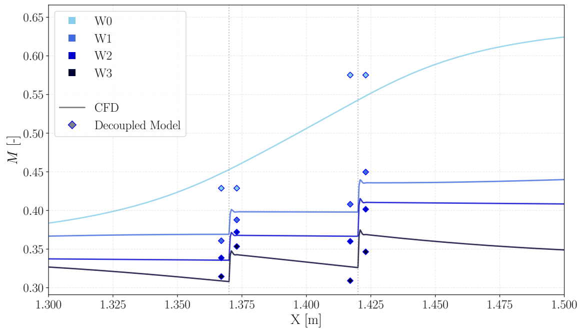

(b) Decoupled Model

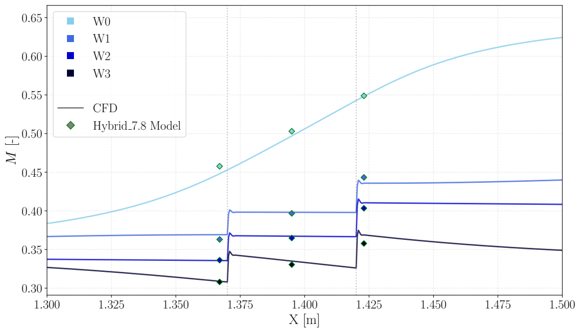

(c) Hybrid Model ($k^* = 7.8$)

Figure 5.14: Mach number profiles for the four circumferential sectors (W0–W3) as a function of axial position at an inter-screen distance $\Delta X_{adim} = 0.11$. Solid lines: CFD reference. Symbols: model predictions.

weights assign a dominant but not exclusive contribution to the Coupled solution. The resulting Mach number profiles match the CFD reference substantially better than either constituent model alone across all four sectors, correctly capturing both the magnitude and the circumferential pattern of the flow redistribution imposed by the two-screen system. The biggest improvement is in the clean sector, where the smooth Mach number increase is best capture by the Hybrid model.

6 | Screen–IGV Model

The dual-screen model of Chapter 5 has been developed as an intermediate step, before introducing the IGV in the model. The dual-screen model treats two elements in series, Screen 1 and Screen 2, as equivalent resistive elements, each characterised by a local total pressure loss coefficient K_c derived from empirical wire-mesh correlations. In the DREAM test section, however, the second resistive element is not a passive mesh but an active blade row: the Inlet Guide Vane (IGV). The IGV introduces total pressure losses and flow turning that are fundamentally different in nature from those of a wire mesh, yet the mathematical structure of the stream-tube model is sufficiently general to account for this difference.

A porous screen and a re-staggered blade row act as a localised, circumferentially non-uniform resistance element. Both elements impose a total pressure drop on the passing stream-tubes, and both establish a circumferential static pressure gradient that drives annular mass flow redistribution. The fundamental difference lies in the physical mechanism generating the loss and in its functional dependence on the local flow conditions.

For the distortion screen, the loss is governed by the wire geometry (porosity β and wire diameter d_w) and the local dynamic pressure, as captured by the empirical correlations of Section 4.5. For a re-staggered IGV, instead, the loss mechanism is mainly driven by the inlet Mach and incidence on the blade. In addition, the IGV introduces a non-zero exit swirl angle α_{out}, which must be accounted for in a blade row model, since the axial component of the velocity is the only one contributing to the mass-flow.

The analysis is therefore performed by retaining the complete mathematical structure of the dual-screen model, the stream-tube discretisation, the isentropic relations, the anti-symmetric static pressure hypothesis, and the hybrid weighting strategy, and replacing only the loss and deviation sub-models at the location of Screen 2 with their IGV equivalents. No other modification to the model architecture is required.

6.1. IGV Loss and Deviation Correlations

The mean-line model adopted for the Inlet Guide Vane (IGV) row relies on two correlations from the classical cascade literature: Carter's rule extended by Lieblein for the outlet deviation angle, and the Lieblein profile loss formula for the total pressure loss coefficient.

The total pressure loss correlation depends on quantities that are only known at the blade-row exit: the exit flow angle α_2 and the exit Mach number M_2 appear explicitly in the equations, while the loss coefficient $\tilde{\omega}_p$ determines the exit total pressure p_{02}. This in turn sets the local density ρ_2, velocity V_{x2}, and Mach number entering both correlations. The two equations are therefore coupled, and an iterative cycle is required to reach a thermodynamically and aerodynamically consistent solution at the IGV exit plane. The iterative cycle is shown in Figure 6.1

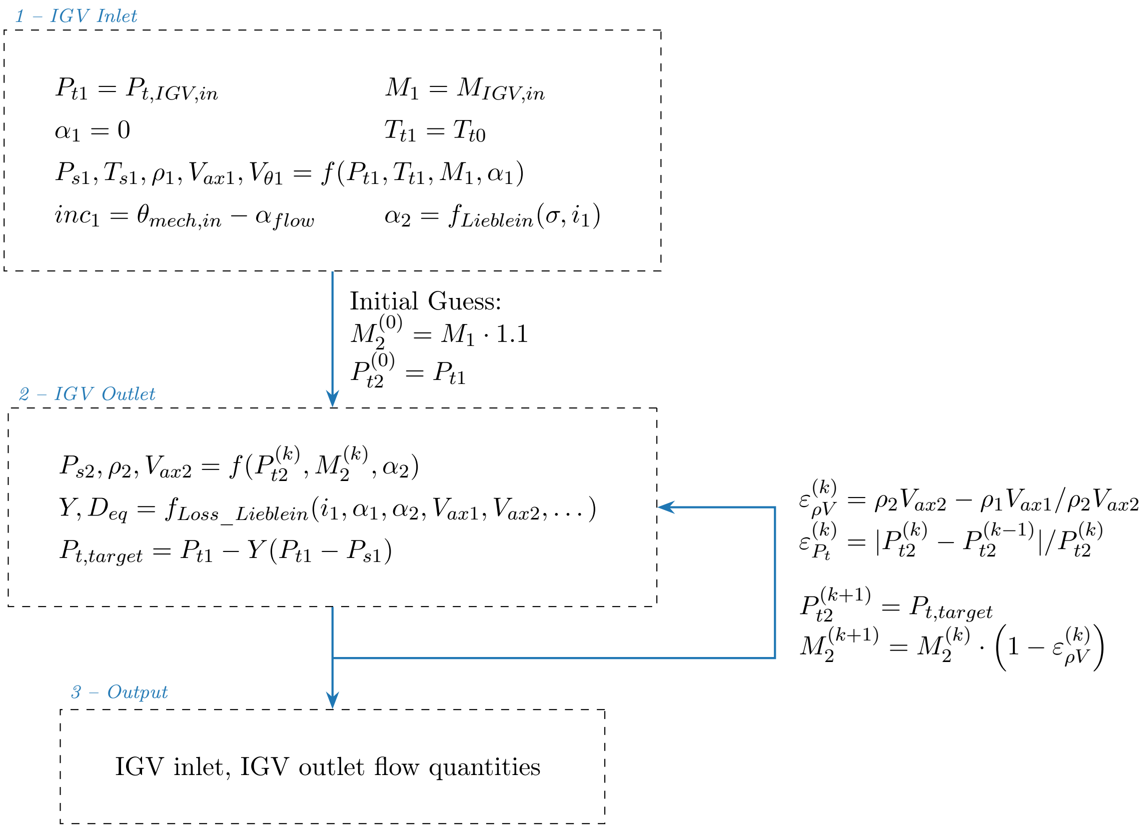

Figure 6.1: Flowchart of the iterative solution algorithm for the IGV model.

6.1.1. total pressure Loss Coefficient

The evaluation of the profile loss coefficient $\tilde{\omega}_p$ is based on the model developed by Lieblein [18]. This is preliminary model, and only profile losses are considered, in the future, a more complex loss model can be adopted, including the effect of secondary losses. The approach developed by Lieblein correlates profile losses directly to the suction-surface diffusion ratio, which serves as the primary aerodynamic indicator of blade loading and boundary layer wake development.

For off-design operations, where the incidence angle deviates from the optimum, the maximum suction-surface velocity ratio is approximated using Lieblein's empirical correlation [18]:

$$\frac{v_{\max}}{v_1} = 1.12 + a(\alpha_1 - \alpha_1^*)^{1.43} + \frac{0.61}{\sigma}\cos^2\!\alpha_1 \left(\tan\alpha_1 - \tan\alpha_2\right), \tag{6.1}$$

where $a = 0.0117$ for NACA 65-series blades, $\sigma = c/s$ is the solidity, α_1 and α_2 are the inlet and outlet flow angles relative to the axial direction, and $(\alpha_1 - \alpha_1^*)$ is the inlet flow angle deviation from the reference minimum loss.

To account for compressibility and streamtube contraction in modern transonic stages, this velocity ratio is corrected following the generalised form proposed by König [14] to yield the equivalent diffusion factor:

$$D_{\mathrm{eq}} = \frac{1}{\Omega}\frac{\rho_2}{\rho_1}\frac{\cos\alpha_2}{\cos\alpha_1}\frac{v_{\max}}{v_1}, \tag{6.2}$$

This definition highlights the effects of both compressibility, through the density ratio ρ_2/ρ_1, and stream-tube contraction, through the axial velocity-density ratio Ω [21].

Once D_{eq} is calculated, the wake momentum-thickness-to-chord ratio $(\theta/c)_2$ must be extracted from empirical reference plots. Using this value, the compressible total pressure profile loss coefficient, defined as $\tilde{\omega} = (p_{01} - p_{02})/(p_{01} - p_1)$, is computed via the modified relation from Manfredi and Fontaneto [21]:

$$\tilde{\omega}_p = 2\left(\frac{\theta}{c}\right)_2 \frac{\rho_1}{\rho_2}\frac{\sigma\Omega^2}{\cos\alpha_2}\left(\frac{\cos\alpha_1}{\cos\alpha_2}\right)^2\left(\frac{2H_2}{3H_2-1}\right)\left[1-\left(\frac{\theta}{c}\right)_2\frac{\sigma H_2}{\cos\alpha_2}\right]^{-3}\left(1+\frac{\gamma-1}{\gamma}\mathrm{M}_2^2\right)^{\frac{1}{\gamma-1}}, \tag{6.3}$$

where $H_2 = 1.08$ is the constant wake boundary-layer form factor, and the final term represents the isentropic total-to-static pressure ratio p_{02}/p_2.

6.1.2. Deviation Angle

The deviation angle at the reference minimum-loss incidence was established by Carter [8] as:

$$\delta^* = m\,\varphi\,\sigma^{-1/2} \tag{6.4}$$

where m is an empirical coefficient dependent on stagger angle and camber-line shape, φ is the blade camber angle, and σ is the solidity. At off-design incidence, Lieblein [18] proposed a correction accounting for the incidence $i = \beta_{\text{mec,in}} - \alpha_1$:

$$\delta = \delta^* + |i| \cdot \frac{\partial \Delta\beta^*}{\partial \alpha} \tag{6.5}$$

where $\partial\Delta\beta^*/\partial\alpha$ is the slope of the turning angle variation with angle of attack, provided by Lieblein [18] as a function of solidity and inlet flow angle.

The exit flow angle is then obtained as:

$$\alpha_2 = \beta_{\text{mec,out}} - \text{sgn}(\beta_{\text{mec,out}} - \alpha_1)\,\delta \tag{6.6}$$

where the sign convention ensures that deviation always acts as under turning regardless of the direction of blade curvature.

6.2. Validation Against CFD

The screen–IGV model is validated against a steady RANS CFD simulation of the compressor stage, operating with the distortion screen at its nominal position and the IGV row at uniform stagger ($\gamma = 0°$ re-stagger on all sectors). The axial distance between the screen and the IGV leading edge is $\Delta X_{adim} = 0.206$. The details of the simulations' setup have been discussed in Chapter 3

The two-dimensional CFD solution provides the flow field on a surface mesh in the annular domain. To enable a meaningful, quantitative comparison with the one-dimensional (1D) analytical model, which predicts a discrete number of circumferential sectors, a single value has to be extracted for each sector at each axial coordinate value. The total pressure field downstream of the IGV is not uniform in each sector, due to the wakes of the IGV blades, requiring an average on the azimuthal coordinate to compare the numerical results with the model. Due to the sectors' size changing downstream of the distortion screen and downstream of the IGV, an algorithm to identify each sector's extent at each axial coordinate was implemented to correctly average the quantities.

6.2.1. Circumferential sectors identification

Sectors edges are not imposed by any geometric feature in the CFD domain, they are generated by the non-uniform porous-jump boundary condition, which models the screen.

The chosen approach to locating them is to detect peaks in the azimuthal gradient of the total pressure profile $\bar{P}_t(\theta)$. However, the IGV blade wakes introduce sharp, localised variations of the flow field, which produce large gradient peaks unrelated to the sector structure, and must therefore be suppressed before any boundary detection is attempted.

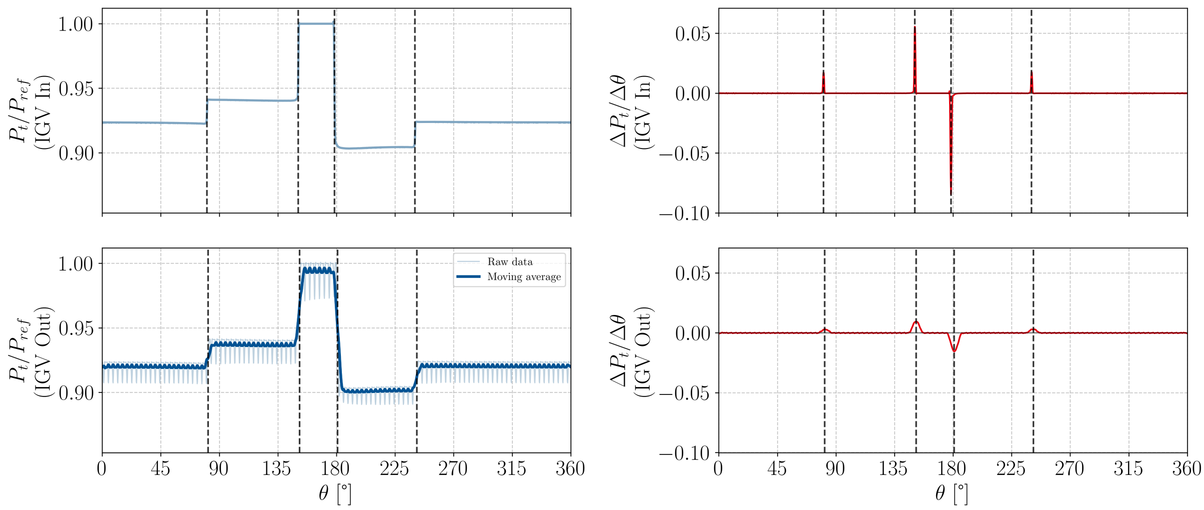

Figure 6.2: Circumferential total pressure profiles (P_t/P_{ref}) and their spatial derivatives at the IGV Inlet and Outlet. The automatically identified sector boundaries are marked by dashed lines.

At each axial station z_i, all CFD circumferential nodes are selected. The azimuthal gradient is then estimated by a centred finite difference scheme. At stations downstream of the IGV, a moving-average filter of width $\Delta\theta_{\text{win}} = 4°$ is first applied to $\bar{P}_t(\theta)$, and the same 4° is used as the finite-difference step; this suppresses the wakes effect that would otherwise cause peaks in the gradient. The value of $\Delta\theta = 4°$ has been choses to be higher than the angular distance between two blades and lower than the extent of the distortion sectors. At upstream stations, where the only non uniformity is given by the distortion screen, no smoothing is applied and a tighter finite-difference step of $\Delta\theta = 1°$ is used instead, preserving the resolution needed to detect the sharper sector edges. Sector boundaries are identified as the dominant peaks of the absolute gradient profile, retaining only those that exceed 15% of the global maximum and are separated by at least 15°, preventing double detections at a single edge. Figure 6.2 shows the total pressure at two axial locations, upstream and downstream of the IGV row, showing how the moving average reduces the wake effect on the total pressure distribution, and the identification of the sectors' boundaries.

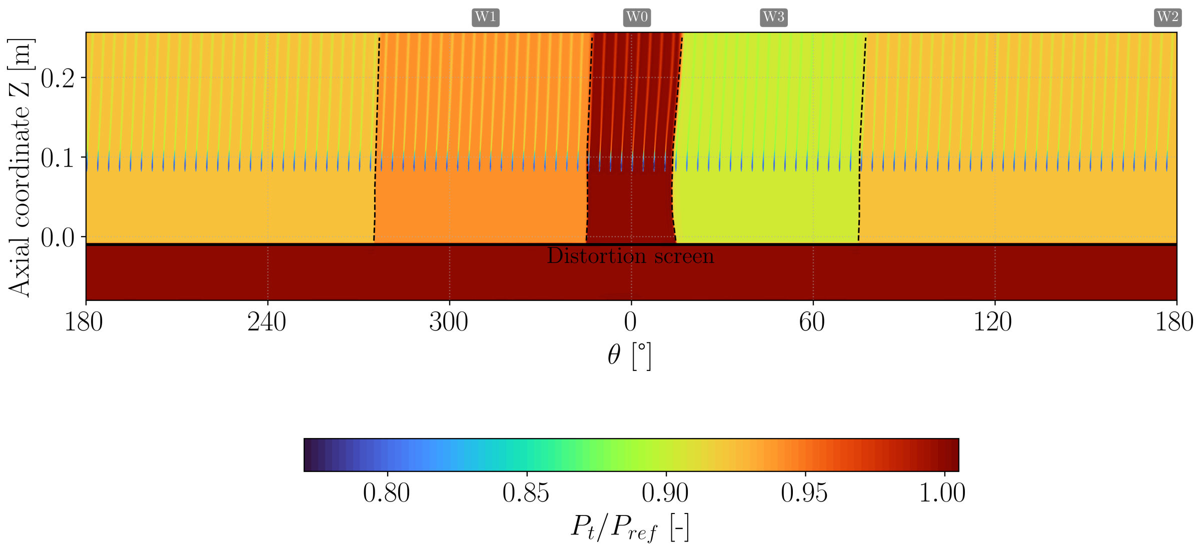

Figure 6.3: Contour of Total pressure on the axial–circumferential plane, dashed lines show the sectors' boundaries, identified using the described procedure.

6.2.2. Sector-Averaged Quantities

With the sector boundaries identified at every axial station, a representative scalar value is assigned to each sector W_k at each station z_i. Two averaging strategies are employed depending on the physical nature of the quantity.

Simple arithmetic mean. For the flow angle α, static pressure and static temperature T_s, the sector average is computed as

$$\phi_k = \frac{1}{N} \sum_{j=1}^{N} \phi(\theta_j,\, z_i)\,, \tag{6.7}$$

where $\{\theta_j\}$ is a set of $N = 100$ uniformly spaced angular points within the sector boundaries and $\phi(\theta_j, z_i)$ is the interpolated value at each point.

Mass-flux-weighted mean. For total pressure P_t and Mach number M, which are advected by the flow and must be weighted by the local mass flux, a flux-weighted average is computed:

$$\phi_k = \frac{\sum_{j=1}^{N} \phi(\theta_j,\, z_i)\; \rho(\theta_j,\, z_i)\; V_z(\theta_j,\, z_i)}{\sum_{j=1}^{N} \rho(\theta_j,\, z_i)\; V_z(\theta_j,\, z_i)}, \tag{6.8}$$

where ρ and V_z are the interpolated density and axial velocity, respectively.

6.2.3. Results and Discussion

The contour plots of Figures 6.3– 6.5 provide the two-dimensional flow field computed by the CFD. The total pressure field (Figure 6.3) clearly identifies the four distortion screen sectors, which impose different loss values across the annulus.

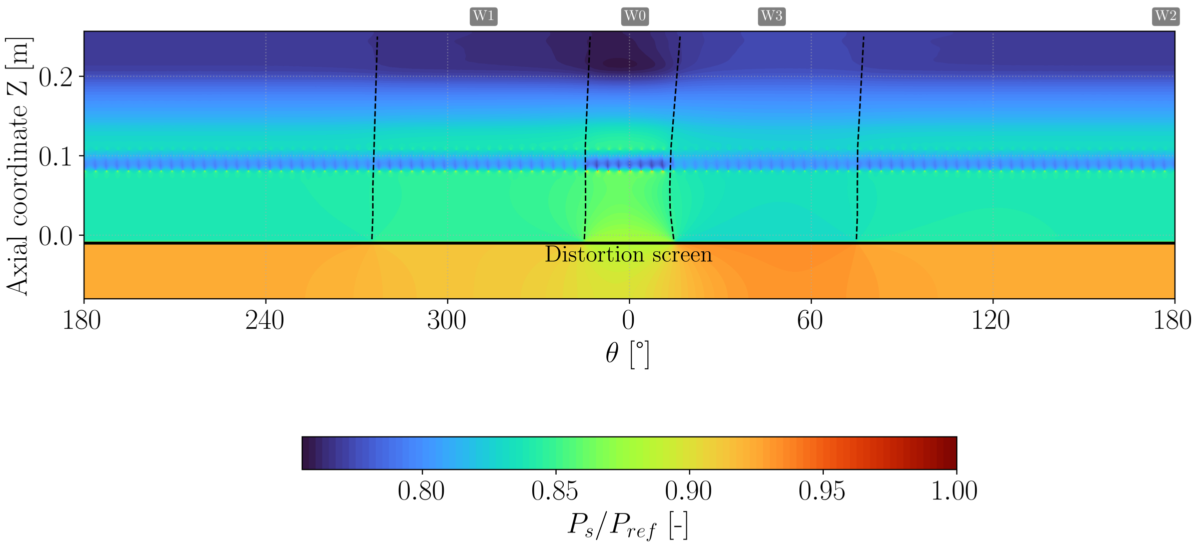

Figure 6.4: Contour of Static pressure on the axial–circumferential plane, dashed lines show the sectors' boundaries, identified using the described procedure.

The static pressure field (Figure 6.4) exhibits a circumferential non-uniformity upstream of the screen, where the flow anticipates the resistance variation imposed by the porous-jump boundary condition: sectors subjected to higher screen resistance (W2, W3) display a slightly elevated static pressure in the inlet region, consistent with the blockage effect. The IGV does not cause noticeable static pressure gradient, since in this configuration it is uniformly staggered. Immediately downstream of the screen, the static pressure drops sharply and then continues to decrease through the IGV passage as the flow accelerates. This acceleration is mostly due to the converging duct geometry, as discussed in Section 3.4.

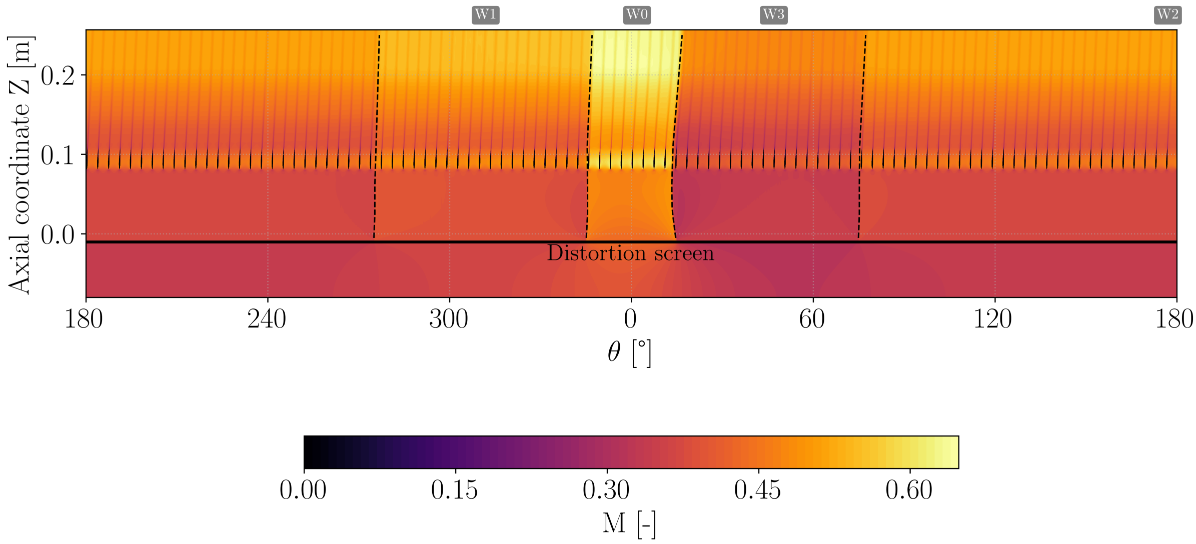

Figure 6.5: CFD contour of Mach number M on the axial–circumferential plane.

The Mach number contour (Figure 6.5) confirms this behaviour: the sectors with lower total pressure loss (W0, W1) achieve noticeably higher velocities at the IGV exit plane, while the high loss sectors (W2, W3) remain at lower Mach numbers throughout the passage. The IGV blade wakes are visible downstream of the trailing edge as thin, periodically spaced low-velocity streaks. These features constitute the flow physics that the 1D model must capture at a sector-averaged level.

Models comparison Figure 6.6 compares the Mach number predicted by three modelling strategies against the sector averaged CFD reference. The hybrid model is applied using the axial distance between the distortion screen and the IGV trailing edge, and it is expected to improve the model's match with the CFD, since the screen–CFD axial distance falls in a range where neither of the two models closely matched the CFD results, as discussed in Section 5.6. The result is a markedly improved agreement with the CFD across all four sectors, confirming that the hybrid strategy is the most appropriate modelling choice for this configuration. The RMSRE between model and CFD at the IGV outlet drops from 4.7% , 6.3% for the Decoupled and the Coupled model to 3.0% for the Hybrid model.

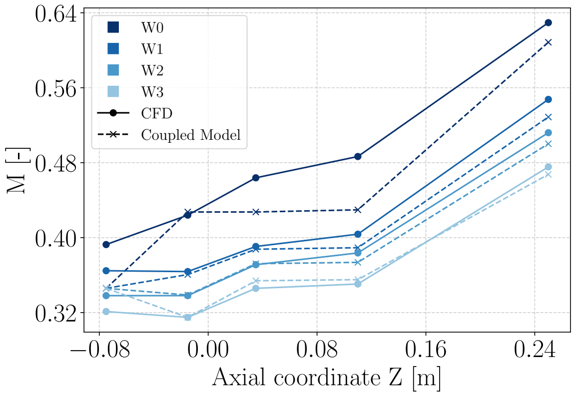

(a) Coupled

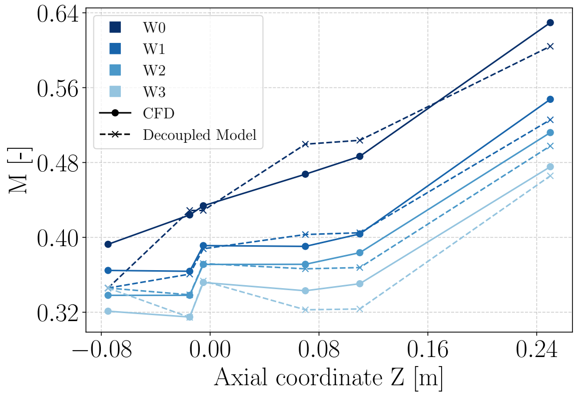

(b) Decoupled

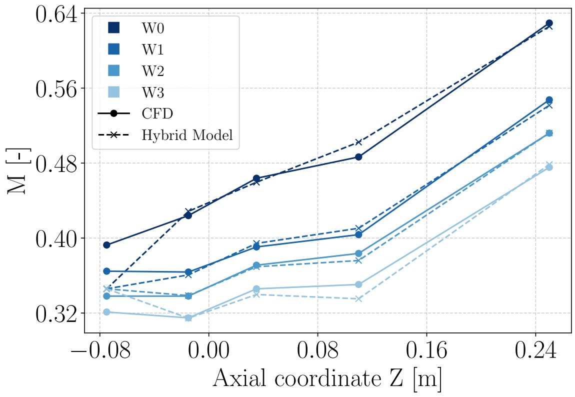

(c) Hybrid

Figure 6.6: Sector-averaged Mach number M as a function of the axial coordinate Z: comparison of the three modelling strategies against CFD for sectors W0–W3.

6.2.4. Model vs CFD comparison

In this section, only the results of the Hybrid model are shown and discussed.

Total Pressure. The total pressure ratio P_t/P_{ref} is the quantity best captured by the model, as shown in Figure 6.7a. Across all four sectors, both the upstream plateau and the abrupt drop occurring at the IGV plane are reproduced with very good accuracy. The level of total pressure in each sector downstream of the IGV, which is set by the loss model, agrees closely with the CFD, with an $RMSRE = 0.04\%$ calculated across all model points. This confirms that the Lieblein profile loss correlation provides a satisfactory estimate of the blade row losses under the present operating conditions.

Since the degree of mass flow redistribution is governed by the total pressure loss difference between sectors, a uniformly staggered IGV is not expected to cause high levels of mass

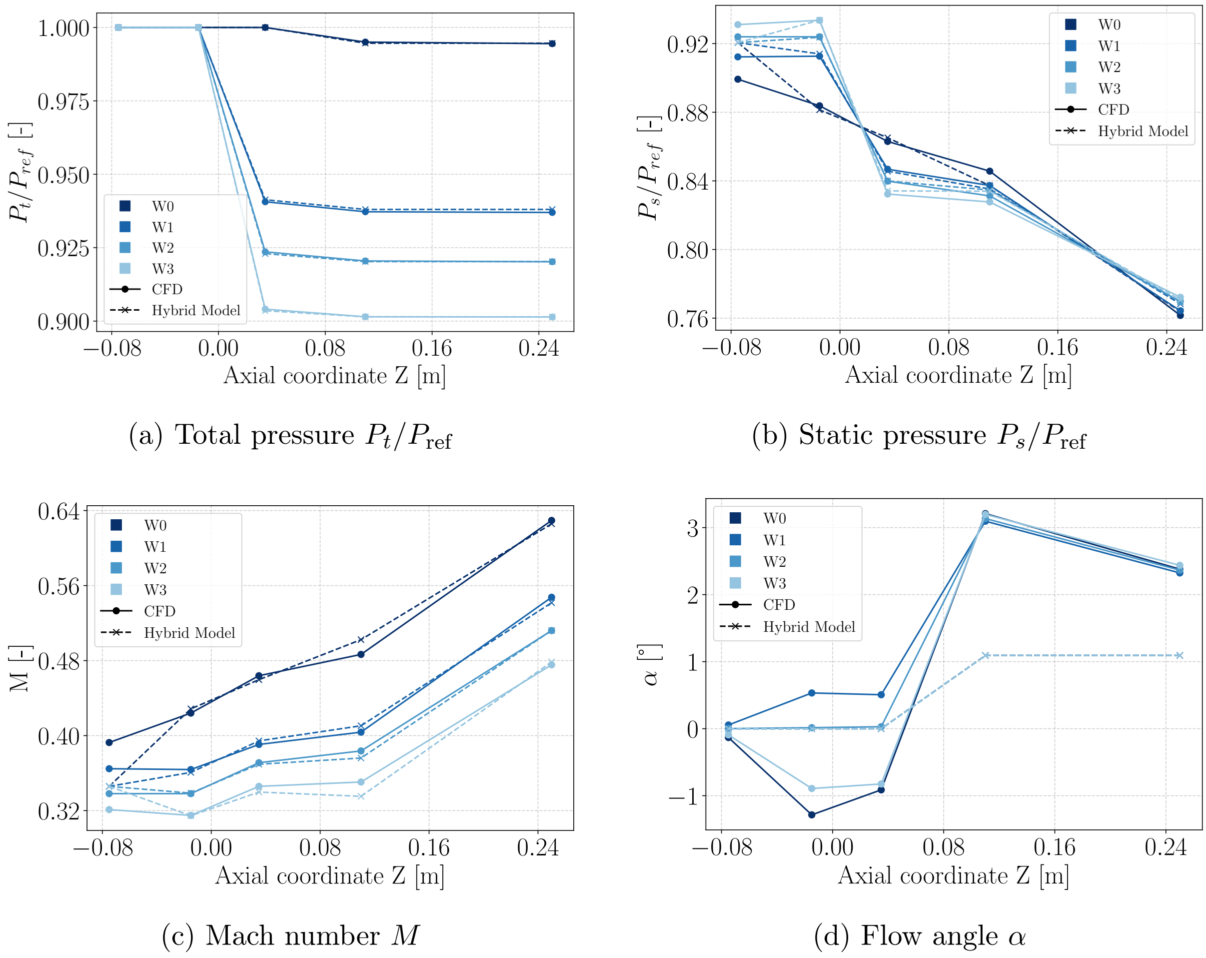

(a) Total pressure P_t/P_{ref}

(b) Static pressure P_s/P_{ref}

(c) Mach number M

(d) Flow angle α

Figure 6.7: Sector-averaged flow quantities as a function of the axial coordinate Z: hybrid model vs CFD , for sectors W0–W3.

flow redistribution. The only difference in losses between the sectors is caused by the different inlet flow conditions between them: higher inlet Mach values will cause higher losses: $\Delta p_t/p_{ref} = 0.54\%$ for W0 (clean sector), $\Delta p_t/p_{ref} = 0.21\%$ for W3 (most distorted sector).

Static Pressure and Mach Number. The static pressure (Figure 6.7b) and Mach number (Figure 6.7c) distributions are reproduced with reasonable, though not exact, agreement, with a RMSRE of 0.7% for static pressure and 3.0% for Mach number, both calculated across all model points. The model captures the correct trends: the inter-sector static pressure gradients that drive radial mass flow redistribution in the gap region, and the progressive acceleration of the flow through the IGV passage. However, some quantitative discrepancy remains, most notably far upstream (static pressure and Mach number RMSRE of 1.4% and 7%) and at the IGV exit plane (0.6% and 3%). These residual differences are attributed to the modelling limitations discussed below.

Flow angle. A difference of 2° is found in the flow angle distribution at the IGV outlet section, as shown in Figure 6.7d. This discrepancy is due to the deviation model used, which predicts a lower value than the one from the CFD. Since the distortion screen effect on the flow angle is not modelled, there is also a difference upstream and downstream of the screen of 1° in the most distorted and clean sectors.

The discussed approach, while being promising given the low error values, still needs further refinement from both the modelling and the computational point of view:

- **Flow angle mismatch**. The deviation angle predicted by the Carter–Lieblein correlation departs significantly from the CFD values across multiple sectors, indicating that the classical mean-line correlation does not capture the actual blade response under the highly non-uniform, distorted inflow imposed by the screen. This mismatch in exit flow angle has a direct consequence on the Mach number and static pressure predictions: the decomposition of the velocity vector into its axial and tangential components is sensitive to the swirl angle, so an error in deviation translates into a corresponding error in the axial velocity and, consequently, in the local Mach number and static pressure. Improving the accuracy of the deviation prediction, would be a prerequisite for further reducing the residual discrepancies in the Mach number and static pressure fields.
- **Non-Uniform CFD Upstream Static Pressure**. A secondary difference between the model and the CFD is visible in the static pressure profiles at stations far upstream of the screen (Figure 6.7b). Rather than being uniform across sectors, as the model assumes for the inlet boundary condition, the CFD shows a circumferential variation already at far-upstream axial station of up to 3%. This non uniformity is caused by the numerical domain and its discretization: the computational grid is either not sufficiently refined in the region far upstream of the screen or the domain is not sufficiently extended upstream of the distortion screen. This difference though, is not affecting the mass-flwo redistribution across the screen, since, as shown in Figure 6.7b, the static pressure distortion upstream of the screen predicted by the CFD is perfectly matched by the model.

To further validate the implemented model, a comparison with CFD should be provided in case of non-uniform staggered IGV. Even though the currently discussed IGV configuration causes a small degree of flow redistribution due to the different loss value across the annulus, only a non-uniform re-staggering would allow the coupled effects of the distortion screen and blade-row response to be assessed in a configuration with much higher flow redistribution.

6.3. Incidence optimization

The Screen–IGV model returns the complete flow field at the rotor inlet for every circumferential sector, and therefore allows the incidence on the compressor rotor to be calculated around the whole annulus. This makes it possible to quantify the aerodynamic effect of the inlet distortion by comparing, sector by sector, the distorted velocity triangles against the clean (undistorted) reference.

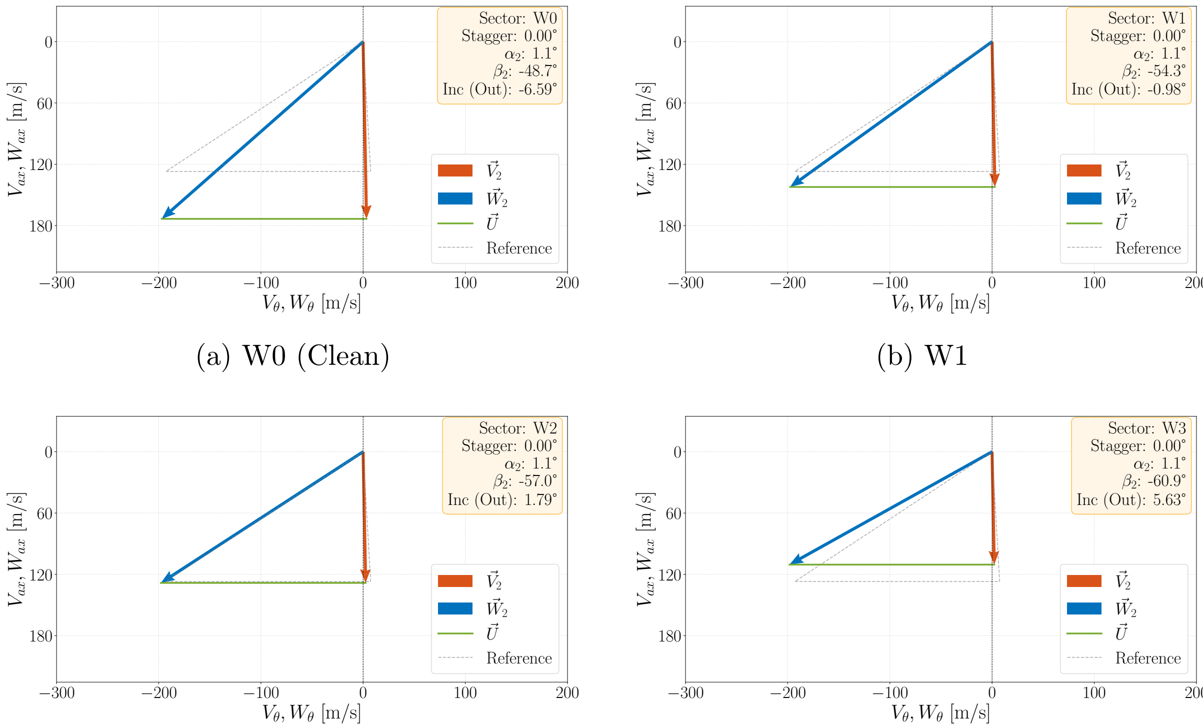

(a) W0 (Clean)

(b) W1

(c) W2

(d) W3

Figure 6.8: Rotor velocity triangles in the four circumferential sectors in the uniform IGV configuration. Dashed triangle: clean-operation velocity triangle.

Figure 6.8 reports the rotor velocity triangles in the four sectors for the baseline configuration, in which the IGV is uniform and set at its design stagger. The dashed triangle is the clean-operation reference velocity triangle. Because the IGV imposes essentially the same outlet flow angle in every sector, the differences between the triangles are driven by the local axial velocity. In the distorted sectors the screen blockage reduces the mass flow and hence the axial velocity: at a fixed flow angle this rotates the relative velocity vector and increases the magnitude of the relative flow angle β, so the rotor experiences a positive (opening) incidence. The clean sector behaves in the opposite way: the flow accelerates, β is reduced and the incidence becomes negative. The uniform IGV is thus unable to shield the rotor from the circumferential incidence variation introduced by the distortion.

As a first, preliminary mitigation step only the incidence is recovered. The IGV stagger is allowed to vary independently in each of the four sectors and is adjusted until the rotor incidence returns to its design value $\iota_{des} = 1.40°$ in every sector.

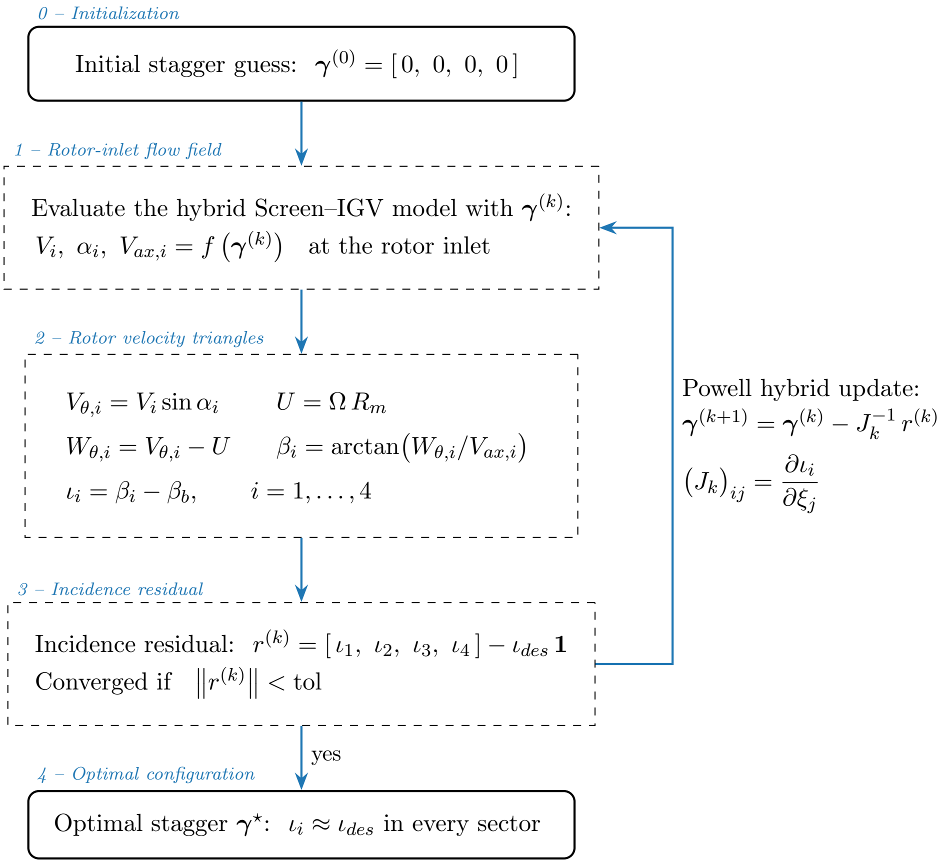

Figure 6.9: Iterative scheme for the sector-wise IGV stagger optimization.

The iterative procedure for the incidence optimization is shown in Figure 6.9. The four sector staggers are collected in the vector $\boldsymbol{\gamma} = [\gamma_1, \gamma_2, \gamma_3, \gamma_4]$, and the four incidence offsets from the design value in the residual vector $r(\boldsymbol{\gamma}) = [\iota_1 - \iota_{des}, \iota_2 - \iota_{des}, \iota_3 - \iota_{des}, \iota_4 - \iota_{des}]$. The optimal staggers are the solution of the nonlinear system $r(\boldsymbol{\gamma}) = \mathbf{0}$ ($\iota_i = \iota_{des}$ in every sector), which is solved in Python with the `hybr` root-finding algorithm of `scipy.optimize.root`: a modified Powell hybrid method that approximates the Jacobian $(J)_{ij} = \partial r_i / \partial \gamma_j$ by finite differences and updates the stagger vector with a Newton-like step. Each residual evaluation requires a full run of the hybrid Screen–IGV model with the current stagger vector, from which the rotor-inlet flow field, the velocity triangles, and thus the four incidences are reconstructed.

The optimized velocity triangles are reported in Figure 6.10. In all four sectors the rotor incidence is driven back to its design value ι_{des}, recovering the nominal relative flow angle at rotor inlet. The corresponding optimal stagger distribution, ordered from the clean sector (W0) to the most distorted one (W3), is

$$\gamma^{\star} = [\,-22.5,\ -9.8,\ 0.2,\ 16.8\,]^{\circ}.$$

The correction increases monotonically across the annulus and reverses sign: negative in the clean sector, positive in the most distorted one, and nearly zero in sector W2, whose incidence already sits close to the design value.

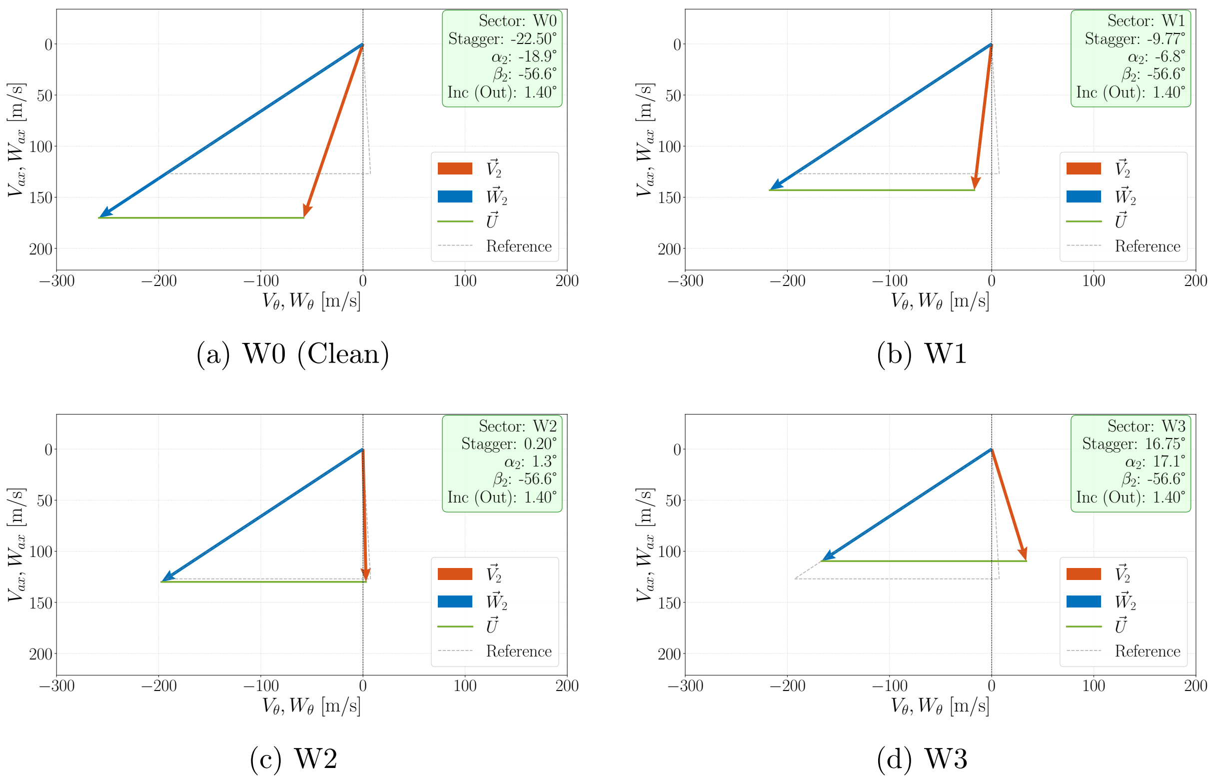

(a) W0 (Clean)

(b) W1

(c) W2

(d) W3

Figure 6.10: Rotor velocity triangles in the four circumferential sectors after the sector-wise stagger optimization.

A further limitation concerns the feasibility of the computed corrections: the required re-staggering is large, spanning from $-22.5°$ in the clean sector W0 to $+16.8°$ in the most distorted sector W3, and such wide deviations from the design stagger move the IGV blades away from their own design incidence and may drive the IGV row into stall, invalidating the assumption that the vane imposes a well-defined outlet flow angle in every sector. This aerodynamic limit on the IGV is not accounted for in the present model, in which the stagger is free to vary; it could be incorporated by prescribing the maximum admissible stagger deviation before blade stall as a bound on $\boldsymbol{\gamma}$ (equivalently, a limit on the IGV incidence), turning the unconstrained root-finding into a bounded problem in which, where such bound becomes active, the design incidence could no longer be fully recovered in that sector.

This is a *single-objective* optimization: the only target is the incidence angle. The procedure has one degree of freedom per sector (the local stagger) and one constraint per sector (zero incidence), so the incidence can be recovered perfectly, but the *magnitude* of the velocity is left uncontrolled. As a consequence, after optimization the incidence is uniform around the annulus while the Mach number is not: the distorted sectors, which still carry a lower mass flow, remain at a lower velocity and therefore a lower Mach number than the clean sector, as can be seen in Figure 6.10. Since the rotor losses are not only caused by incidence, but also by the inlet Mach number values, this does not guarantee a full recovery of the clean operation performance. A more complete recovery would require matching both the incidence and the Mach number in every sector simultaneously. This cannot be obtained by acting on the IGV stagger alone, and would require an additional design variable. An intermediate solution could be to optimize for a trade-off between the two quantities to reach the lowest possible losses on the rotor blades.

7 | Conclusions

This thesis developed a low-order, physics-based model for the coupled flow redistribution produced by a total pressure distortion screen and a downstream, non-uniformly re-staggered Inlet Guide Vane (IGV) row. The model serves a dual purpose: 1) as a design tool to predict the flow redistribution around distortion screens, enabling the generation of a prescribed total pressure profile at the rotor face, and; 2) As an optimization tool to identify the IGV re-staggered configuration that restores the rotor incidence to that of the clean machine

A one-dimensional stream-tube model of a single non-uniform screen was first formulated, with a total pressure-loss correlation decoupling porosity, wire-diameter Reynolds number and Mach number effects, calibrated on seven operating points. It reproduced the CFD static pressure and Mach number distortion with average deviations below 0.5% and agreed well with the experimental data measured downstream of the screen. The model was then extended to two resistive elements in series, where *Coupled* and *Decoupled* models represent the two limiting screens distances and a *Hybrid* model interpolates between them via an exponential weighting of the normalised axial distance, which reduces the error in the intermediate axial distance values, where each model alone presents some limitations.

Finally, the second screen was replaced by an IGV row, substituting the wire-mesh correlations with Carter–Lieblein cascade models for the profile loss and flow deviation. Validated against a full-annulus RANS simulation, the Screen–IGV model reproduced the total pressure loss, static pressure gradients and Mach number trends to good accuracy. The screen—IGV model was then used to propose an IGV re-staggering pattern, which recovers the rotor incidence to the design value.

The present work produced a number of physical insights into the flow redistribution mechanism. First of all, it has been shown that the circumferential redistribution driven by a non-uniform screen is established primarily upstream of the screen: the blockage of the distorted sectors raises the local static pressure and lowers the Mach number ahead of the distorted sector, while the clean one accelerates. As a direct consequence, a CFD simulation prescribing only the downstream total pressure of the distortion screen cannot recover the correct flow field; the portion of the domain upstream of the screen must be resolved explicitly. A second outcome concerns the antisymmetric static pressure closure adopted by the model, which constrains the mean of the static pressures immediately upstream and downstream of the screen to a common circumferential value. This physically based assumption proved to be a valid closure condition, enabling the model to correctly capture the redistribution on both sides of the distortion screen. Furthermore, another insight concerns the dependence of the coupling on the axial separation between two resistive elements. The back-pressure perturbation of the downstream screen on the upstream one relaxes in an exponential trend as the spacing increases, so that the transition from the fully coupled to the fully decoupled regime is itself exponential. This is why an exponential weighting of the *Coupled* and *Decoupled* solutions is required to model the back-pressure effect on the upstream screen. From a broader perspective, this thesis contributes to the understanding of flow redistribution in compressors operating under distorted inlet flows. Its findings are of direct relevance to compressor designers: an improved characterization of the effect of distortion screens in experimental test environments, and the development of a rapid tool for the preliminary optimization of the IGV stagger based on the underlying redistribution mechanisms, together constitute a key asset for future, more refined design strategies for distorted compressors.

7.1. Future work

The results of this thesis establish the analytical tools needed to design IGV re-staggering strategies for distortion mitigation. Several concrete steps are required to consolidate the model.

Model validation against a non-uniformly re-staggered IGV. The next step is the generation of a series of CFD simulations in which the IGV row operates with a non-uniform stagger angle distribution, rather than the uniform configuration used in the current validation. A non-uniform re-staggering introduces a more pronounced circumferential resistance variation, which produces larger mass-flow redistribution than the uniformly staggered case, and it is precisely this coupled redistribution that the Screen–IGV model is designed to predict. A reference re-staggering pattern can be used to define the stagger variation $\gamma(\theta)$ for this validation case.

Compressor stage implementation An additional refinement to the model concerns the interaction between the inlet distortion and the compressor's back-pressure effect. Due to the non-uniform total pressure distribution at the compressor inlet, the corrected mass flow varies across the circumferential direction of the annulus. As a result, different sectors of the compressor annulus operate at different positions along the characteristic map, giving rise to a spatially non-uniform back-pressure field that propagates upstream into the inlet duct. This circumferential variation in back-pressure introduces an additional perturbation that is not captured when the compressor is treated as imposing a uniform downstream boundary condition. Incorporating this effect into the model, by coupling the local operating point of each annular sector to its corresponding back-pressure influence on the upstream flow field, would improve the accuracy of the model in replicating the real operating conditions of the distortion screen and IGV.

Validation of optimized re-staggered IGV pattern The Screen–IGV model ultimately returns the predicted optimal re-stagger pattern for the IGV, which is the sector-wise stagger distribution required to restore the design incidence on the rotor around the entire annulus. For the distortion configuration investigated, this pattern is given by the stagger vector $\boldsymbol{\gamma}^{\star} = [\,-22.5,\ -9.8,\ 0.2,\ 16.8\,]^{\circ}$, ordered from the clean sector (W0) to the most distorted one (W3). The next step is to validate this re-stagger pattern, both numerically through high-fidelity CFD simulations and experimentally through dedicated tests in the VKI-R4 test rig.

Validation of optimized re-staggered IGV pattern The Screen–IGV model ultimately returns the predicted optimal re-stagger pattern for the IGV, which is the sector-wise stagger distribution required to restore the design incidence on the rotor around the entire annulus. For the distortion configuration investigated, this pattern is given by the stagger vector $\boldsymbol{\gamma}^{\star} = [\,-22.5,\ -9.8,\ 0.2,\ 16.8\,]^{\circ}$, ordered from the clean sector (W0) to the most distorted one (W3). It should be noted that the optimization enforces the design incidence on the rotor alone and places no constraint on the aerodynamic loading of the IGV row itself. The most extreme stagger values in the pattern may. This limitation is not captured by the present formulation, but it can be readily addressed by introducing the maximum incidence sustainable before stall as a bound in the optimization, thereby turning the current unconstrained problem into a constrained one. The next step is to validate this re-stagger pattern, both numerically through high-fidelity CFD simulations and experimentally through dedicated tests in the VKI-R4 test rig.

Bibliography

[1] A. Adler. Variation with mach number of static and total pressures through various screens. Technical report, 1946.

[2] W. Annand. The resistance to air flow of wire gauzes. *The Aeronautical Journal*, 57 (507):141–146, 1953.

[3] ANSYS, Inc. *ANSYS Fluent User's Guide*. ANSYS, Inc., 2025. Release 2025 R2.

[4] F. Azizi. On the pressure drop of fluids through woven screen meshes. *Chemical engineering science*, 207:464–478, 2019.

[5] B. Bailey, J. Montero, J. P. Parra, A. Robertson, E. Baeza, and R. Kamaruddin. Airflow resistance of greenhouse ventilators with and without insect screens. *Biosystems Engineering*, 86(2):217–229, 2003.

[6] E. Brundrett. Prediction of pressure drop for incompressible flow through screens. 1993.

[7] A. F. Campbell. An investigation of distortion indices for prediction of stalling behavior in aircraft gas turbine engines. Master's thesis, Virginia Polytechnic Institute and State University, Blacksburg, Virginia, august 1981.

[8] A. D. Carter. The low speed performance of related aerofoils in cascade. 1950.

[9] I. B. Celik, U. Ghia, P. J. Roache, and C. J. Freitas. Procedure for estimation and reporting of uncertainty due to discretization in cfd applications. *Journal of fluids Engineering-Transactions of the ASME*, 130(7), 2008.

[10] E. Commission, D.-G. for Research, Innovation, D.-G. for Mobility, and Transport. *Flightpath 2050 – Europe's vision for aviation – Maintaining global leadership and serving society's needs*. Publications Office, 2011. doi: doi/10.2777/50266.

[11] J. Gillespie, A. Hayden, T. Lowe, A. Untaroiu, and C. Nessler. Analysis of com-

plex total pressure distortion screens using one-dimensional loss data. *Journal of Turbomachinery*, 147(10):101009, 2025.

[12] J. Groth and A. V. Johansson. Turbulence reduction by screens. *Journal of Fluid Mechanics*, 197:139–155, 1988.

[13] E. Gunn and C. Hall. *Aerodynamics of boundary layer ingesting fans*, volume 45578. American Society of Mechanical Engineers, 2014.

[14] W. Konig, D. Hennecke, and L. Fottner. Improved blade profile loss and deviation angle models for advanced transonic compressor bladings: part i—a model for subsonic flow. 1996.

[15] P. K. Kundu, I. M. Cohen, and D. R. Dowling. *Fluid Mechanics*. Academic Press, 5th edition, 2012.

[16] T. Kurian and J. H. Fransson. Grid-generated turbulence revisited. *Fluid dynamics research*, 41(2):021403, 2009.

[17] A. Lesser and R. Niehuis. Transonic axial compressors with total pressure inlet flow field distortions. In *Turbo Expo: Power for Land, Sea, and Air*, volume 45578, page V01AT01A036. American Society of Mechanical Engineers, 2014.

[18] S. Lieblein. Loss and stall analysis of compressor cascades. *Journal of basic engineering*, 81(3):387–397, 1959.

[19] J. Longley and E. Greitzer. Inlet distortion effects in aircraft propulsion system integration. In *Steady and transient performance prediction of gas turbine engines*. Advisory Group for Aerospace Research and Development (AGARD), 1992.

[20] J. P. Longley and E. M. Greitzer. Inlet distortion effects in aircraft propulsion system integration. *Journal of Aircraft*, 29(3):538–545, 1992.

[21] M. Manfredi and F. Fontaneto. Transonic axial compressors loss correlations: Part i—analysis and update of loss models. In *Turbo Expo: Power for Land, Sea, and Air*, volume 84065, page V02AT32A029. American Society of Mechanical Engineers, 2020.

[22] F. R. Menter. Two-equation eddy-viscosity turbulence models for engineering applications. *AIAA journal*, 32(8):1598–1605, 1994.

[23] Mentour Pilot. The double bubble d8: A coming leap in efficiency? URL `https://mentourpilot.com/the-double-bubble-d8-a-coming-leap-in-efficiency/`.

[24] B. Mohankumar, C. A. Hall, and M. J. Wilson. Fan aerodynamics with a short intake at high angle of attack. *Journal of Turbomachinery*, 143(5):051003, 2021.

[25] A. Peters, Z. S. Spakovszky, W. K. Lord, and B. Rose. Ultrashort nacelles for low fan pressure ratio propulsors. *Journal of turbomachinery*, 137(2):021001, 2015.

[26] R. Pinker and M. Herbert. Pressure loss associated with compressible flow through square-mesh wire gauzes. *Journal of Mechanical Engineering Science*, 9(1):11–23, 1967.

[27] C. Reid. The response of axial flow compressors to intake flow distortion. In *Proceedings of the ASME 1969 Gas Turbine Conference and Products Show*. American Society of Mechanical Engineers, 1969. doi: 10.1115/69-GT-29.

[28] P. Roach. The generation of nearly isotropic turbulence by means of grids. *International journal of heat and fluid flow*, 8(2):82–92, 1987.

[29] P. J. Roache. Perspective: a method for uniform reporting of grid refinement studies. 1994.

[30] R. Toracchio. Performance and stability analysis of a highly-loaded low-pressure compressor under distorted inflow conditions. 2024.

[31] R. S. Wakeland and R. M. Keolian. Measurements of resistance of individual square-mesh screens to oscillating flow at low and intermediate reynolds numbers. *J. Fluids Eng.*, 125(5):851–862, 2003.

[32] K. Wieghardt. On the resistance of screens. *Aeronautical Quarterly*, 4(2):186–192, 1953.

A | Loss correlation validation plots and RMSE tables

This appendix collects the complete set of validation results for the single-screen analytical model against the experimental measurements at the VKI R4 facility.

Figure A.1– A.3 show the circumferential distributions of P_t/P_{t0M} predicted by the model, compared to the experimental values. For each sub-model function, all the available functions are compared, while the other two sub-models are fixed to the best performing combination. The results are shows for all the seven available operating conditions, ranging the whole compressor map.

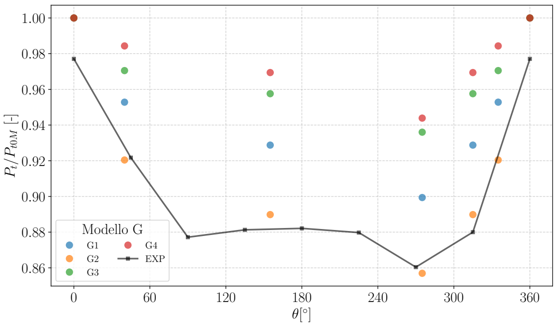

(a) $\dot{m} = 10.038$ kg/s

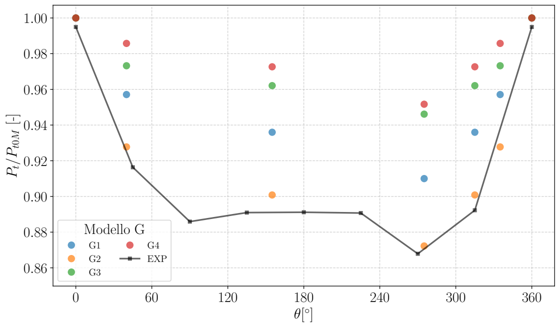

(b) $\dot{m} = 9.712$ kg/s

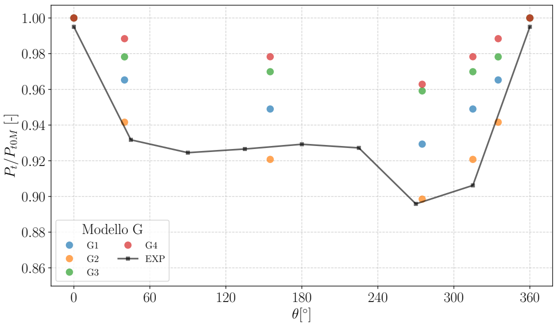

(c) $\dot{m} = 8.949$ kg/s

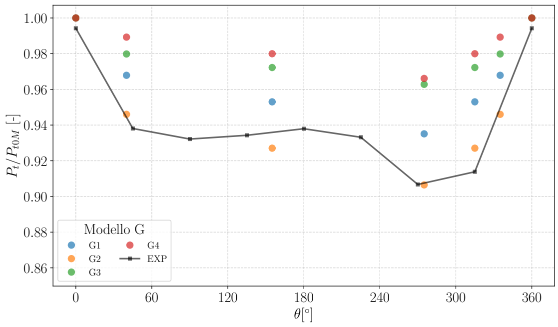

(d) $\dot{m} = 8.667$ kg/s

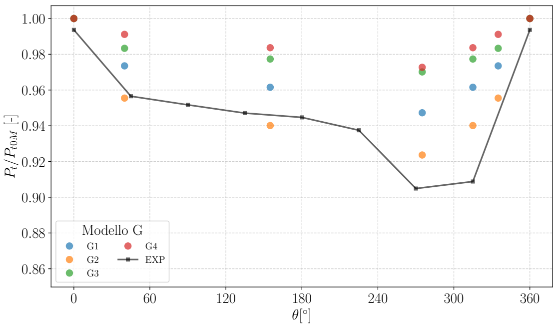

(e) $\dot{m} = 7.980$ kg/s

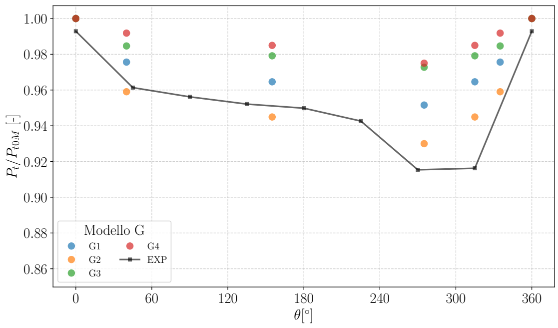

(f) $\dot{m} = 7.693$ kg/s

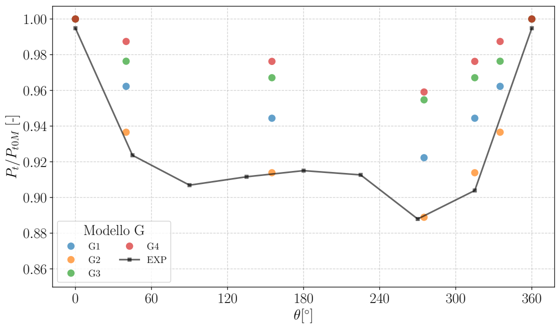

(g) $\dot{m} = 9.254$ kg/s

Figure A.1: Sensitivity to the porosity function $G(\beta)$ across all seven operating conditions. In each plot, the porosity function is held fixed at G_2 and the Mach correction is enabled.

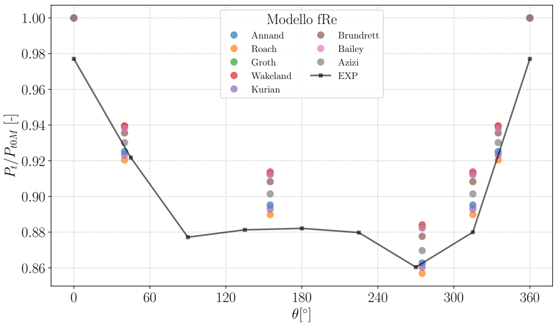

(a) $\dot{m}$ = 10.038 kg/s

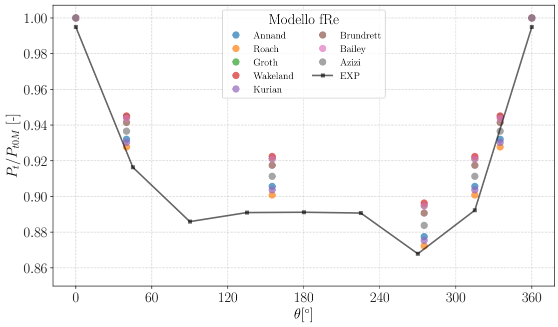

(b) $\dot{m}$ = 9.712 kg/s

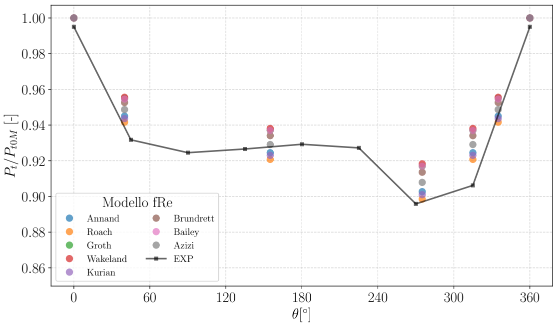

(c) $\dot{m}$ = 8.949 kg/s

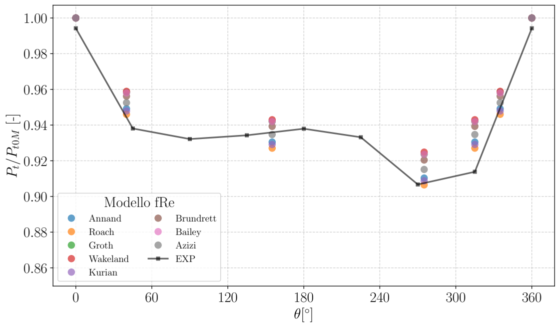

(d) $\dot{m}$ = 8.667 kg/s

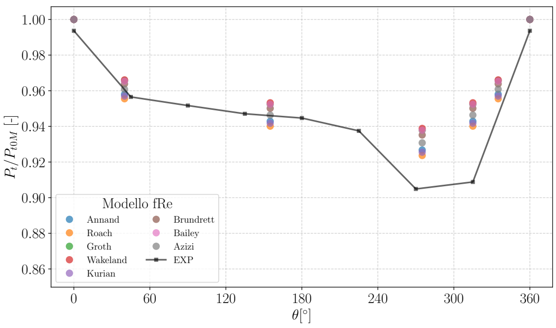

(e) $\dot{m}$ = 7.980 kg/s

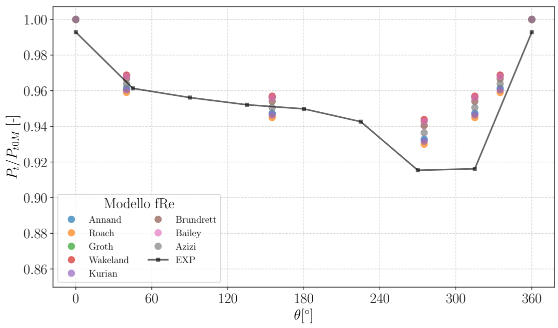

(f) $\dot{m}$ = 7.693 kg/s

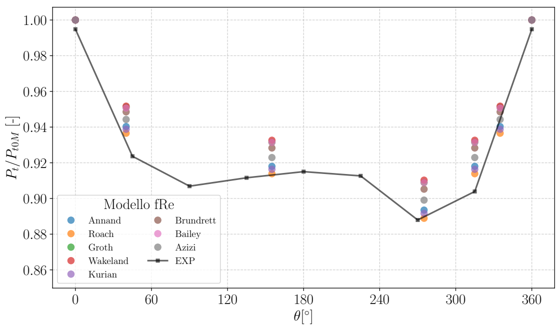

(g) $\dot{m}$ = 9.254 kg/s

Figure A.2: Sensitivity to the Reynolds number function $F(Re_d)$ across all seven operating conditions. The porosity function is held fixed at G_2 and the Mach correction is enabled.

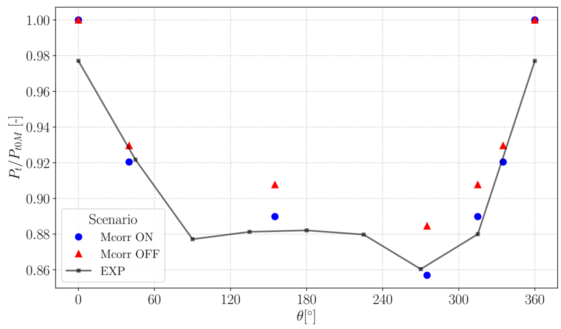

(a) $\dot{m} = 10.038$ kg/s

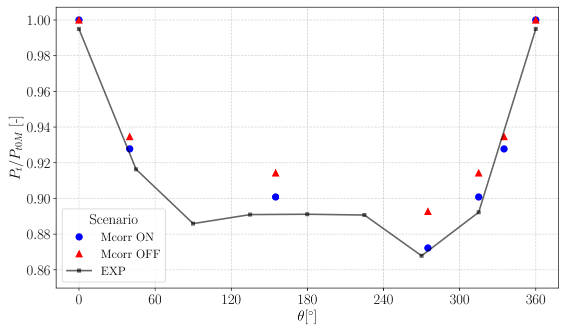

(b) $\dot{m} = 9.712$ kg/s

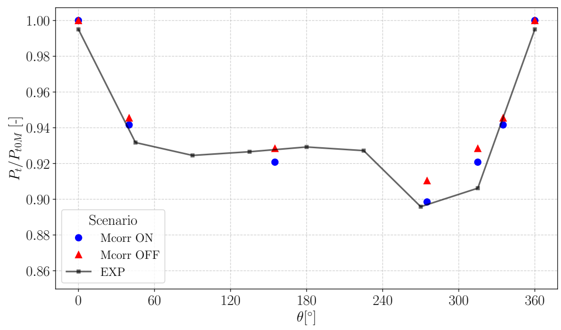

(c) $\dot{m} = 8.949$ kg/s

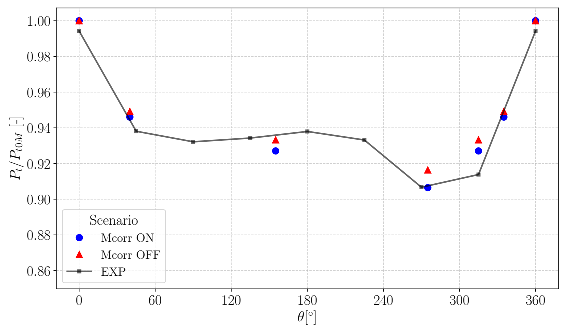

(d) $\dot{m} = 8.667$ kg/s

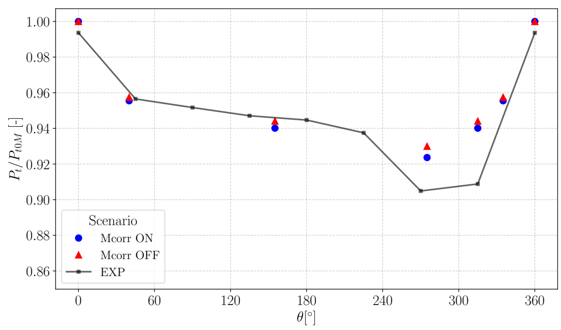

(e) $\dot{m} = 7.980$ kg/s

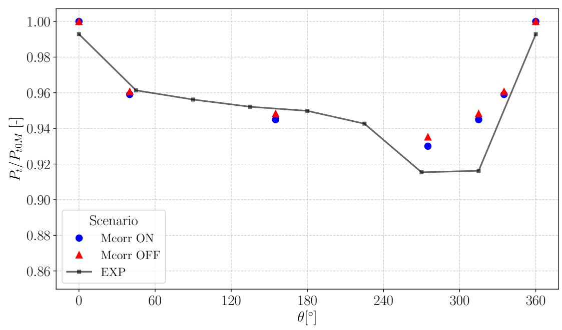

(f) $\dot{m} = 7.693$ kg/s

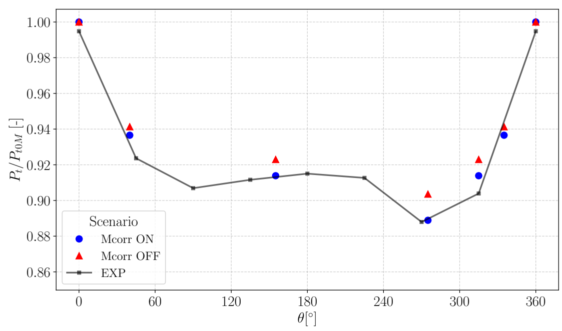

(g) $\dot{m} = 9.254$ kg/s

Figure A.3: Effect of the Mach number compressibility correction across all seven operating conditions. `Mcorr ON` is compared against `Mcorr OFF`. Porosity function is fixed at G_2 and the *Roach* Reynolds function is fixed.

A.1. RMSE tables

Tables A.1 and A.2 report the global RMSE (%) aggregated over all seven operating conditions for every combination of porosity function G_i and Reynolds number function $F(Re_d)$, with the Mach number correction enabled and disabled, respectively. Each cell value is the RMSE expressed as a percentage of the reference total pressure P_{t0M}. The minimum value in each table is highlighted in bold.

Table A.1: Global RMSE (%) over all seven operating conditions – `Mcorr ON`.

	Annand	**Roach**	**Groth**	**Wakeland**	**Kurian**	**Brundrett**	**Bailey**	**Azizi**
G_1	3.30	3.08	4.03	4.09	3.22	3.86	4.02	3.57
G_2	1.23	**1.09**	2.09	2.16	1.16	1.85	2.07	1.49
G_3	5.13	4.98	5.58	5.61	5.07	5.47	5.57	5.29
G_4	5.82	5.72	6.15	6.17	5.78	6.07	6.14	5.94

Table A.2: Global RMSE (%) over all seven operating conditions – `Mcorr OFF`.

	Annand	**Roach**	**Groth**	**Wakeland**	**Kurian**	**Brundrett**	**Bailey**	**Azizi**
G_1	3.87	3.67	4.54	4.59	3.79	4.38	4.53	4.11
G_2	1.83	**1.58**	2.75	2.83	1.73	2.52	2.74	2.15
G_3	5.54	5.41	5.94	5.97	5.49	5.84	5.93	5.68
G_4	6.12	6.03	6.42	6.44	6.09	6.35	6.42	6.23

The two tables confirm the conclusions drawn in Section 4.5.1. Across both correction settings, the porosity function G_2 consistently yields the lowest RMSE for every Reynolds number function, with the minimum achieved by the combination G_2 + Roach + Mach correction (RMSE = 1.09%). Enabling the Mach number correction reduces the RMSE for all combinations without exception. The porosity functions G_3 and G_4 perform significantly worse than G_1 and G_2 across all conditions, suggesting that the choice of porosity formulation is the dominant source of modelling uncertainty in the loss correlation.

Acknowledgment

L'esperienza al von Karman Institute for Fluid Dynamics (VKI) è stata estremamente formativa e un'occasione di crescita sia personale che professionale. Vorrei perciò ringraziare le persone che hanno reso possibile questo progetto e che mi hanno seguito durante il suo svolgimento. Vorrei ringraziare il Professor Paolo Gaetani, per avermi dato questa possibilità e per aver dimostrato interesse e fiducia verso i suoi studenti, mettendo il suo tempo a disposizione. Vorrei poi ringraziare il Professor Fabrizio Fontaneto, per aver seguito e gestito il progetto al VKI e per essere stato un punto di riferimento, dandomi consigli nei momenti più delicati e mantenendo un approccio critico sul lavoro svolto, che mi ha permesso di evidenziarne sia i punti di forza che i limiti. Ringrazio infine il Dr. Riccardo Toracchio, per il suo costante supporto, la sua estrema disponibilità e i suoi consigli durante lo svolgimento del progetto e la stesura della tesi, dai quali ho avuto modo di imparare moltissimo. Lo ringrazio per avermi dedicato tanto del suo tempo, a riprova di quanto ci tenga al lavoro dei suoi studenti.